N71-36191

REPORT NO. GDC-DDE71-001
CONTRACT NAS9-11191
FINAL REPORT

CASE FILE
COPY

A PRELIMINARY INVESTIGATION OF POTENTIAL VALUE-LOADS ALLEVIATION CONTROL FOR SPACE SHUTTLE VEHICLES

GENERAL DYNAMICS
Convair Aerospace Division

CR-115165

REPORT NO. GDC-DDE71-001

A PRELIMINARY INVESTIGATION OF POTENTIAL VALUE-LOADS ALLEVIATION CONTROL FOR SPACE SHUTTLE VEHICLES

30 June 1971

Prepared Under
Contract NAS9-11191

Prepared for
National Aeronautics and Space Administration
MANNED SPACECRAFT CENTER
Houston, Texas

Prepared by
CONVAIR AEROSPACE DIVISION OF GENERAL DYNAMICS
San Diego, California

FOREWORD

This investigation was conducted for the NASA Manned Spacecraft Center Guidance and Control Division. Mr. Frank Elam was the technical monitor. The study was performed by Mr. B. J. Kuchta and Mr. D. M. Sealey of Convair Aerospace Division of General Dynamics, San Diego, California.

TABLE OF CONTENTS

TABLE OF CONTENTS (Contd)

LIST OF FIGURES

LIST OF FIGURES (Contd)

LIST OF FIGURES (Contd)

LIST OF FIGURES (Contd)

LIST OF TABLES

UNITED STATES OF AMERICA
UNITED STATES OF AMERICA

SUMMARY

An investigation was made to estimate the potential value of load alleviation control for the space shuttle vehicle. The study examined the application of rigid body load relief and modal suppression control systems. Efforts were also expended on a preliminary fatigue damage analysis. The study was conducted for a two-element, straight, fixed-wing configuration.

Both the Marshall synthetic and Atlantic Missile Range (AMR) real winds were used in the analysis. To determine the performance penalties associated with a given load reduction technique, closed loop guidance was incorporated into load trajectory analysis. Orbiter and booster element wing and horizontal tail design conditions were ascent head/tail winds and entry maximum pullout normal acceleration. Minimum material gage influences the design for major portions of the orbiter horizontal tail and wing. Load relief is necessary for the ascent side wind condition to maintain control of the vehicle and to reduce vertical tail design loads.

In general, load reduction can save approximately 3 percent of the orbiter and booster wing and horizontal tail structural weight. Load reduction can reduce the vertical tail load by 25 percent which results in a structural weight saving of 12 percent. Orbiter and booster fuselage structural weight savings can amount to 500 pounds and 2000 pounds, respectively. Overall approximately 1500 to 2000 pounds of payload can be added to the vehicle by using load reduction technique. The techniques can be: (1) trajectory biasing, (2) gimbal angle limiting, (3) normal accelerometer feedback, or (4) gain scheduling. Trajectory biasing has been used on such missile systems as the Atlas. Gain scheduling offers a very promising method and is the method recommended for reducing the lateral loads.

Preliminary estimates were made for the accumulative fatigue damage of both vehicles. Vehicle life load spectra were developed for the booster and orbiter major structural elements. The selected fatigue control points were the wing root, vertical tail root, horizontal tail root, and a frame on the fuselage forward of the wing intersection. The load spectra include loads due to: (1) ascent winds and gusts, (2) entry flight path maneuvering, (3) cruise/approach/landing gust and maneuvering, and (4) taxi loads. The gust loads spectra were computed by using power spectral density techniques. Ascent wind load spectra were developed by simulating the ascent flight and "flying" the vehicle through numerous flights. Entry flight loads spectra were also developed from simulated flights. No fatigue damage was found at any of the eight monitored control points. However, the fatigue damage was estimated using Miner's theory and

the material properties data was not sufficient to yield high confidence levels. Very little data was found in the high-stress, low-cycle region in which a large portion of the space shuttle structure operates.

The third phase of this study evaluated methods of suppressing low-frequency structural vibration modes. Considerations were given to suppressing wing modes and fuselage modes. The approach taken was to use closed-loop modal damping as a measure or yardstick for modal suppression.

The study has shown that a small increase in closed-loop damping of the first few structural modes can be obtained by multiple sensors but that a significant increase can be realized by introducing two controllers. During ascent, a rigid/elastic body analysis indicates that rate gyros are needed in both the nose and tail of the booster element to provide basic flight stability. Single sensors produced instability through the thrust vector control system. Added modal damping can be provided through the operation of a canard located near the nose of the booster element.

For the suppression of wing modes at least two controllers are necessary. For a single control surface a stabilizing generalized force is produced for some modes and a destabilizing generalized force for other modes. For the wings of both the orbiter and booster, aileron-type surfaces should be located near the wing tip and at the wing mid-span. One rate gyro located near each of these control surfaces can provide control signals for good modal suppression. These wing-located sensors are not required for basic stability of the vehicle.

With modal suppression, the fatigue damage rate can be reduced by 10 percent. This small potential reduction in fatigue damage is due to the fact that a majority of the fatigue damage is attributable to rigid body load variations. The load spectra in a large part is made up of ascent wing loads, entry flight path variation loads, normal rigid body gust loads, and aircraft type operational maneuver loads.

The results of this study apply to the configuration studied (straight-wing booster/straight-wing orbiter; 3.5 million pounds gross liftoff weight). Indications are that the recommendations of the application of load alleviation are highly configuration dependent and, therefore, each specific configuration must be studied in depth.

SECTION 1

INTRODUCTION

The objective of this study was to conduct a preliminary investigation of the potential value of load alleviation control for a typical space shuttle vehicle. The yardstick used to evaluate the various load alleviations control systems considered was payload in orbit. The parameters of each system investigated were varied in a manner whereby the payload in orbit was increased above a given baseline. The baseline used in this study was the non-load alleviated Convair/North American Phase B baseline configuration of August 1970.

Key parameters that were considered included:

a. Complexity of Control. The factors influencing complexity include the type of sensors required and actuator requirements.

b. Design Risk. The factors influencing vehicle and control design risk include load minimization, sensor and control simplicity, as well as the use of existing sensors.

c. Reliability/Redundancy. Simplicity of sensors and minimum modification to the basic autopilot which has no load relief.

d. Trajectory Dispersions. Minimize trajectory dispersions in order to achieve a payload optimal ascent.

The study included the review of existing and current boost analyses for loads effects, compensation methods, and resulting trajectory errors. The analyses consisted of time varying three-degree-of-freedom pitch plane simulation, time varying six-degree-of-freedom rigid body simulations, random gust analysis, and multi-loop linear analysis. Each of these analysis technique are described in the appendixes. The simulation effort dealt with the evaluation of the selected rigid body load reduction systems. The control schemes investigated were not optimized in the sense that gains and filters were not optimum. However, those gains and filters used represent the best engineering estimate.

The study was divided into three parts. Part one investigated the potential structural weight saving that can be obtained by active, rigid-body load reduction. Part two estimated the fatigue damage on major structural components. Part three investigated candidate model suppression control schemes for the wings and bodies.

This report is organized in the manner described above.

1.1 CONFIGURATION

The study considered the space shuttle vehicle configuration as established in August 1970. At that time the major emphasis of the Phase B space shuttle study was toward the low-crossrange mission. Therefore, the Convair Aerospace/North American Phase B baseline was selected as the study configuration. The configuration shown in Figure 1-1 consists of a straight wing booster and the low-crossrange, straight wing orbiter. Both vehicles have conventional tails and use thrust vector control on ascent, attitude control propulsion system (ACPS) control in low dynamic pressure, and elevator/stabilizer/aileron/rudder control for conventional flight. The transition from high angle of attack entry flight to low angle of attack cruise/approach/landing portions of flight occurs dynamically at a subsonic Mach number. This type of transition applies to both the orbiter and booster vehicles.

The aerodynamic data used throughout the study was derived from wind tunnel tests. The data included orbiter/booster interference interaction effects.

To assess the structural weight savings or penalties associated with load alleviation, a detailed structural model of both the orbiter and booster were established. Figures 1-2 and 1-3 present the structural layout of the orbiter and booster, respectively. This structural definition was used to determine the elastic modes of vibration of the individual vehicles and the combined launch configurations.

1.2 SPACE SHUTTLE MISSION

The space shuttle vehicle will be subjected to severe environmental conditions. Figure 1-4 shows the basic phases of the space shuttle mission. To arrive at fatigue damage estimates, this study considered loads produced by: servicing, towing, pad erection, launch, boost ascent, separation, booster and orbiter entry, orbiter and booster transition, booster cruise, and orbiter and booster approach/landing and taxi. A service life of 100 missions was used. The ascent portion of flight was divided into nine flight segments while the entry was divided into three flight segments. The cruise/approach portion of flight represented one flight segment. At each flight segment, load spectra were determined and fatigue damage was estimated for orbiter and booster, wing root, horizontal tail root, vertical tail root, and a fuselage point near the wing leading edge.

1.3 FLIGHT PROFILE

To estimate the potential of load relief, nominal trajectories for wind and no-wind flight conditions were obtained for all flight phases. The no-wind ascent trajectories were used to measure the performance gains or losses associated with the wind conditions and load alleviation. A comparison of the wind conditions with and without load alleviations was made to estimate the potential load reduction.

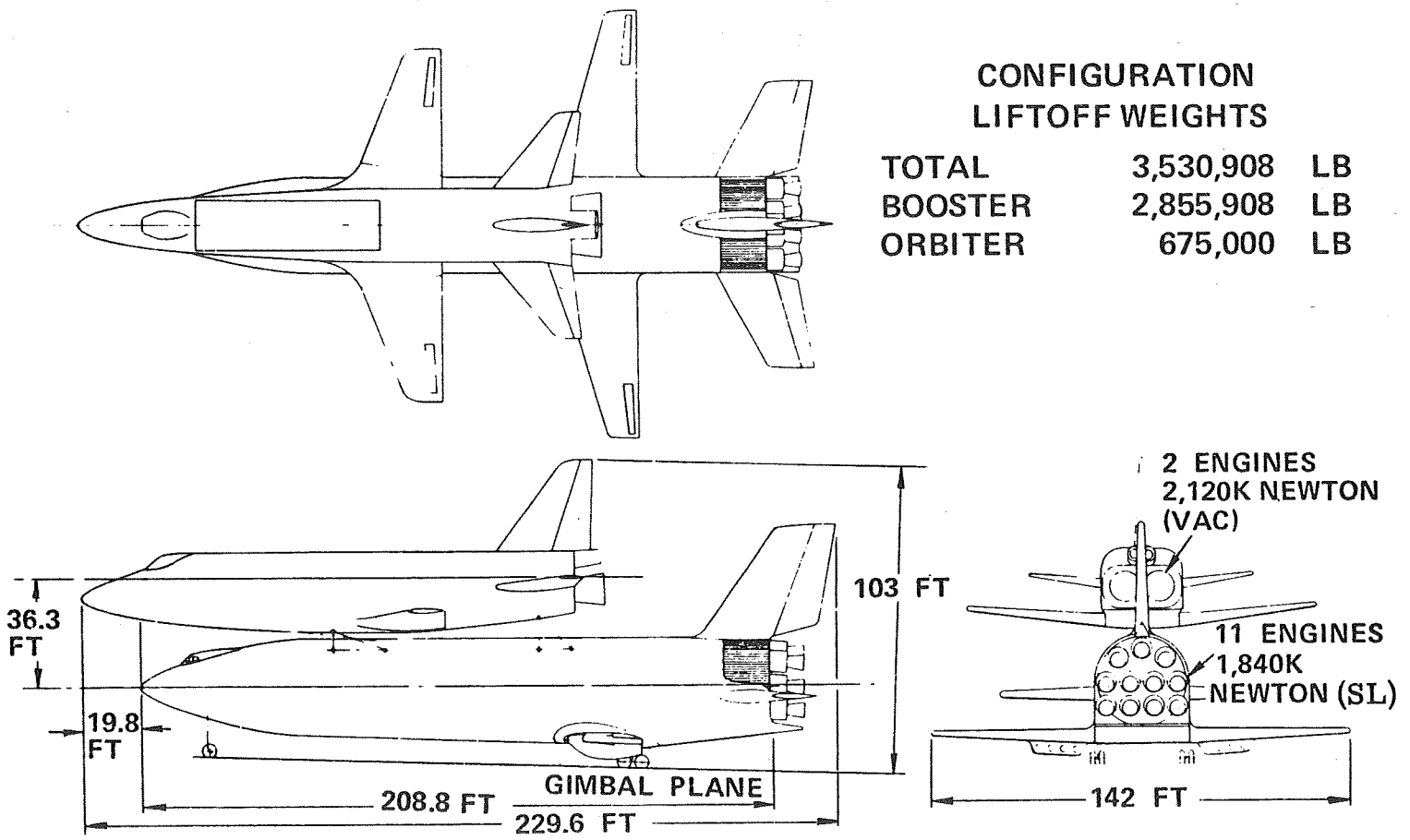

Figure 1-1. Mated Vehicle System — Straight Wing Orbiter and Booster

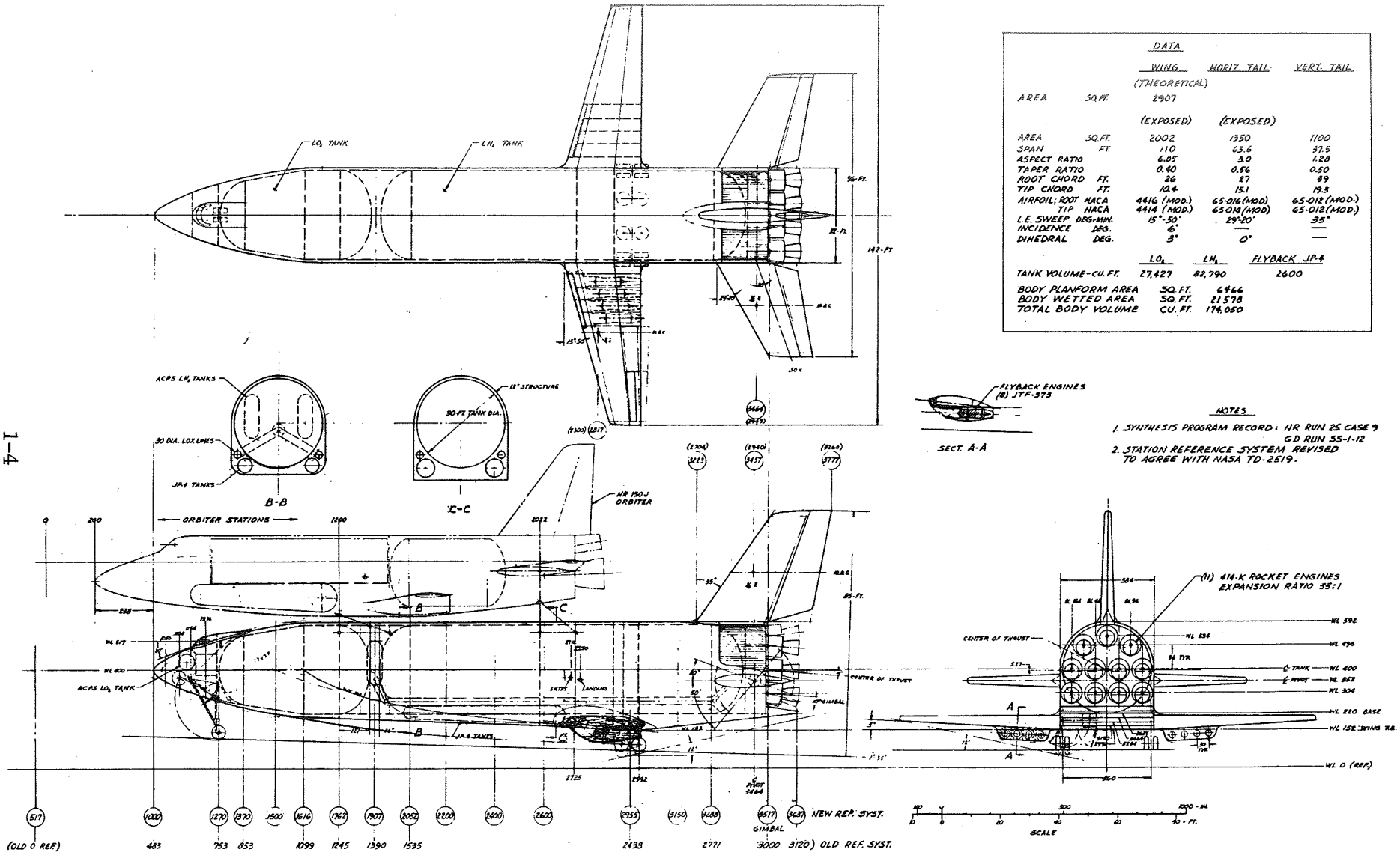

Figure 1-2. Booster General Arrangement

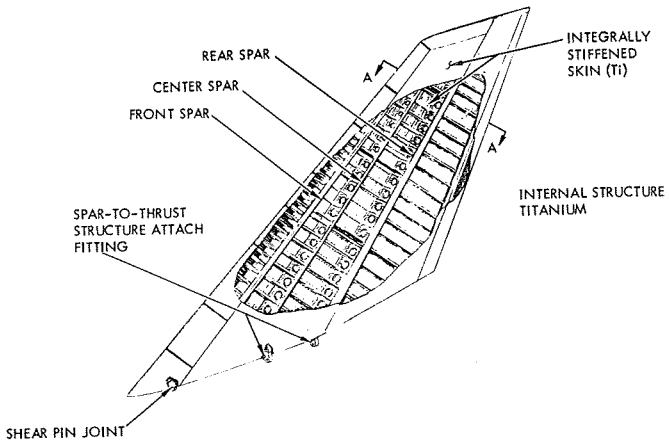

VERTICAL STABILIZER

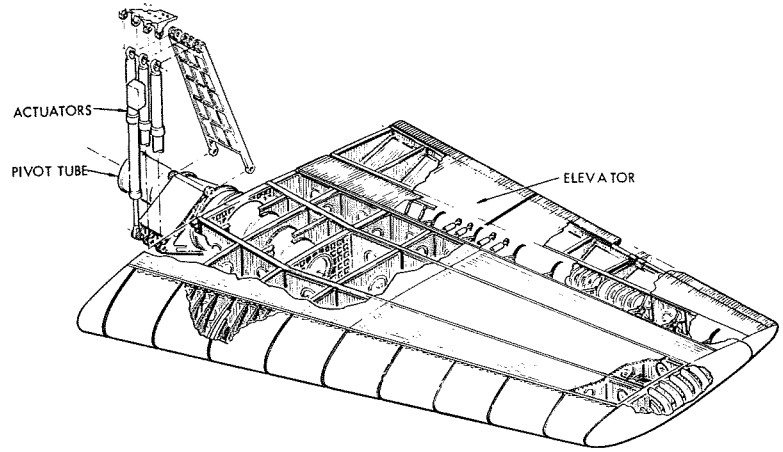

HORIZONTAL STABILIZER

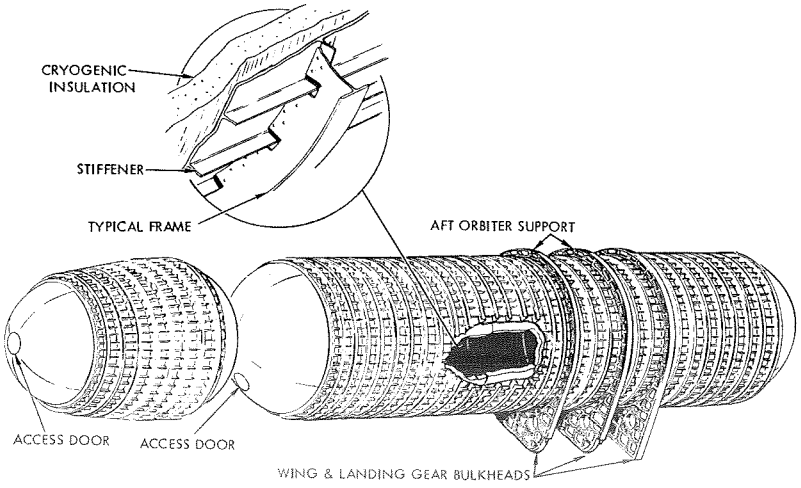

PROPELLANT TANKS

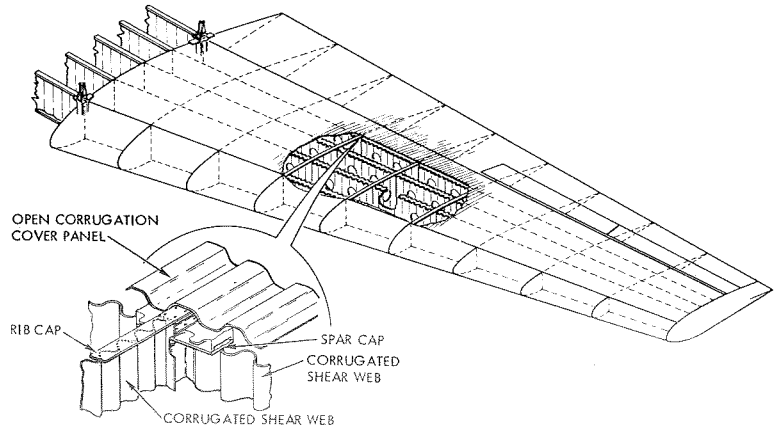

WING

Figure 1-2. Booster General Arrangement (Contd)

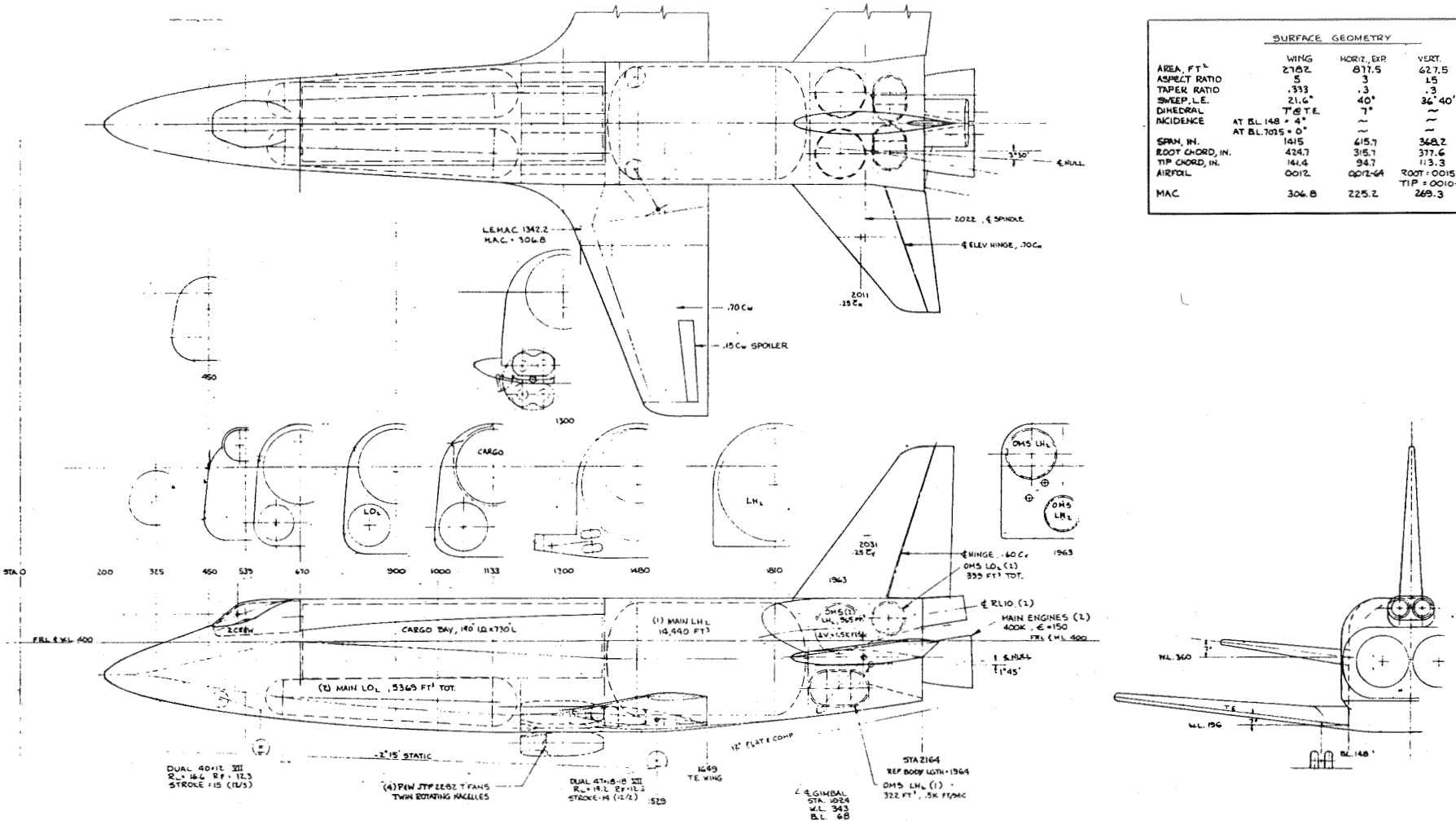

Figure 1-3. Orbiter General Arrangement

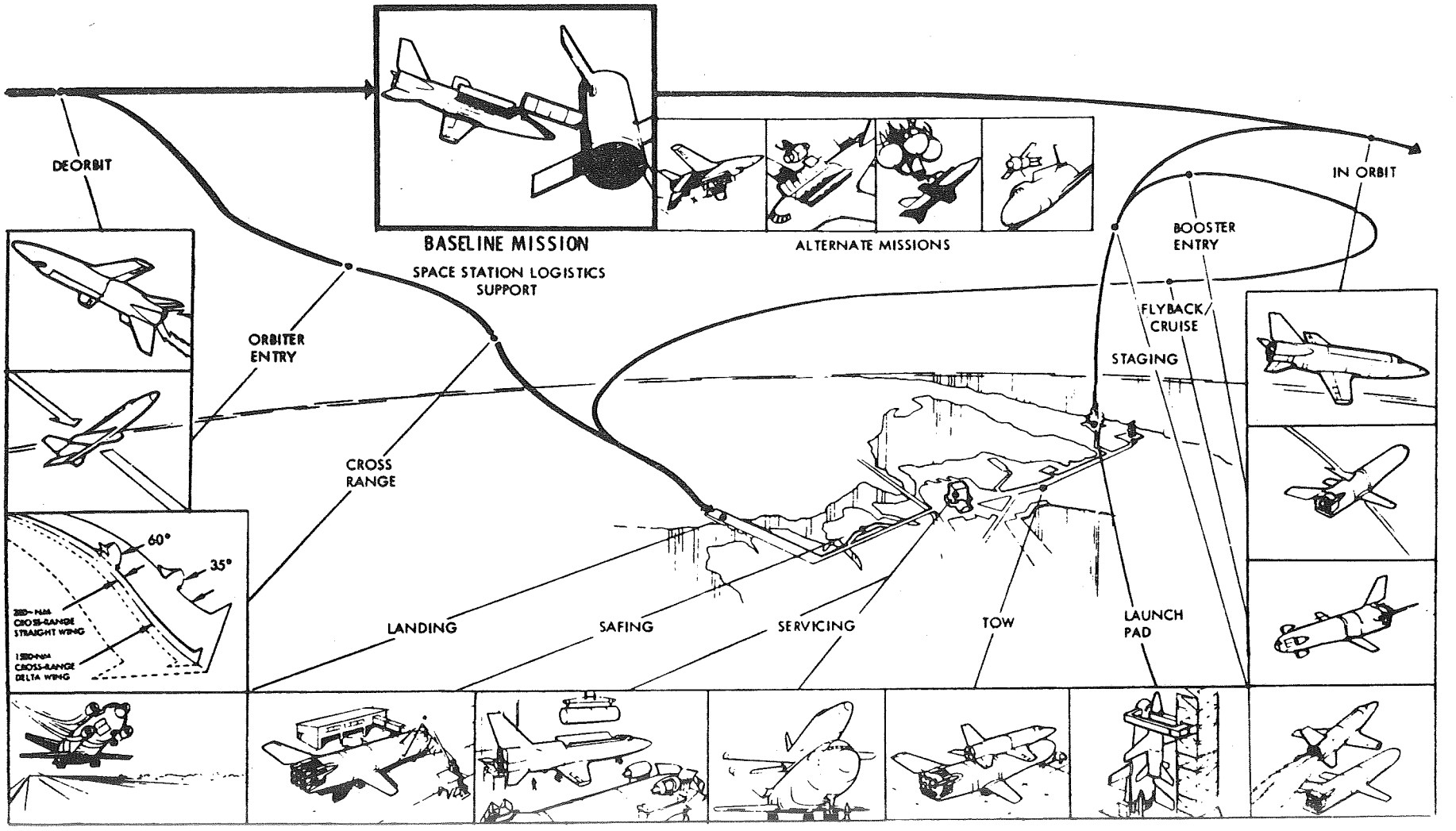

Figure 1-4. Mission Profile

The boost phase provides thrust for approximately 200 seconds of ascent flight. At approximately 220,000 feet altitude and 10,000 fps velocity the booster and orbiter separate. The boost phase includes a gliding turn for the booster back towards the launch site while the orbiter thrusts to orbit injection. The booster glides to an altitude of 20,000 feet and a velocity of approximately 300 knots at which time cruise turbofan engines are deployed and the vehicle cruises 400 n.mi. to the launch site. The orbiter performs its mission, enters the atmosphere and lands at a prescribed landing site.

Since the design load conditions occur at maximum launch dynamic pressure and maximum entry load factor, aerodynamic characteristics were developed for the combined launch configuration and for the individual elements at hypersonic speeds. Figures 1-5 and 1-6 present the pitch plane and lateral launch configuration aerodynamic characteristics, respectively. Table 1-1 presents the hypersonic characteristics for each element. For the entry condition, only static aerodynamic characteristics were developed because dynamic derivatives are extremely small when compared to the damping provided by the control system.

Table 1-1. Hypersonic Aerodynamic Characteristics

Booster		Orbiter
0.875	C_{L_α} = 60°	1.384
0.66 X/L	$C.P._\alpha$	0.637 X/L
0.26	$C_{L_{WING_\alpha}}$ = 60°	0.479
0.515	$C_{L_{BODY_\alpha}}$ = 60°	0.696
0.10	$C_{L_{HORIZ.TAIL_\alpha}}$ = 60°	0.209
0.55 X/L	$C.P._{BODY_\alpha}$	0.553 X/L
1.77	C_{D_α} = 60°	2.8
7120 ft^2	S (Reference Area)	7120 ft^2
2637 in.	L (Reference Length)	2068 in.

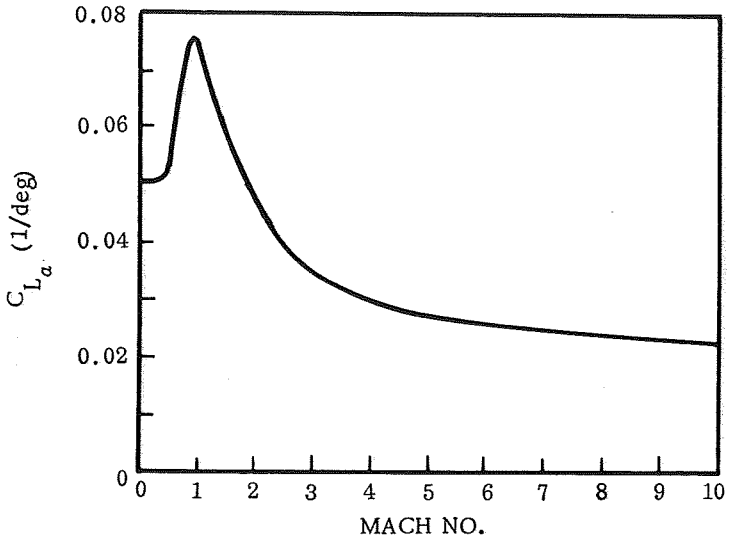

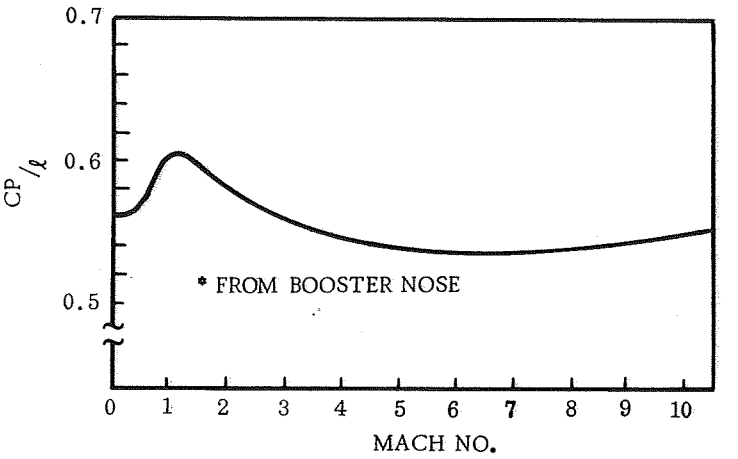

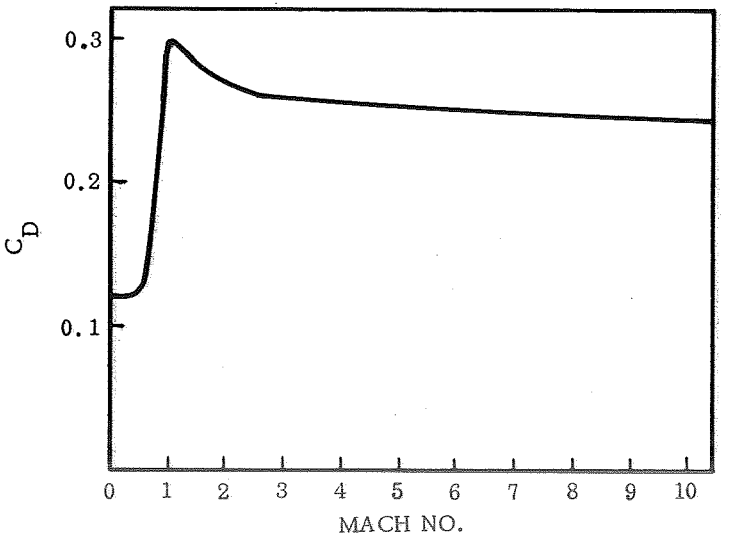

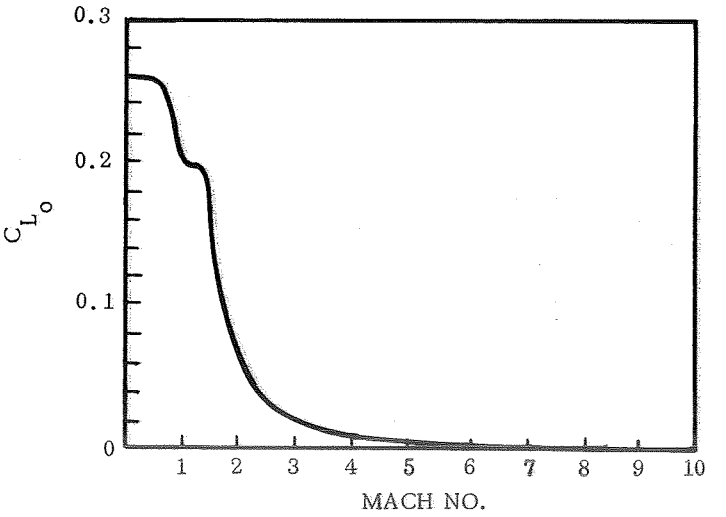

Figure 1-5. Pitch Plane Launch Configuration Aerodynamic Characteristics

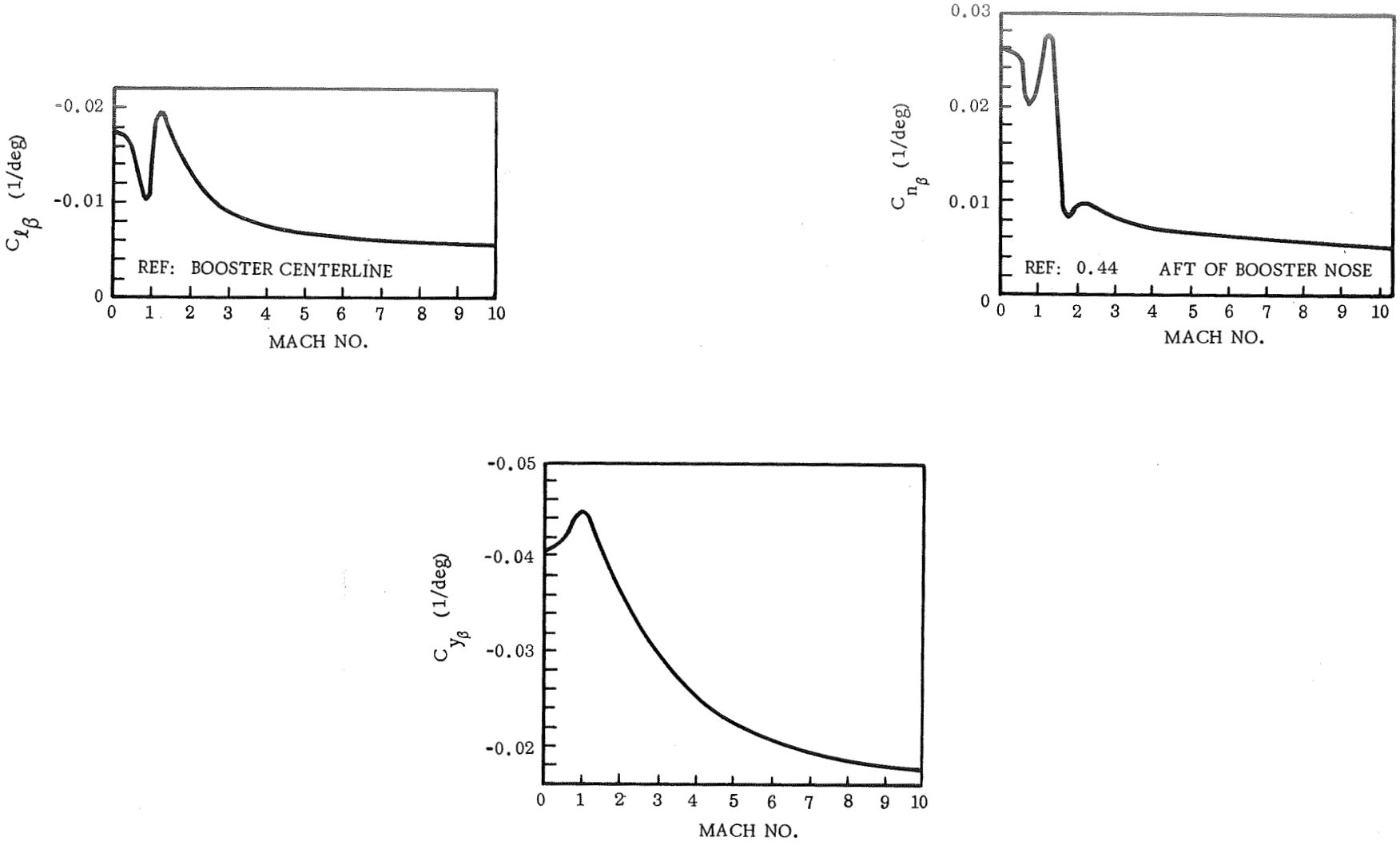

Figure 1-6. Lateral Launch Configuration Aerodynamic Characteristics

Inertia characteristics for the launch configuration are presented in Figure 1-7. As the fuel is depleted the center of gravity moves aft and towards the orbiter. The motion in the Z-direction is unique to the booster/orbiter configuration and it produces a component of thrust in the Z-direction which results in a no-wind angle of attack. The yaw and pitch mass moment of inertia is an order of magnitude greater than the roll moment of inertia. A sizable product of inertia exists due to the X-Z plane asymmetry. Ascent weight and thrust characteristics are presented in Figure 1-8.

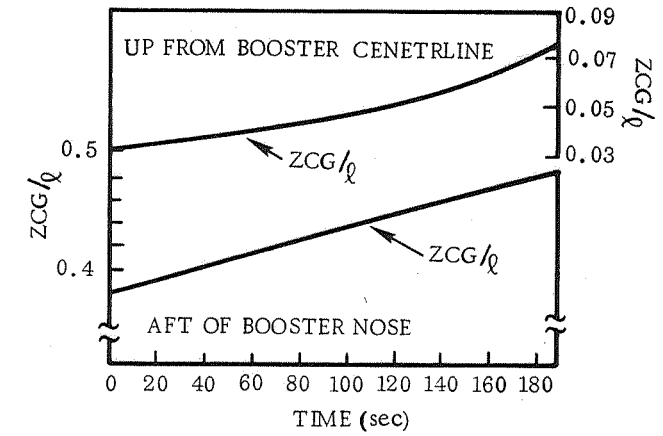

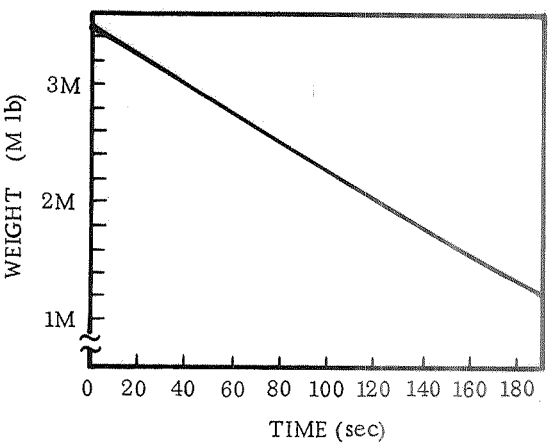

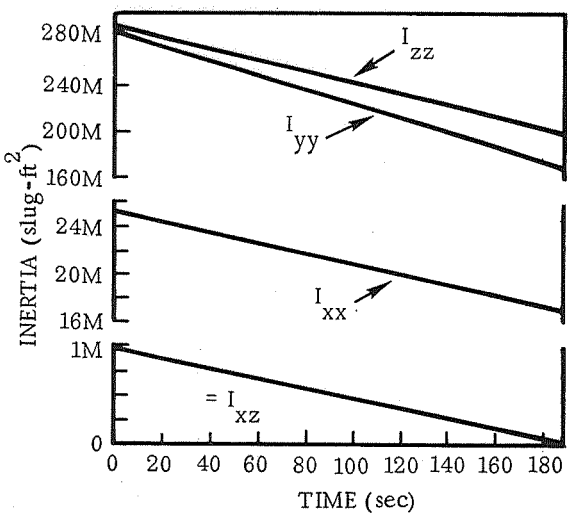

Figure 1-7. Launch Configuration Inertia Characteristics

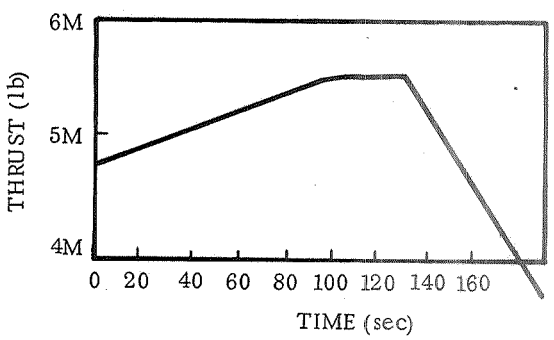

Figure 1-8. Thrust and Launch Configuration Weight Characteristics

1.4 ASCENT WINDS

A review of atmospheric disturbance models was made to select a realistic environment. The atmospheric disturbance model consists of wind and no-wind shears. The lateral loads computed for a boost vehicle during atmospheric flight are largely a function of the wind criteria used in the analysis. Many wind criteria have been developed for use in the aerospace industry in the past decade. The most commonly

used criteria is the Marshall Space Flight Center (MSFC) synthetic wind, Figure 1-9. The basic philosophy has been to use synthetic wind criteria during preliminary and start of final design to ensure consistent design inputs and to avoid the problems of oversight errors. Furthermore, synthetic wind criteria enable design teams to simultaneously conduct studies and compare results on a common basis. It is also desirable to simulate the vehicle flight and response to actual wind velocity profiles. These wind profiles must contain an adequate frequency content through at least the vehicle's first bending frequency.

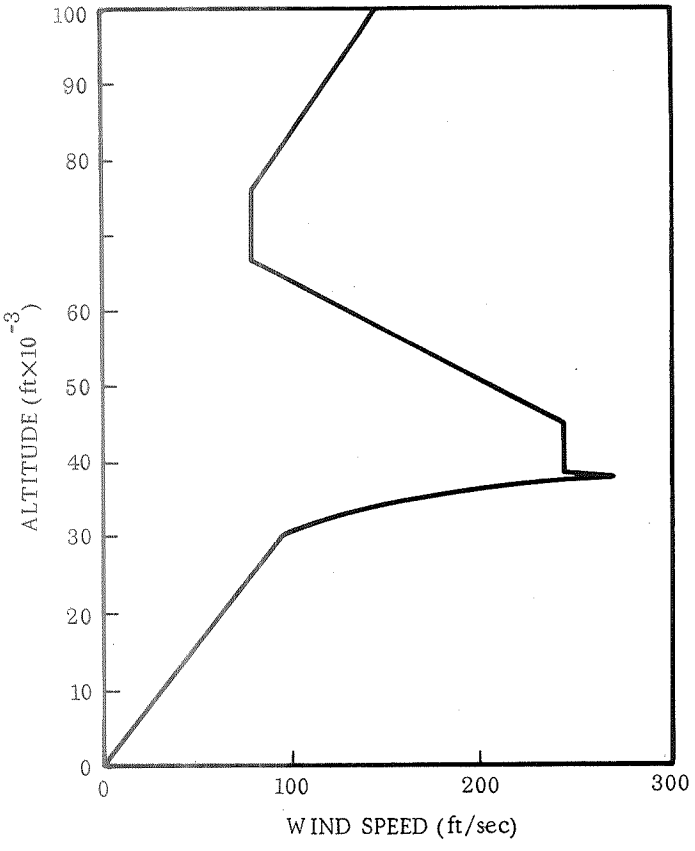

Figure 1-9. MSFC Synthetic Wind

A review was made of the Patrick Air Base (Atlantic Missile Range) winds (200) to select a managable number of wind profiles. Since the space shuttle will be launched throughout the year, the selected wind profiles were distributed throughout the calendar. These profiles which were selected in the winter and fall months were chosen with the knowledge that they had been critical for the Atlas and Atlas/Centaur launch vehicles. Table 1-2 lists the winds and Figures 1-10 through 1-18 present the nine selected profiles. The wind data includes wind speed and compass direction.

Table 1-2. AMR Real Winds Used In Study

No.	Wind
1	11 Jan 58
2	1 Jan 61
3	1 Feb 58
4	11 Feb 58
5	21 April 60
6	6 Aug 58
7	1 Aug 59
8	11 Nov 59
9	26 Nov 61

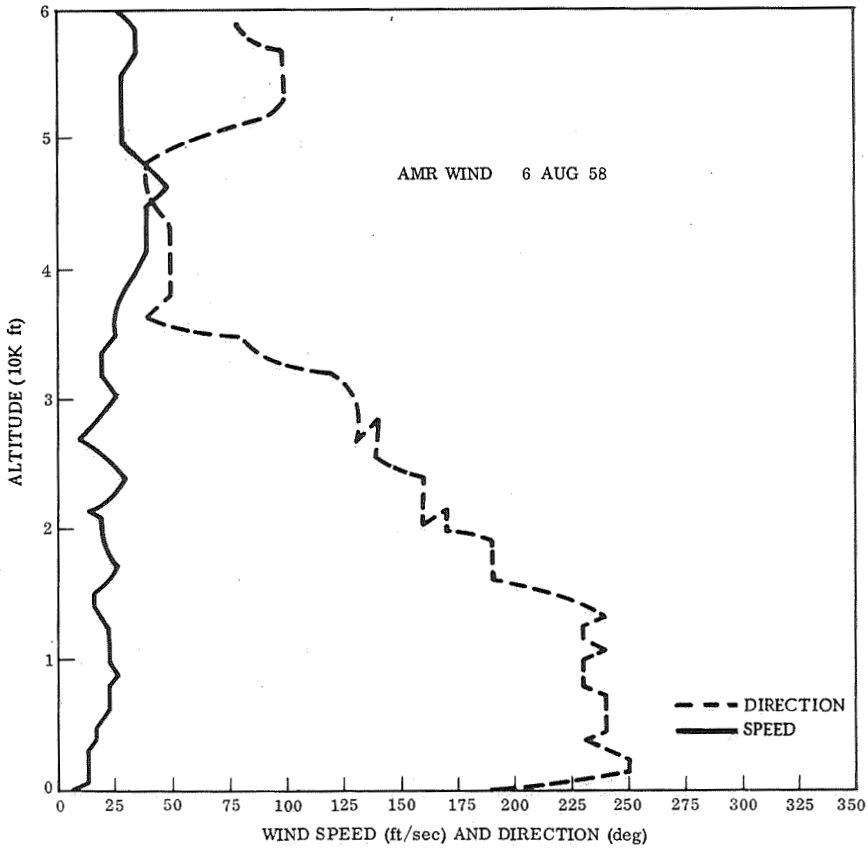

Figure 1-10. AMR Wind, 6 August 1958

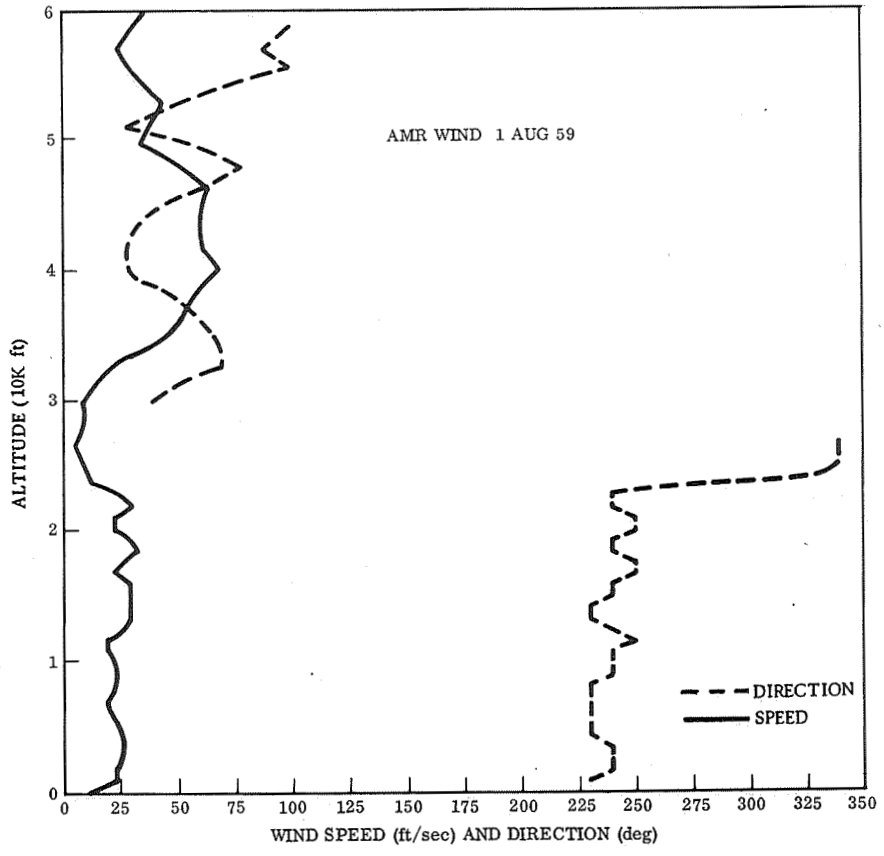

Figure 1-11. AMR Wind, 1 August 1959

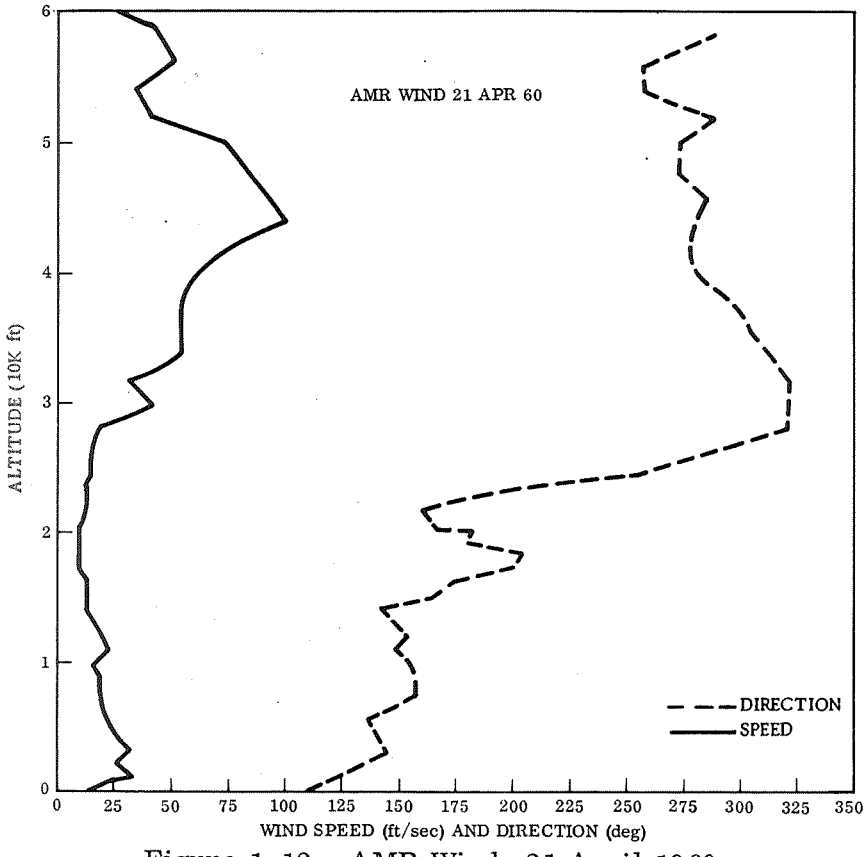

Figure 1-12. AMR Wind, 21 April 1960

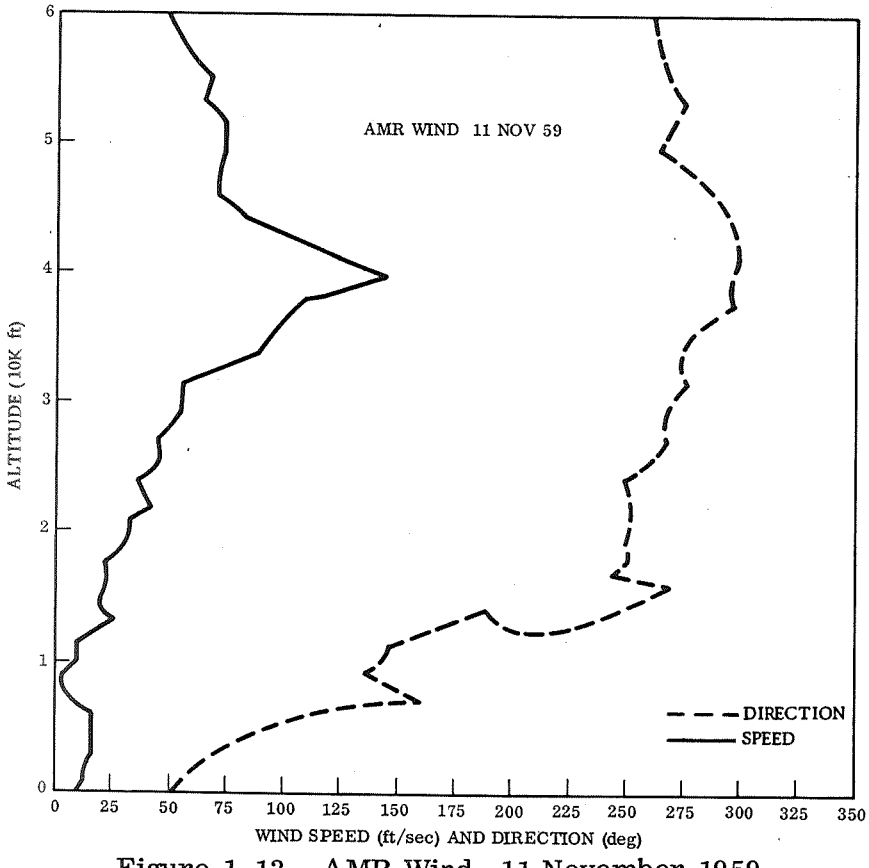

Figure 1-13. AMR Wind, 11 November 1959

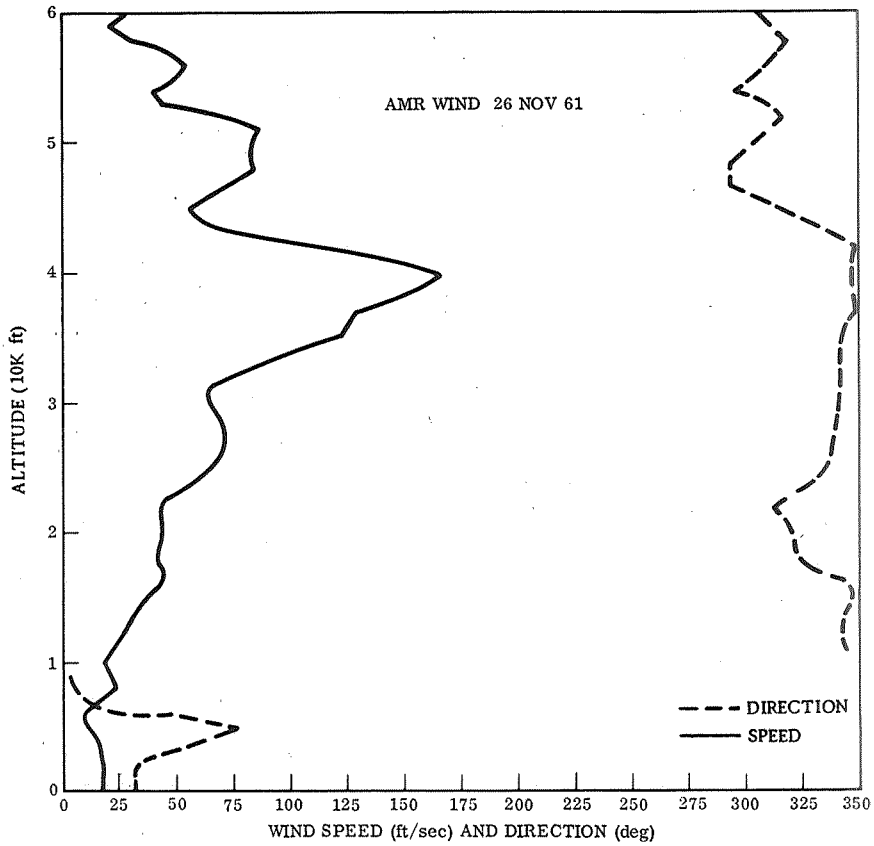

Figure 1-14. AMR Wind, 26 November 1961

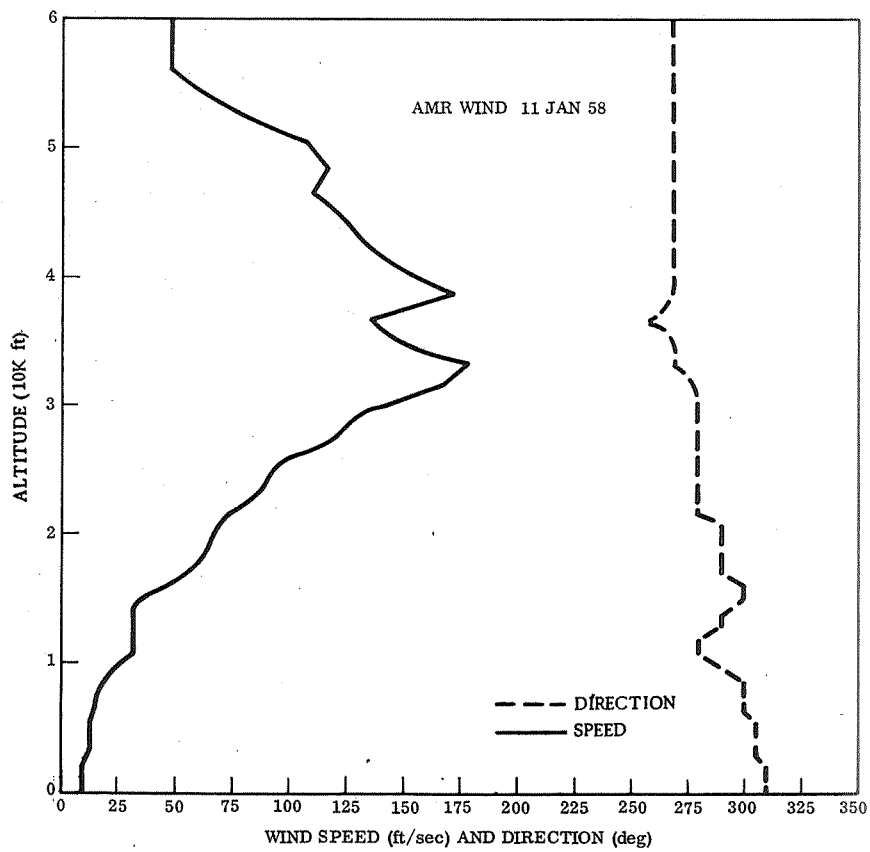

Figure 1-15. AMR Wind, 11 January 1958

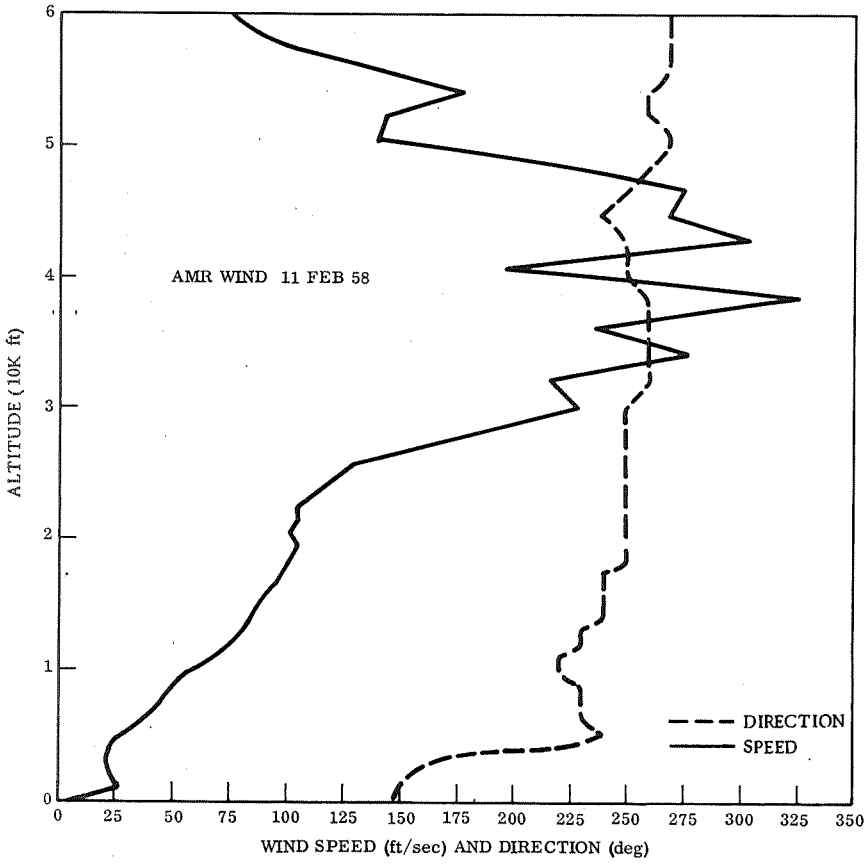

Figure 1-16. AMR Wind, 11 February 1958

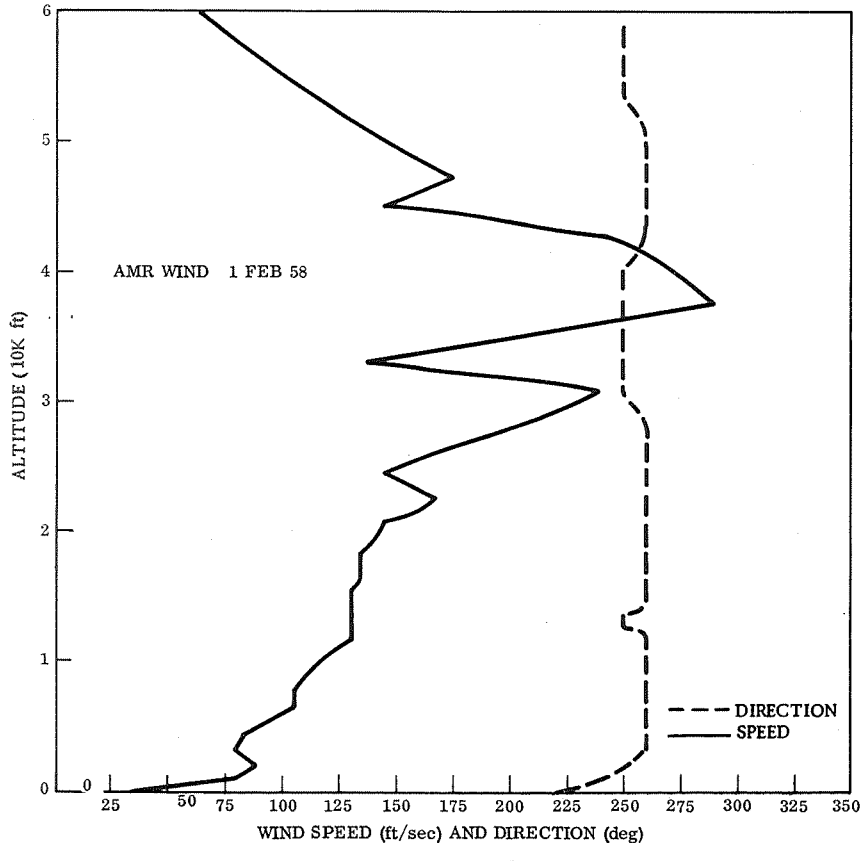

Figure 1-17. AMR Wind, 1 February 1958

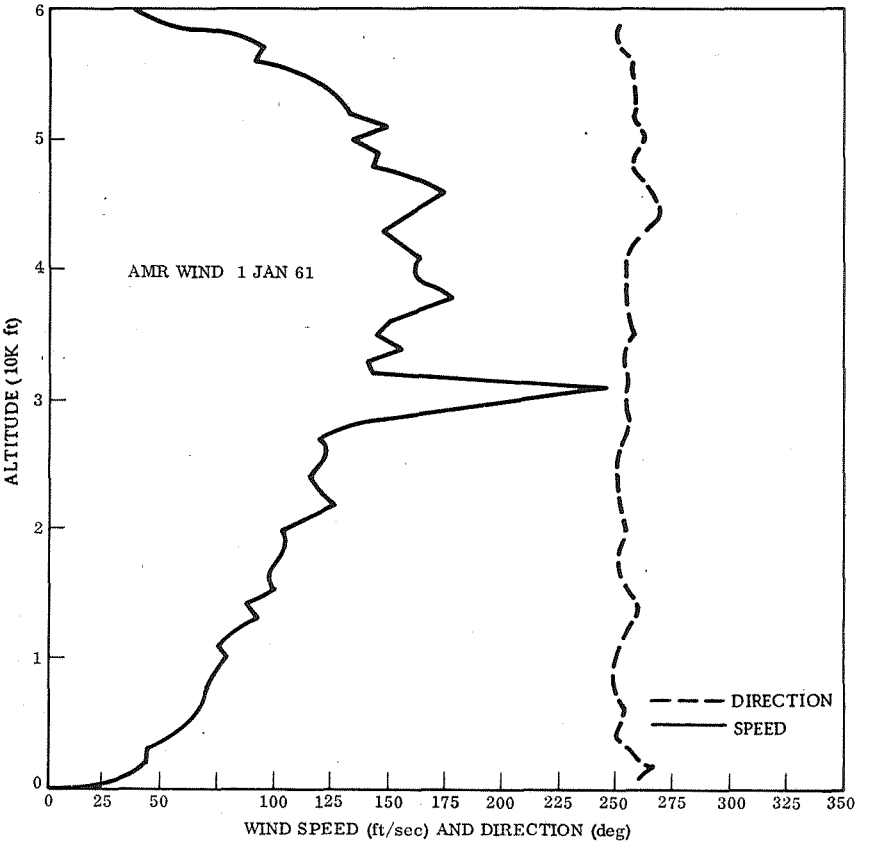

Figure 1-18. AMR Wind, 1 January 1961

1.5 REFERENCE TRAJECTORY

To conduct a loads analysis or a load alleviation analysis, a basic no-wind reference trajectory is necessary. Figures 1-19 through 1-23 present a reference trajectory for the pitch programmer presented in Figure 1-24. The gimbal angle (used for control by thrust vectoring) is about a fixed, 5-degree cant angle. This cant angle was determined such that the gimbal angle requirement for no winds at maximum dynamic pressure was near zero. The angle of attack time history shows the angle of attack to be approximately a constant negative three degrees up to 120 seconds and then it increases almost linearly to near minus ten degrees at burnout. The increase in angle of attack in the latter portion of the ascent flight is due to the off-center c.g. (center of gravity). The peak dynamic pressure is 560 psf and it occurs between 60 and 70 seconds, at approximately 35,000 feet altitude and a Mach number of approximately 1.2.

This trajectory was obtained by "flying" the pitch programmer presented in Figure 1-24. The pitch programmer was obtained from an optimum point mass trajectory program which considers the constraints of staging parameters (booster/orbiter separation) and orbital injection parameters. The pitch programmer was optimized

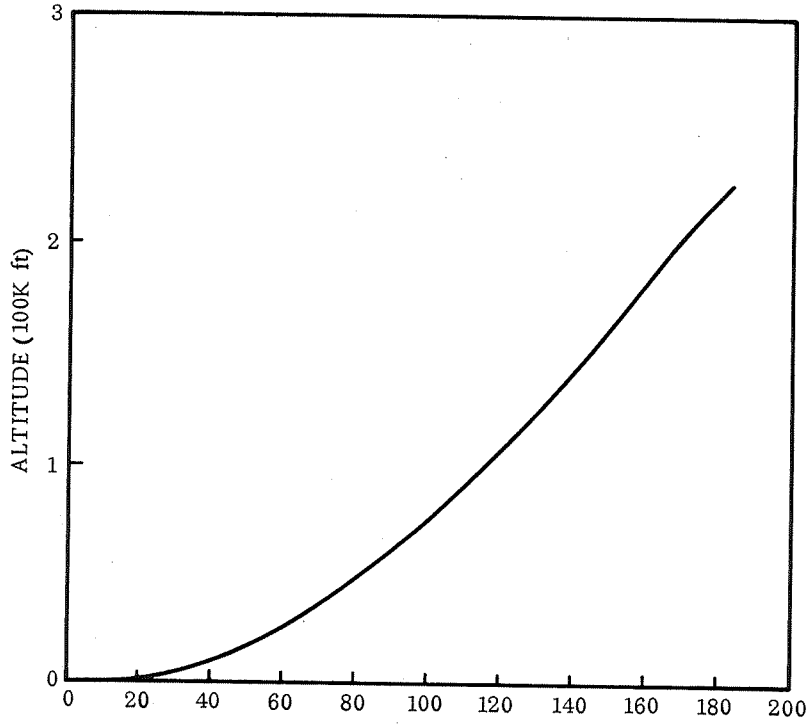

Figure 1-19. Reference No-Wind Trajectory — Altitude

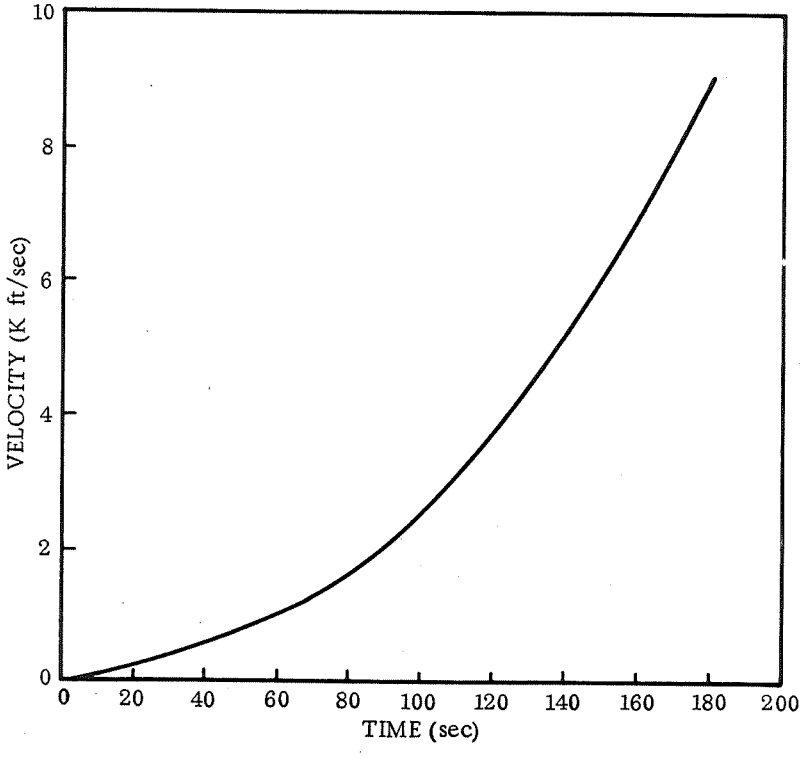

Figure 1-20. Reference No-Wind Trajectory — Velocity

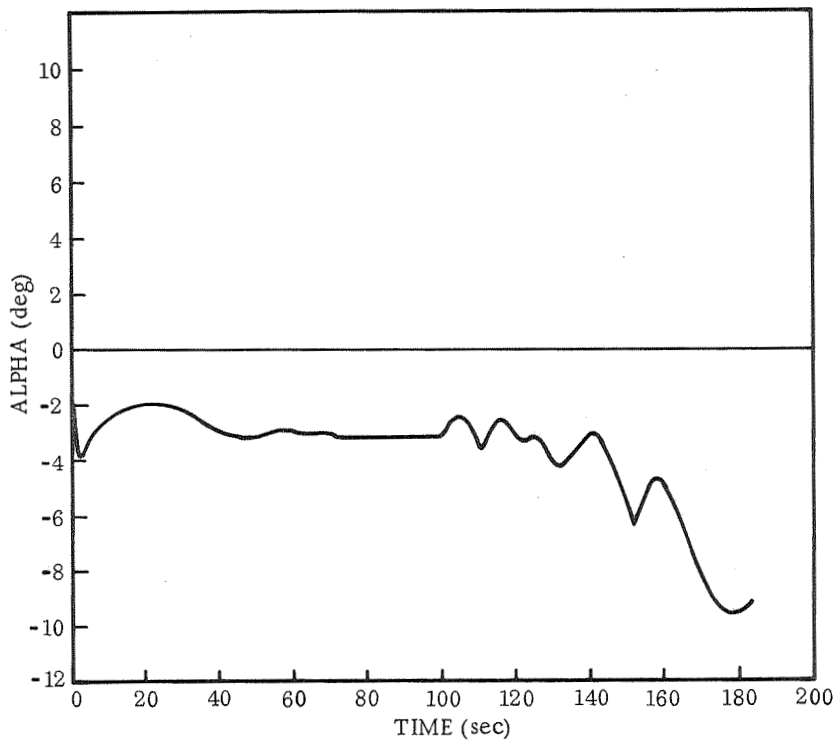

Figure 1-21. Reference No-Wind Trajectory — Angle of Attack

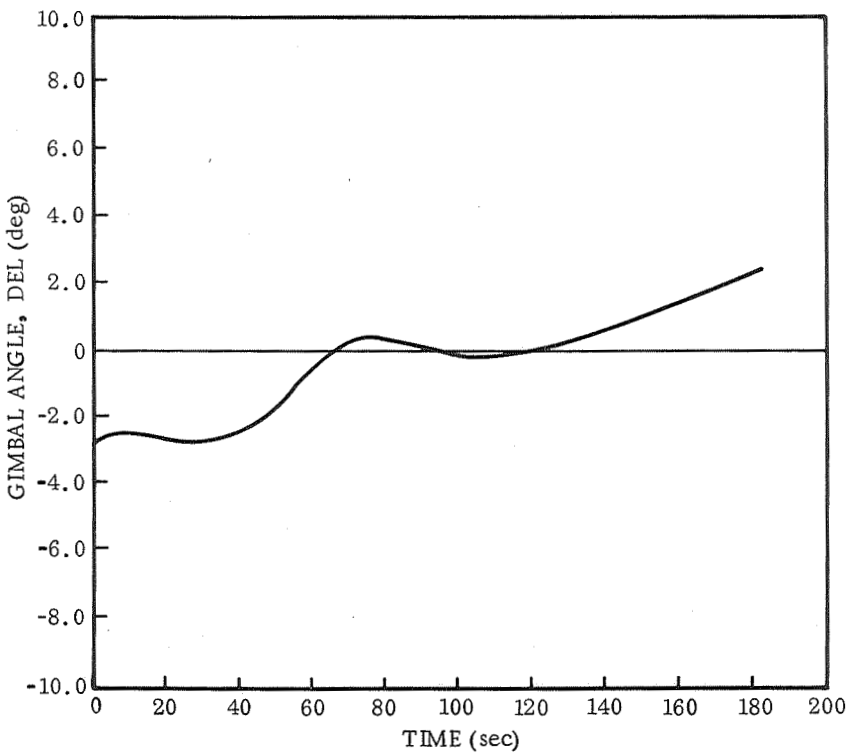

Figure 1-22. Reference No-Wind Trajectory — Gimbal Angle (From 5° of Cant)

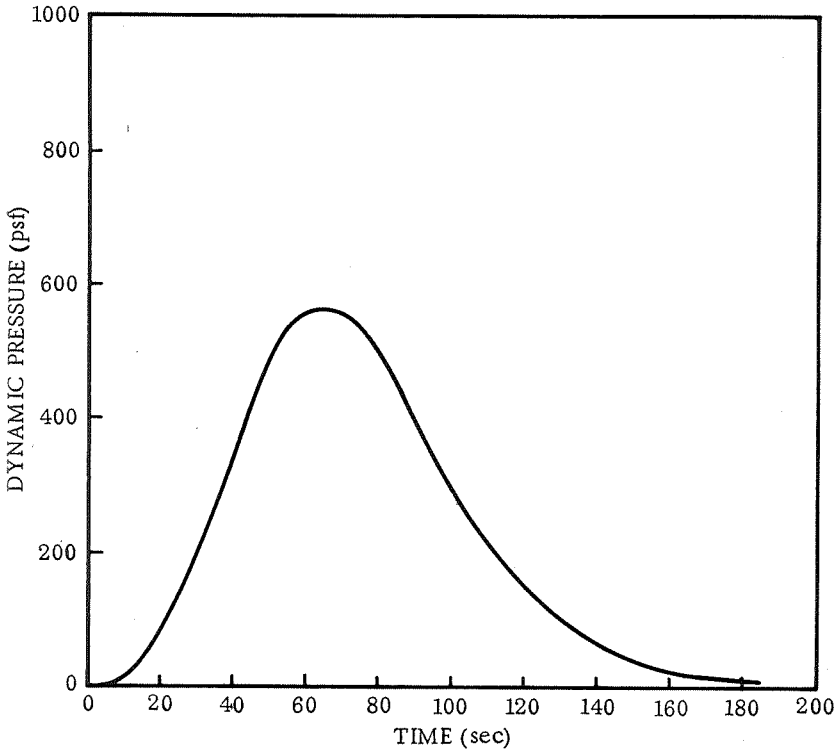

Figure 1-23. Reference No-Wind Trajectory — Dynamic Pressure

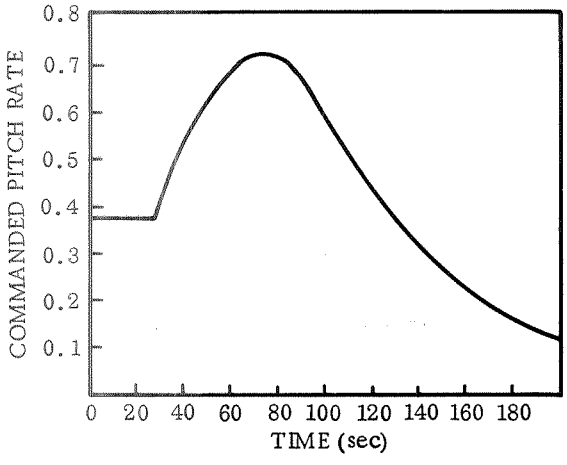

Figure 1-24. Reference Trajectory Pitch Programmer — Command Pitch Rate

to provide the maximum payload into orbit. The staging parameters considered were altitude, velocity, and flight-path angle. Altitude and velocity are critical to booster entry heating, and altitude and flight path angle are critical to booster cruise-back fuel requirements.

Because of the preceding staging requirements, all the trajectories developed in this study (including the no-wind reference trajectory) used a closed-loop guidance scheme which was activated 100 seconds into the ascent flight. The scheme used the reference trajectory technique to guide to a nominal staging altitude, velocity, and flight-path angle. An incremental pitch rate command ($\Delta\dot{\theta}_c$) was generated by

$$\Delta\dot{\theta}_c = C_V (V - V_N) + C_{\dot{\gamma}} (\dot{\gamma} - \dot{\gamma}_N) + C_\gamma (\gamma - \gamma_N)$$

Where

V_N, γ_N, $\dot{\gamma}_N$ are nominal values

C_V, C_γ, $C_{\dot{\gamma}}$ are linear functions of altitude

C_V = -0.008 at 70K ft

C_γ = -0.20 at 70K ft

$C_{\dot{\gamma}}$ = -6 at 70K ft

C_V = 0 at 215K ft

C_γ = -1.0 at 215K ft

$C_{\dot{\gamma}}$ = -10 at 215K ft

Nominal Staging Conditions

T = 187.895 sec

V = 9456 ft/sec

H = 210,101 ft

γ = 8.9036 deg

For the yaw plane guidance, an incremental commanded yaw rate ($\Delta\dot{\Psi}_c$) was generated by

$$\Delta\dot{\Psi}_c = \dot{\theta}_c \cdot \text{TAN}(\phi) + C_{CR} \cdot CR + C_{CRDOT} \cdot CRDOT$$

Where

ϕ = roll angle

CR = cross range distance

CRDOT = rate of cross range distance

C_{CR}, C_{CRDOT} are linear functions of altitude

C_{CR} = 0.0000001 at 70K ft

C_{CRDOT} = 0.00111 at 70K ft

C_{CR} = 0 at 230K ft

C_{CRDOT} = 0.00111 at 230K ft

The overall guidance cycle time was one second. With this type of guidance, performance penalties in terms of added propellant requirements can be obtained. The cut-off for staging is velocity and the performance penalty is obtained by differencing the propellant consumed for the particular run with the nominal no-wind reference trajectory propellant consumption.

Figures 1-25 through 1-33 present angle of attack, αq, and gimbal angle time history for the reference trajectory with MSFC headwinds, MSFC tailwinds, and a typical "real" wind. For the MSFC winds the gust and peak wind was applied at maximum dynamic pressure. The wind was a 95% wind profile with a 99% wind shear build-up and a 7.65 meters per second gust. The maximum αq for this reference trajectory is -3700 psf-deg and it occurs for the MSFC tailwind.

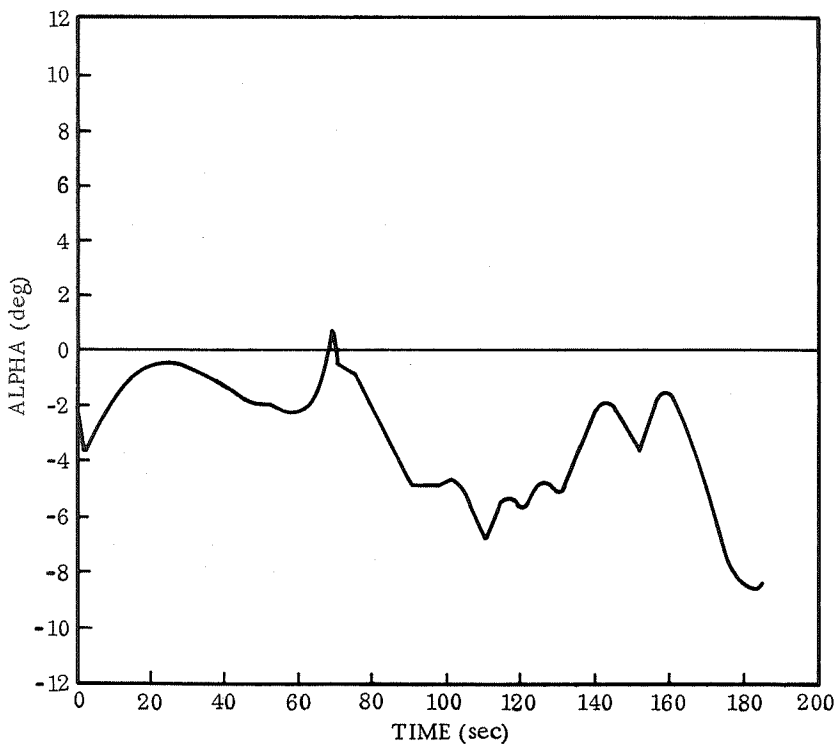

Figure 1-25. Marshall Headwind — Alpha

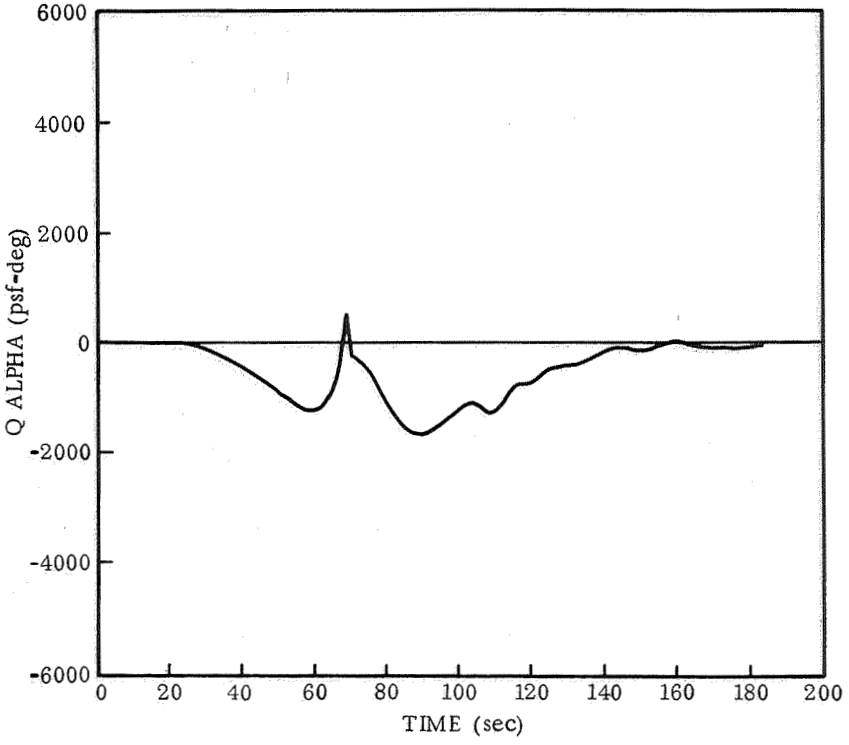

Figure 1-26. Marshall Headwind — Q Alpha

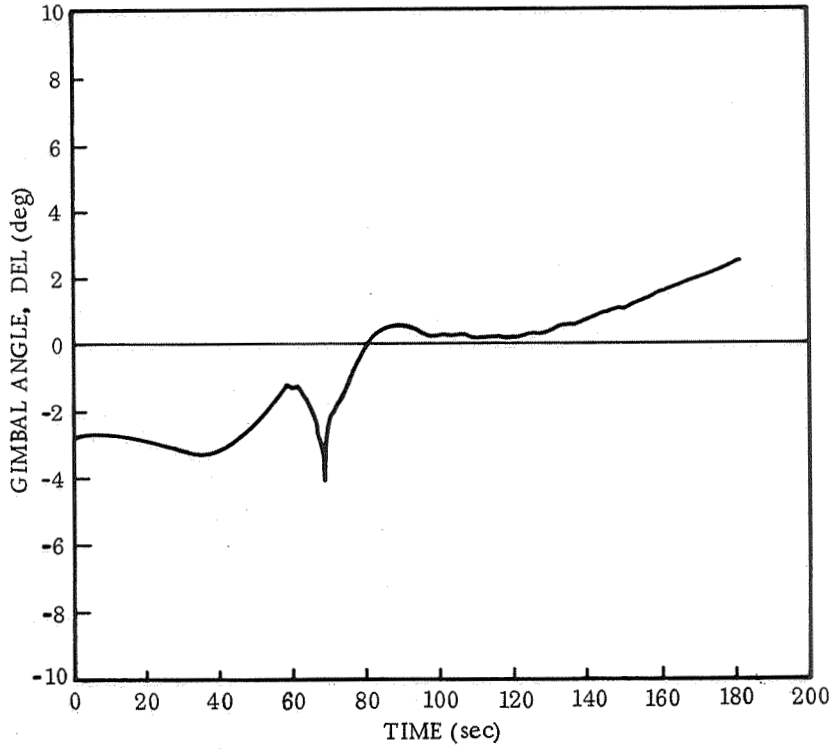

Figure 1-27. Marshall Headwind — Gimbal Angle

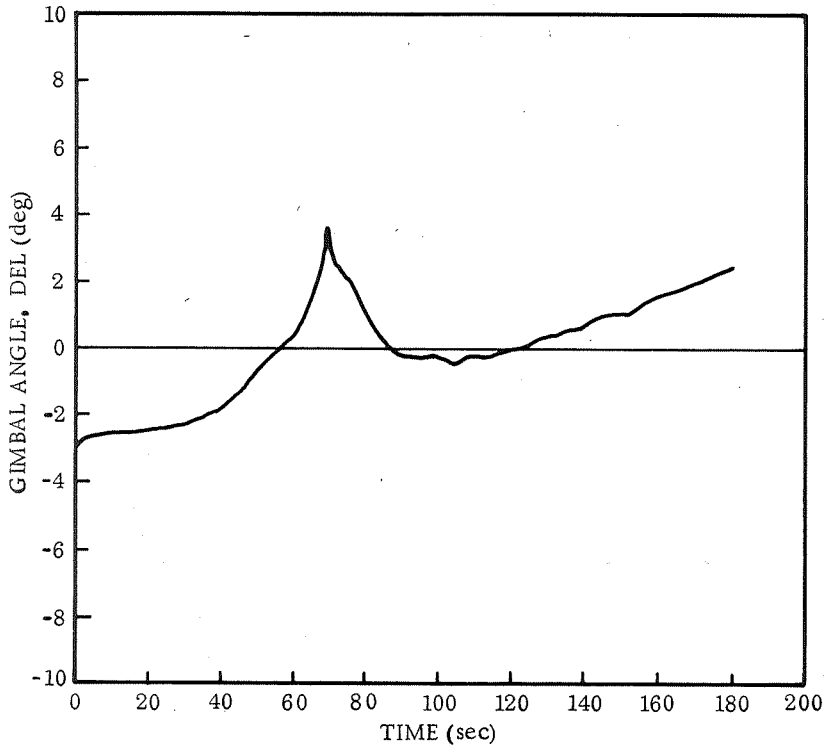

Figure 1-28. Marshall Tailwind — Gimbal Angle

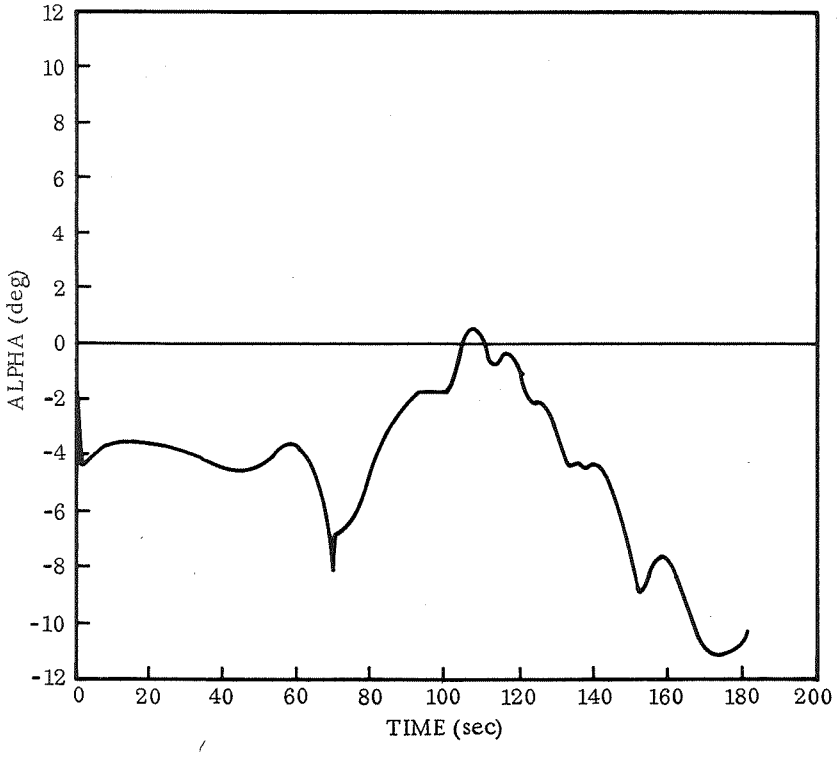

Figure 1-29. Marshall Tailwind — Alpha

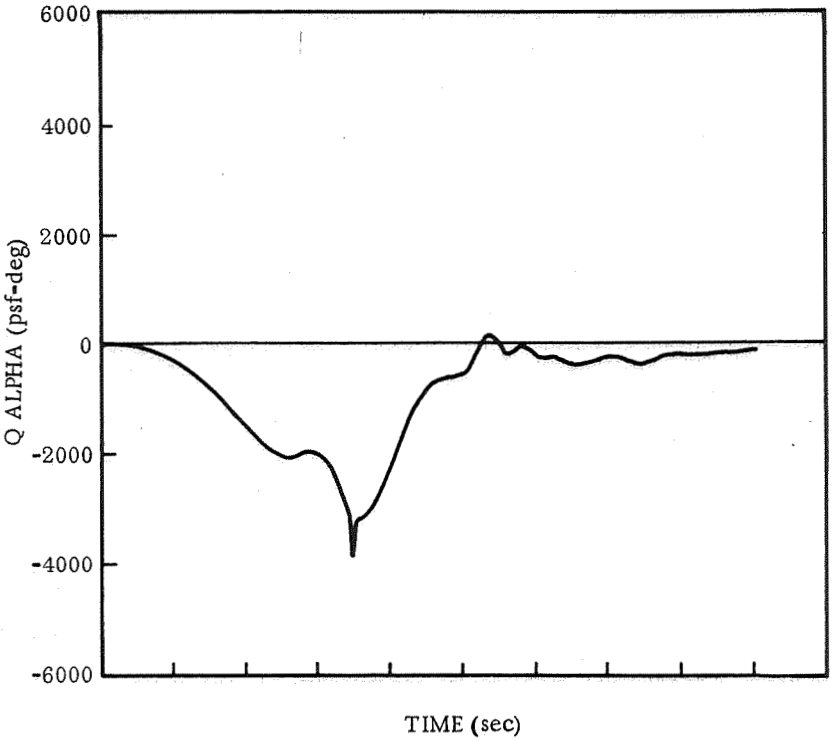

Figure 1-30. Marshall Tailwind — Q Alpha

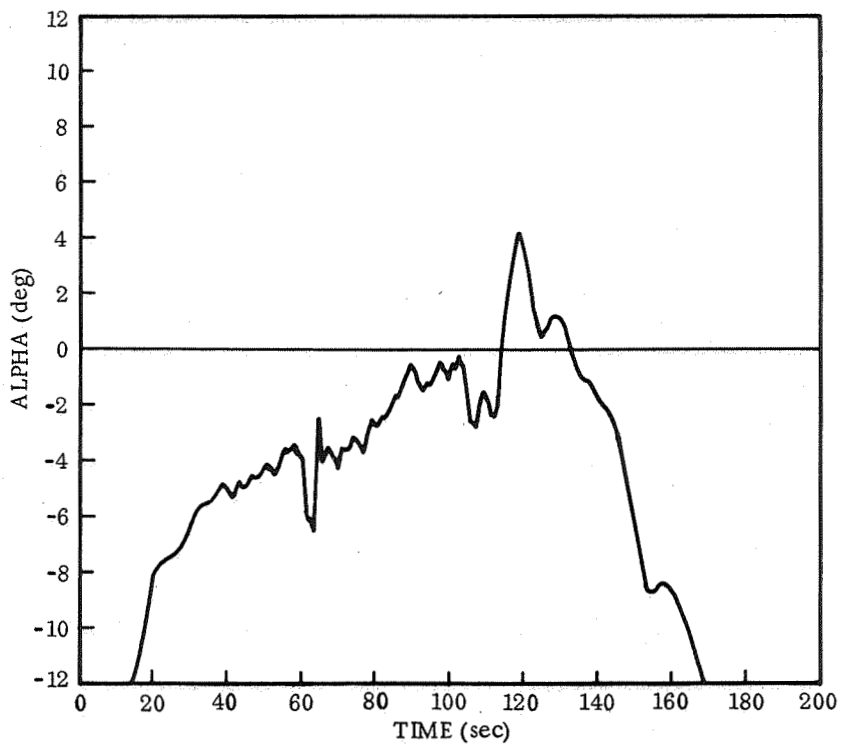

Figure 1-31. Real Winds - AZ = 90 - Alpha

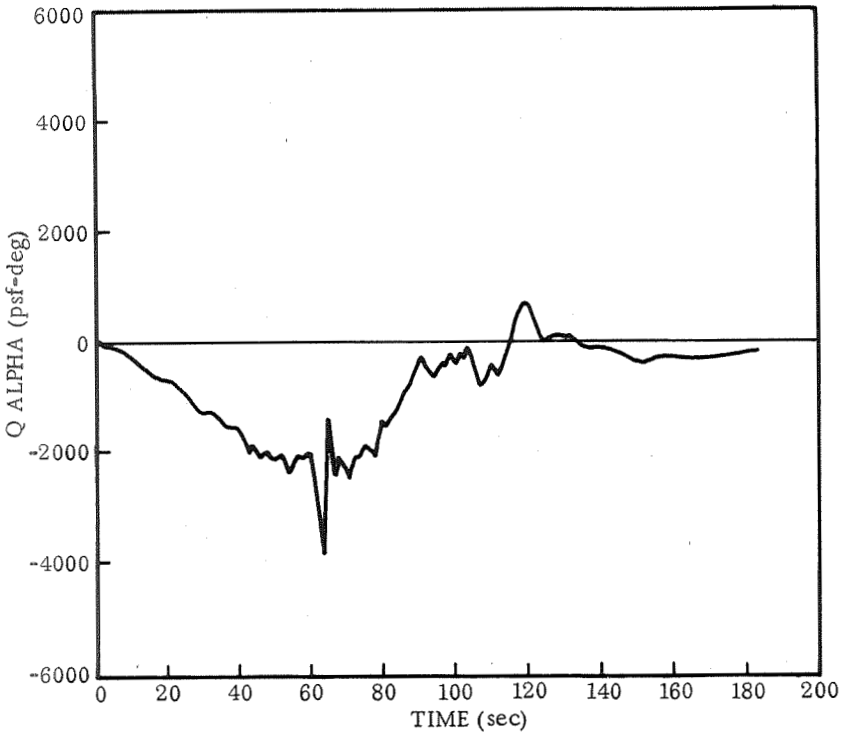

Figure 1-32. Real Winds - AZ = 90 - Q Alpha

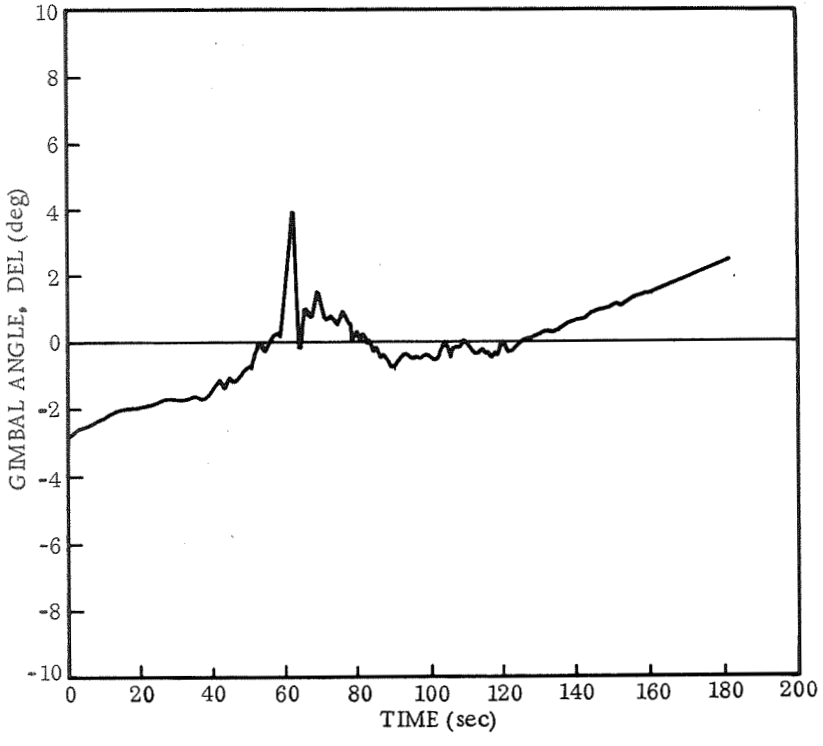

Figure 1-33. Real Winds - AZ = 90 - Gimbal Angle

SECTION 2

RIGID BODY LOAD ALLEVIATION

Load alleviation can be accomplished by: trajectory biasing, limiting gimbal angle, angle of attack of normal acceleration feedback, and by reduction in pitch attitude feedback. Associated with each load alleviation scheme is a performance penalty which will be measured in terms of propellant. Since the design load conditions include entry loads, structural weight savings is not a direct function of ascent load reduction. In fact this study has demonstrated that minimum material gage begins to cloud the load/structural weight relationships.

2.1 TRAJECTORY BIASING

A common method of reducing ascent loads is by trajectory biasing or more descriptively, tailoring the pitch programmer based on a priori knowledge of the wind direction and profile. This load reduction technique has been used on Atlas/Centaur and Saturn vehicles with good success. The basic principle is to have the vehicle pitching into the wind for a headwind, and to minimize the pitch-over for a tailwind.

Figure 2-1 presents six candidate pitch programmer time histories for a two-element space shuttle vehicle. Table 2-1 presents a summary of load and performance penalties for each of the pitch programmers. Each programmer showed a reduction in αq max for flight times below 100 seconds. However, some programmers showed αq greater than the nominal 3700 psf-deg for ascent flight times greater than 100 seconds. This large load at low dynamic pressure was due to commands from the guidance system which were attempting to steer the vehicle to the desired staging point. They can be reduced by introducing the guidance at an earlier time (85 seconds) and by blending the guidance signal into the open-loop pitch command. However, these results give an indication of the trajectory dispersions caused by the biased pitch programmer. The performance penalty indicator also bears out these conclusions. The increased propellant requirements ranged from 13,000 to 40,000 pounds. It should be noted that booster propellant converts to payload by a 1:14 ratio. Therefore, 13,000 pounds of added fuel represent approximately 1000 pounds of payload.

2.2 GIMBAL ANGLE LIMITING

Most of the clustered reusable launch vehicles are aerodynamically stable during the ascent high dynamic pressure region of flight. The flight control system can make use of this characteristic by software limiting the gimbal angle command to some predetermined value. Then, as the wind induced pitching moment builds up, the vehicle will rotate into the wind and thereby reduce the angle of attack. The associated load reduction must be weighed against the performance penalty produced by excursions

Table 2-1. Trajectory Biasing Performance

PITCH* PROGRAM	Δ WEIGHT PENALTY (EFFECTIVE PROPELLANT) (lb)	ALT. ERROR (ft)	γ ERROR DEG.	αQ MAX PSF-DEG	
				t < 100	t > 100
1	40353	3154	-1.5	2700	5227
2	18941	1943	-1.0	2351	
3	27353	1729	-1.25	1700	3273
4	28224	2151	-1.27	2700	3973
5	28811	2338	-1.25	1750	3919
6	13213	1779	-0.76	1294	
NOMINAL	0	120	-0.03	3637	

*The AMR 1 January 1961 winds were used throughout

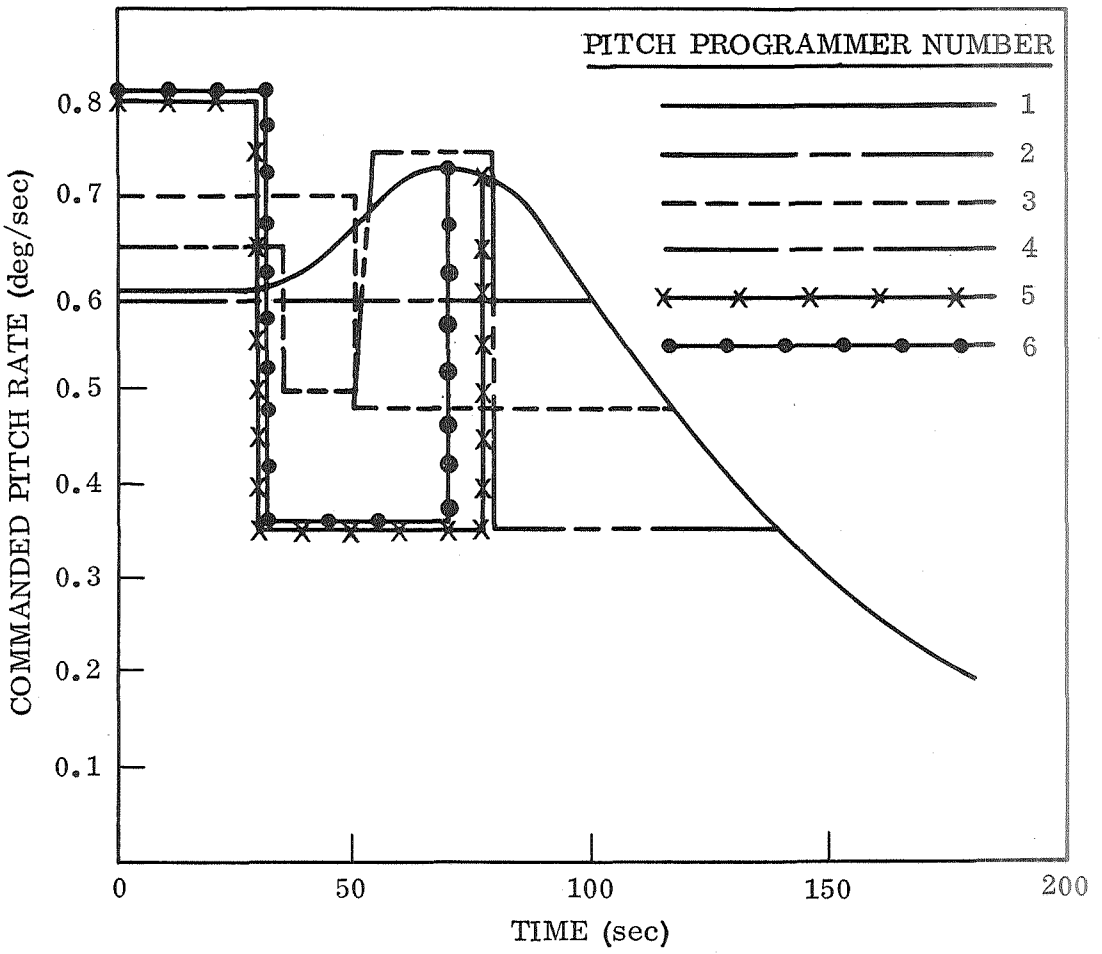

Figure 2-1. Various Pitch Programmer Schedules

from the near optimum reference trajectory. Table 2-2 summarizes the results for limiting the absolute value of the gimbal angle to 0°, 0.5°, 1.0° and 2.0° during the time interval of 50 to 110 seconds. This type of load reduction appears attractive because of the low performance penalty (approximately 3000 pounds of propellant) and the reasonable load reduction of approximately 25%.

Preliminary analysis shows potential for this load reduction technique, but since this scheme is very sensitive to vehicle inertia and aerodynamic characteristics care must be given to broadly extrapolating these conclusions to other configuration. Each particular configuration must be investigated by simulations to determine the amount of load reduction that can be obtained by gimbal angle limiting.

2.3 ANGLE OF ATTACK COMMAND

Theoretically it is possible to "fly" constant angle of attack trajectories (α = +1, 0, -1). The fundamental laws which must be satisfied for such a scheme are (for α = 0)

Table 2-2. Gimbal Angle Limiting Performance

LIMIT VALUE	Δ WEIGHT PENALTY (lb)	ALT. ERROR (ft)	γ ERROR (deg)	αQ MAX PSF-DEG.*
0°	4500	829	-0.32	3400
0.5°	3000	131	-0.33	3000
1°	3000	369	-0.34	2700
2°	3000	108	-0.34	3100

*The AMR 1 January 1961 wind was used

$$\alpha = \frac{w}{V_T} = 0 \quad \text{or} \quad w = 0$$

where

w is the body Z component of velocity

V_T is the total vehicle velocity

if $w = 0$ then $\dot{w} = 0$

but $\dot{w} = \frac{\Sigma F_Z}{m} + U\dot{\theta}$

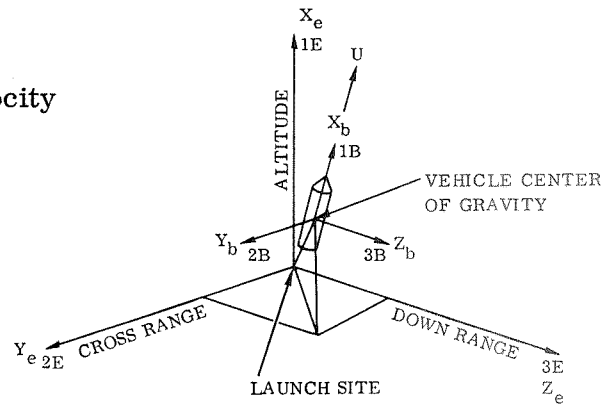

Sign Convention

where

ΣF_Z is the summation of external forces along the body Z-axis

m is the mass

U is the body X component of velocity

if $\dot{w} = 0$

then $\frac{\Sigma F_Z}{m} = -\dot{\theta} U$

or $= \dot{\theta}_c = -\dot{\theta} = \frac{\Sigma F_Z}{mU}$

if $\Sigma F_Z = K_1 \alpha + K_2 + K_3 \delta$ and $\alpha = 0$

then a command pitch rate can be found which produces the constant $\alpha = 0$ constraint. This is especially true since $\dot{\theta}_c$ directly controls the gimbal angle (δ) time history.

Launch towers and offset center of gravities at lift-off preclude use of the above law prior to 30 seconds of flight. Therefore, a constant command pitch rate is used during the time. Figure 2-2 presents a family of trajectories for zero command angle of attack and various initial commanded pitch rates. Note that only one initial commanded pitch rate approaches the near optimum reference trajectory. Table 2-3 summarizes the results of constant angle-of-attack commanded systems. Large performance penalties are incurred because the pitch rate necessary for the constraint is

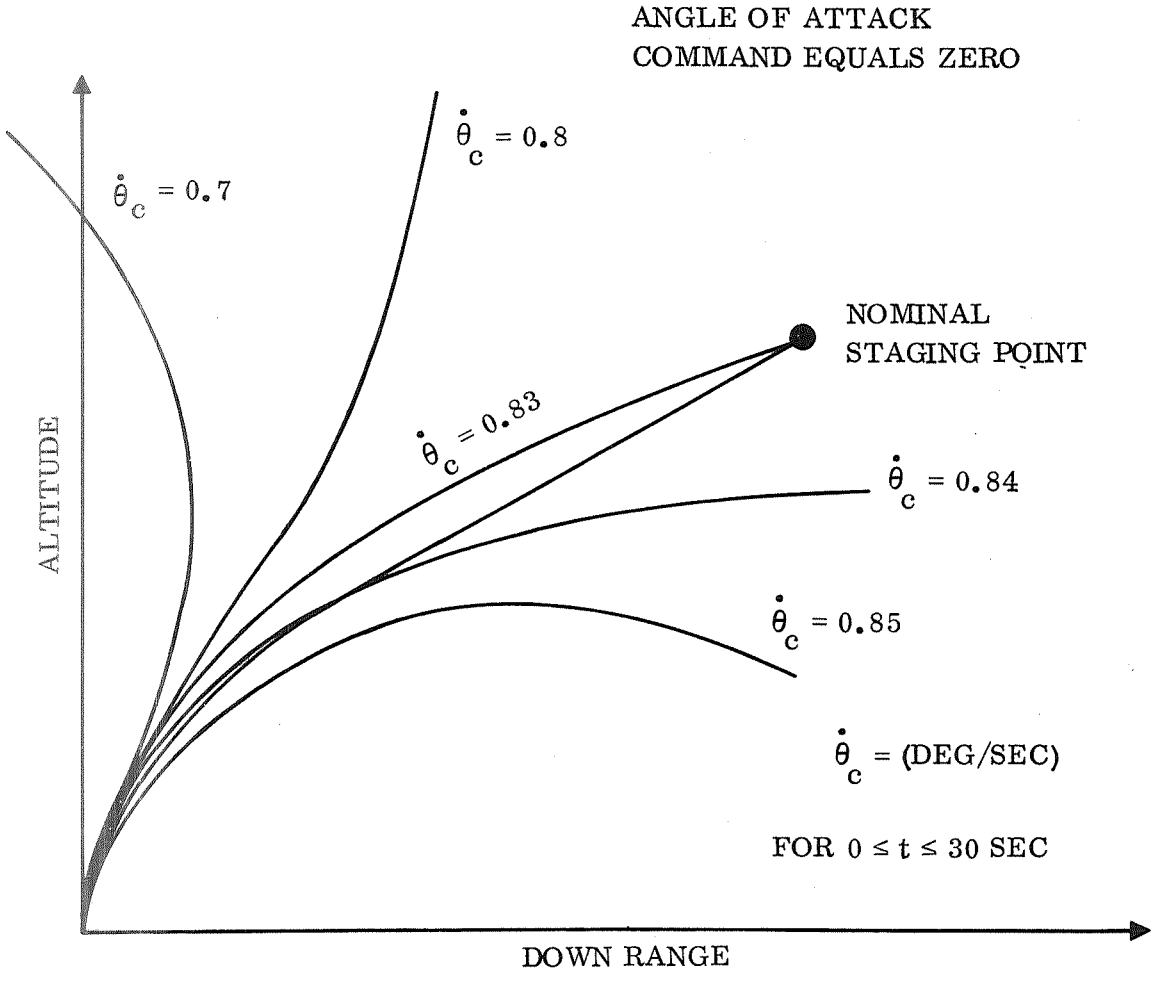

Figure 2-2. Family of $\alpha_c = 0$ Trajectories

considerably different from the near optimum reference trajectory. Load reductions are in order of 50% to 60% with the performance penalties between 20,000 and 30,000 pounds of propellant.

2.4 GAIN SCHEDULING AND ACCELEROMETER FEEDBACK

Load reduction can be achieved by reducing the pitch attitude gain during peak dynamic pressure and wind shears. This technique makes use of the aerodynamically stable vehicle characteristics. The gains can be scheduled as shown by this sketch.

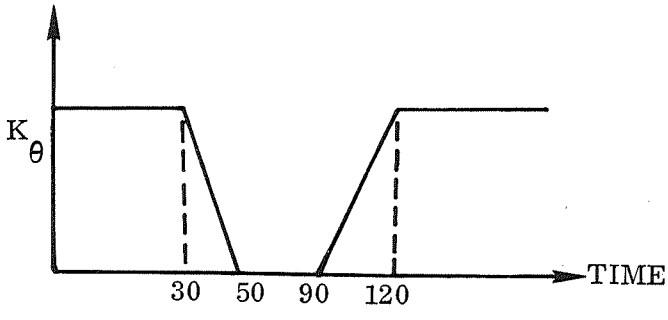

Table 2-3. Angle of Attack Command Performance

α COMMAND (deg) *	Δ WEIGHT PENALTY (lb)	ALT ERROR (ft)	γ ERROR (deg)	αQ MAX PSF-DEG
-1	32000	-17000	-6.8	2200
0	21000	5650	2.8	1925
+1	22000	13000	4.9	1800

* AMR 1 January 1961 wind was used

The attitude gain can be rapidly reduced to zero without difficulty. However, the gain must be phased in so that dynamic transients will not produce severe load conditions. With this technique, a 25% load reduction was attainable with only a 3000- to 4000-lb performance penalty.

Studies have been conducted for aerodynamically unstable launch vehicles which conclude that load reduction can be obtained when normal acceleration is fed back into the flight control system. For unstable vehicles, as the load builds up the pitching moment tends to increase the angle of attack. Therefore, normal acceleration is sensed and is used to gimbal the engines to counter the aerodynamic moment. Acceleration feedback was added to the space shuttle vehicle flight control system by the control law,

$$\delta_c = q + k\theta + \frac{0.1 K_A A_{ZCG}}{s + 1}$$

where

δ_c = gimbal angle command

q = pitch rate

θ = pitch attitude

K = pitch attitude gain

K_A = accelerometer gain

A_{ZCG} = acceleration at the vehicle center of gravity

s = Laplace operator

For the AMR January wind profile, the pitch gain follows the schedule previously presented and the accelerometer gain is scheduled as

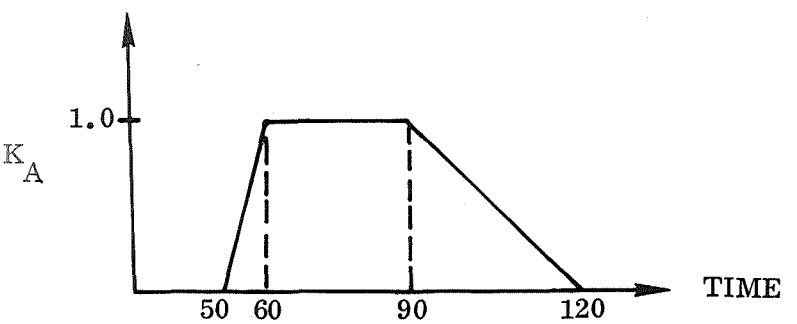

Based on the limited work performed in this study, there appears to be no significant improvement in load reduction nor increased performance penalty with acceleration feedback when combined with gain scheduling for the space shuttle vehicle. Because of static stability, the vehicle response to aerodynamic moment is approximately the same as the flight control system with acceleration feedback and therefore the rotation into the wind (weather cocking) is not improved. However, a detailed study may arrive at a combination of filters which can provide sufficient level on the accelerometer signal and thereby improve overall vehicle response. Pitch attitude gain scheduling can potentially reduce load by approximately 25 percent.

2.5 LATERAL LOAD REDUCTION WITH β FEEDBACK

Reduction of the side-slip angle is necessary for the space shuttle because of lateral control power limitation. A side view of a two element space shuttle configuration shows a large aerodynamic area above the center of gravity. The result is a large rolling moment due to side slip (C_{l_β}). With limited gimbal angle deflections ($\pm 10°$) large side-slip angles produce rolling moments which are much greater than those produced by gimballing the thrust vector. The sketch below shows the gimballing sequence for providing roll, yaw, and pitch control for the baseline configuration and the engine arrangement.

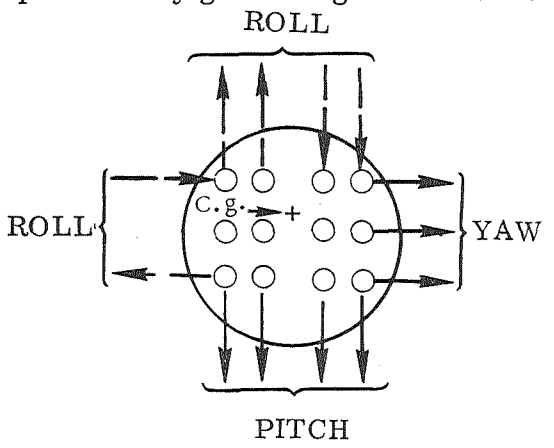

Reduction of side-slip angle (β) can be provided by feeding back β and reducing the yaw attitude gain. As β is fed back, yaw attitude must be reduced because otherwise they will buck each other. As the vehicle yaws to reduce β, an error in heading is detected and, if yaw attitude were still being fed back, the command would try to yaw the vehicle back to the correct heading. The result would be no real reduction in β.

A 36% reduction in β was realized by using

$$K_\beta = \frac{1.5\,\bar{Q}}{650}$$

where $\bar{Q}$ = dynamic pressure

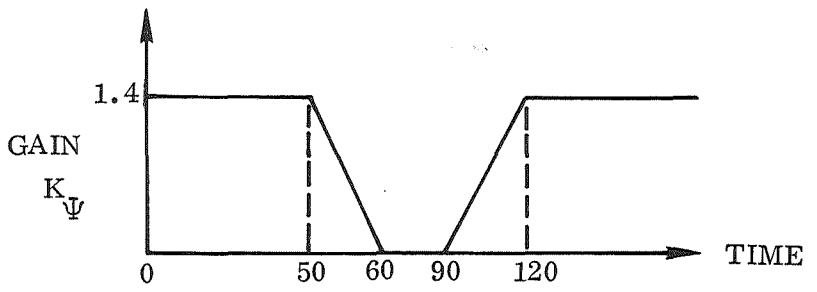

The performance penalty was approximately 5000 pounds of propellant with this system.

Another β reduction (or load alleviation) technique makes use of the absolute value of the roll attitude error. Figure 2-3 presents a block diagram of this scheme. As the absolute value of the roll attitude error increases, the yaw attitude gain is decreased and the side-slip angle gain is increased. When compared to the previous scheme, this reduces performance losses to 4000 pounds of propellant but only reduces β by 29%.

Side loads due to winds are critical for the orbiter and booster vertical tail. Other side load conditions are at least a factor of four below these ascent side loads.

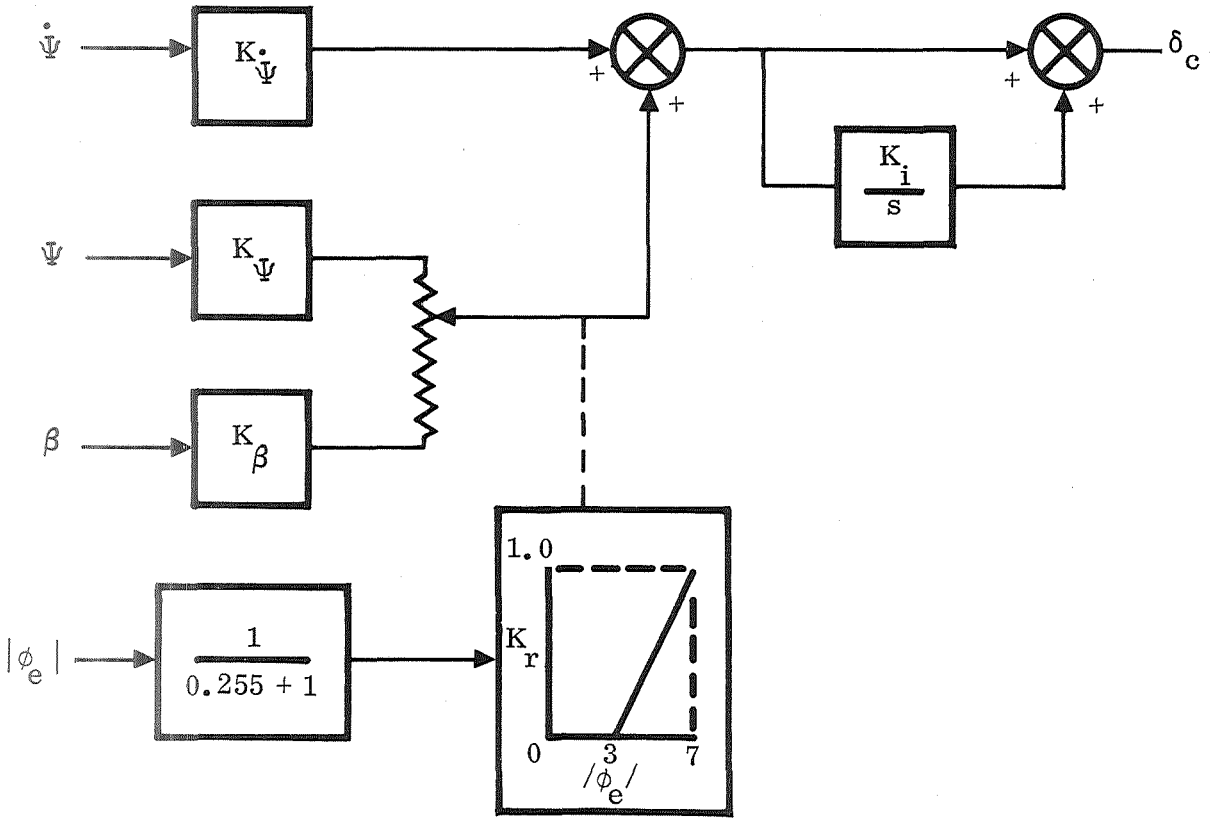

Figure 2-3. Block Diagram of Side Slip Minimization Control

2.6 BOOSTER ENTRY LOADS

Entry loads result from the high entry angle of attack. Entry angles of attack are approximately 60 degrees in order to minimize aero heating. Figure 2-4 presents a baseline booster entry trajectory. The maximum normal load factor obtained is +4g and it occurs at approximately 200 seconds after separating of the two elements. The vehicle is banked approximately 80 degrees in order to minimize turning radius and thereby minimize the cruise range requirements. Bank angle and normal load factor produce the force which turns the vehicle.

Trajectories were flown where the normal load factor was held to a maximum of 3g. The flyback range increased by 60 n.mi. resulting in increase of the flyback fuel by

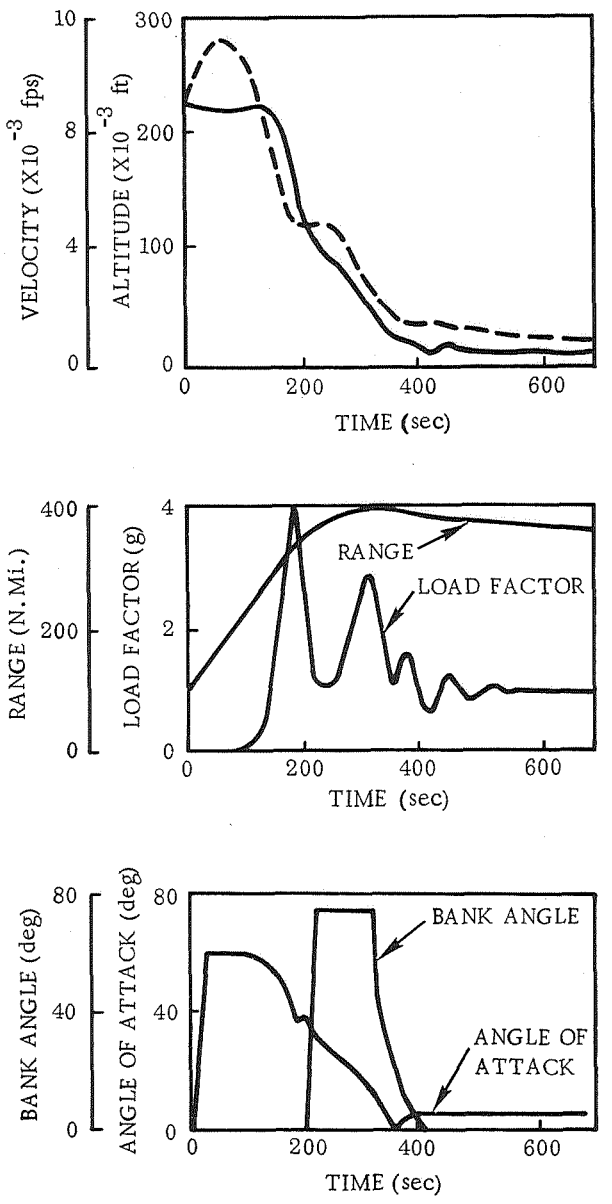

Figure 2-4. Booster Entry Trajectory

5000 pounds. This was for the baseline liquid hydrogen fueled cruise engines. If JP flyback engines are used, the fuel penalty increases more sharply.

2.7 ESTIMATE OF STRUCTURAL WEIGHT SAVINGS FOR RIGID BODY LOAD REDUCTION

The structural weight saving was evaluated for the nominal 25% ascent load reduction potential. This load reduction percentage was chosen because it appears to have the most potential, can be implemented by gain scheduling, gimbal limiting, trajectory biasing or accelerometer feedback, and can be accomplished with approximately 5000 pounds of added propellant.

To estimate the structural weight savings, a detail mathematical model of all major structural components was formulated. This model included booster wing-like elements with integrally stiffened cover skins and orbiter wing-like elements with Z-stiffened cover skins. The booster has an Inconel 718 wing and tail with an aluminum 2219-T87 body; the orbiter has Inconel 625 lower wing and horizontal tail covers with Titanium 6Al-4V upper wing and horizontal tail covers, vertical tail, and body.

A two-spar stiffened skin box construction forms the design of all the wing type surfaces. Where a surface is swept, the loads in the structural box are integrated along a mean structural box chord line. Elevated temperature effects are accounted for by simply lowering the material allowables. All loads were given a uniform pressure distribution. An ultimate load factor of 1.4 is applied to the design limit loads.

Structural box cover and spar weights were estimated by an automated sizing program. The structure is sized simultaneously for various loading conditions that occur during the entire flight profile. Theoretical and non-optimum factors varying between 1.25 and 1.5, depending on the particular substructure are used to derive realistic design

weights from the theoretical weight. These factors account for leading edge covers, trailing edge panels, and manufacturing variation from the theoretical design. Table 2-4 presents structural sizing data for the booster wing.

Table 2-4. Wing Weight Summary

Item	Non-Opt Factor	Weight (lb)
Structural Box		
Compression Cover	1.25	6,443
Tension Cover	1.25	5,552
Webs	1.50	1,541
Ribs	2.00	6,141
Carry Through	1.45	8,546
Leading Edge	1.00	914
Trailing Edge	1.00	2,613
Flap		2,713
Ailerons		357
T.P.S.		0
Tip		90
		34,910
Exposed Wing Weight:		26,400
Contingency (10%)		2,640
		29,000
Total Exposed Wt. Per Side:		14,500

2.7.1 BOOSTER WING. The booster wing is designed by entry loads and ascent headwind and tailwind loads. The entry loads magnitude is not as large as the ascent loads. However, the elevated temperature of the hot wing structure reduces material properties to the point where entry loads are a design condition for parts of the wing.

Reducing the ascent loads by 25% results in a 3.5% structural weight saving. The wing structural weight is approximately 29,000 pounds which means a potential weight savings of 1000 pounds in structural weight.

2.7.2 ORBITER WING. The design conditions for the orbiter wing are entry loads, ascent head/tailwind loads, and material minimum gage (0.03 inch). The orbiter wing is thermally protected; therefore, properties of a room-temperature structure were assumed. Reducing the ascent loads by 25% results in a 4.5% reduction in structure weight. The orbiter wing weighs approximately 13,000 pounds which means a potential weight saving of 585 pounds in structural weight.

2.7.3 BOOSTER AND ORBITER VERTICAL TAILS. Only the ascent sidewind condition produces a design load condition for the orbiter and booster vertical tails. A 25% reduction in side load results in a 12% structural weight savings for both the orbiter and booster vertical tails. The approximate structural weights of the orbiter and booster tails are 4600 pounds and 10,500 pounds, respectively. Therefore, an approximate structure weight savings of 550 pounds for the orbiter and 1260 pounds for the booster can be realized by load reduction techniques.

2.7.4 BOOSTER AND ORBITER HORIZONTAL TAILS. The design conditions for both tails are ascent head/tailwinds, entry, and material minimum gage (0.03 inch). Reduction of the ascent loads by 25% results in approximately 3% structural weight saving for both tails. The orbiter and booster tail weigh 4000 pounds and 14,000 pounds, respectively. Therefore, a structural weight savings of 120 pounds for the orbiter and 520 pounds for the booster can be obtained by load reduction methods.

2.7.5 BOOSTER AND ORBITER FUSELAGES. Figures 2-5 and 2-6 present the load intensities for the orbiter and booster fuselage, respectively. The effect of ascent headwinds had a strong influence in the design of the booster lower surface. Other portions of the booster fuselage were designed based on booster burnout acceleration, ullage pressure, and maximum thrust acceleration. By reducing the ascent loads by 25%, a fuselage structural weight saving of 2000 pounds can be realized for the booster.

The orbiter fuselage was designed based on orbiter burnout acceleration, entry, and a small portion based on ascent tailwinds. Minimum gage is also a constraint on the forward portion of the orbiter fuselage. A 25% ascent load reduction produces a 500-pound structural weight saving in the orbiter fuselage.

2.8 POTENTIAL OF RIGID BODY LOAD REDUCTION

Rigid body load reduction techniques for the space shuttle can potentially reduce ascent loads by 25%. Trajectory biasing, gimbal angle limiting, side-slip angle feedback, and gain scheduling all have equal potential for providing this load reduction. Table 2-5 summarizes the potential of load reduction by listing the structural weight saving for each major structural component.

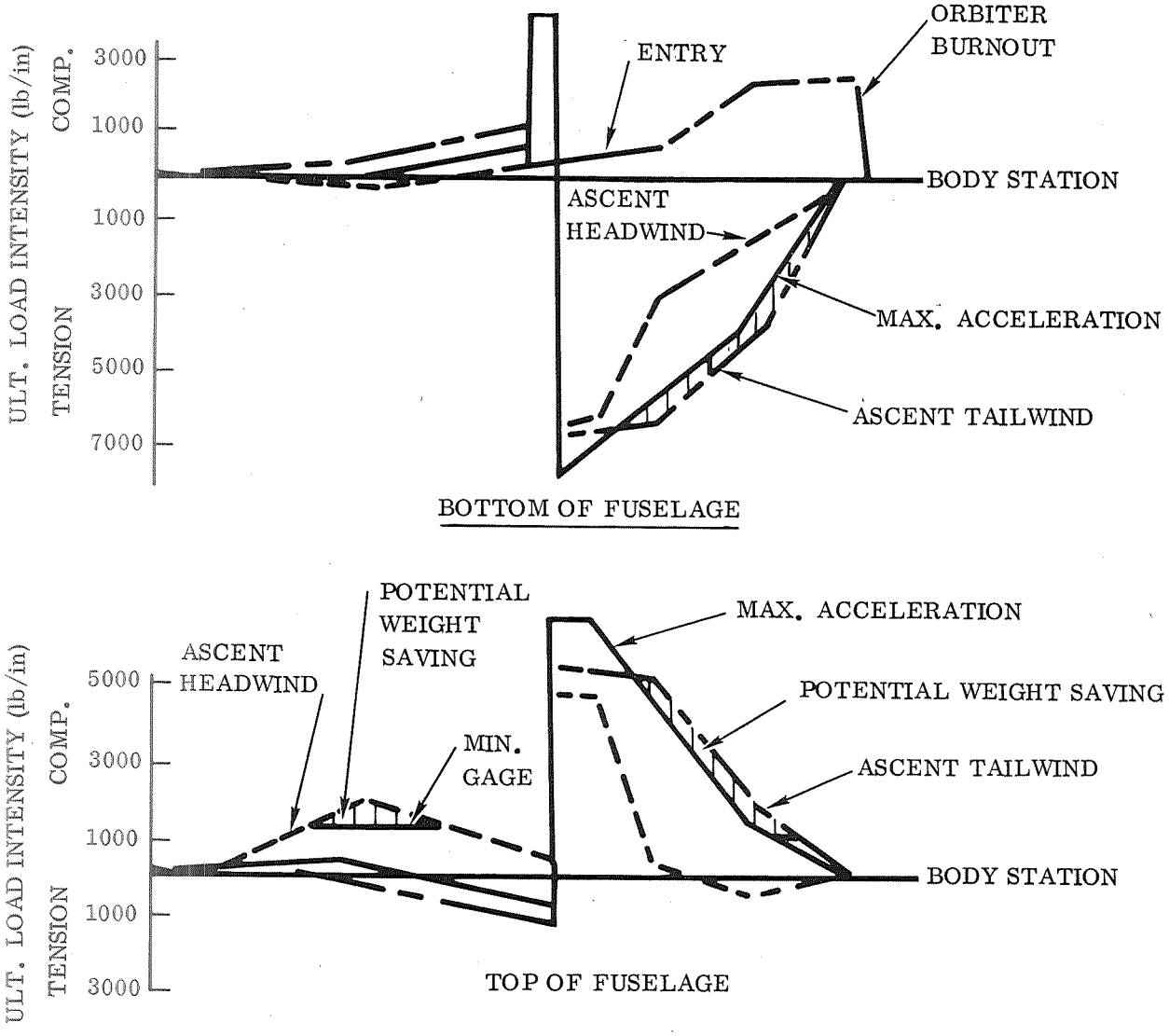

Figure 2-5. Orbiter Fuselage Load Intensities

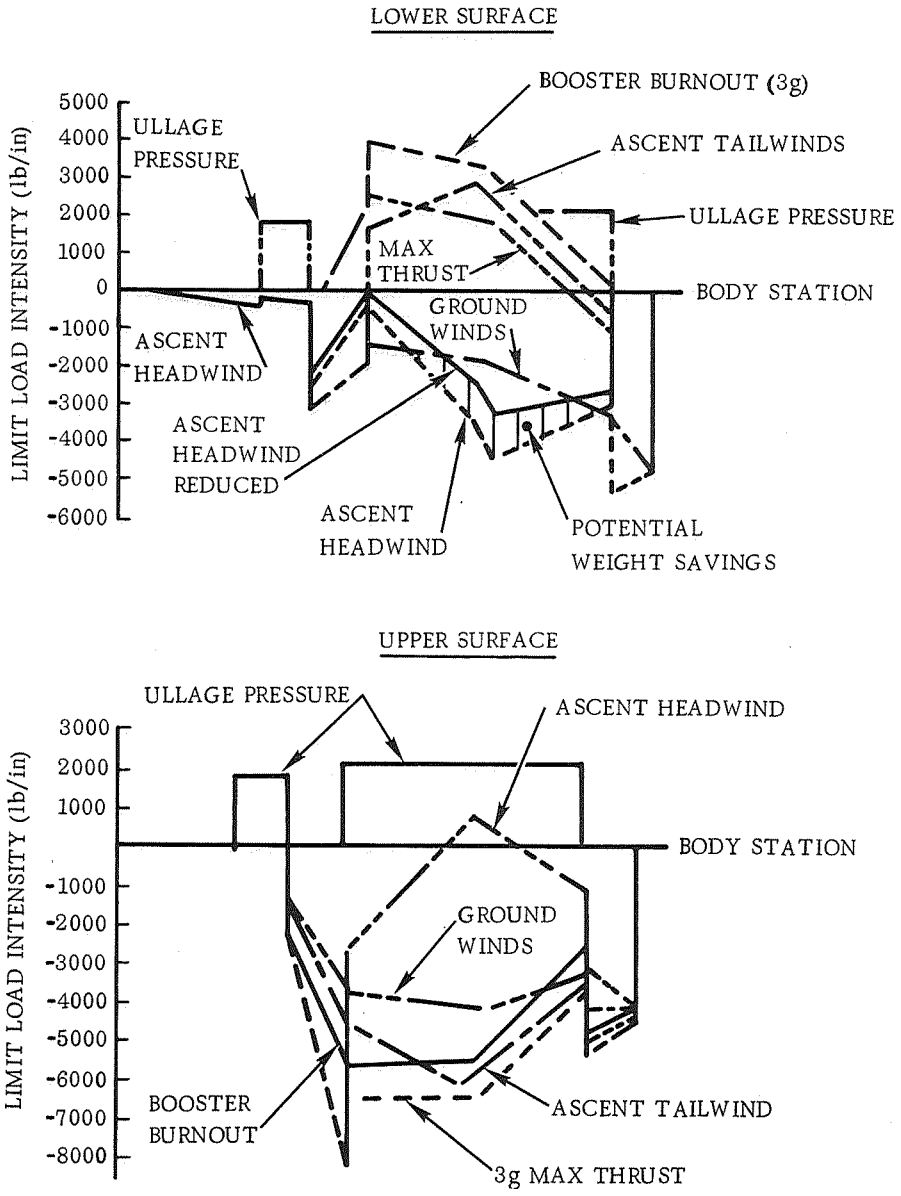

Figure 2-6. Booster Fuselage Design Load Intensities

Table 2-5. Potential of Load Reduction

	Structural Weight Saving (lb)	
	Orbiter	Booster
Wing	585	1,000
Horizontal Tail	120	520
Vertical Tail	550	1,260
Fuselage	500	2,000
Total	1,755	4,780

The booster structural weight saving is approximately balanced by the performance penalties (increased propellant requirements). Therefore, load alleviation can save approximately 1755 pounds of orbiter structural weight. Orbiter structural weight trades for payload on a one-to-one basis. The conclusion is that load alleviation can increase payload from 1500 to 2000 pounds.

SECTION 3

ESTIMATE OF FATIGUE DAMAGE

The general method of analysis used in the calculation of fatigue damage is based on the linear cumulative damage theory as presented by M. A. Miner in Reference 1 This theory states that damage accumulation in a structural element is equal to the summation of the ratio of the number of cycles of applied stress of a given magnitude to the number of cycles to failure at that stress.

$$D = \sum_{i=1}^{M} \frac{\eta_i}{N_i}$$

The cycles to failure curves were derived from fatigue properties for the structural material used. The applied stress spectrum was estimated for each structural location of interest.

Most of the material fatigue data available is in the so-called high cycle range (10^5 to 10^7 cycles). For the space shuttle vehicle the importance to design to withstand relatively few cycles (1 to 1000) of high loading, points out the need to establish material fatigue properties data in the low-cycle area. Reference 2 gives data for Inconel 718 for 10^5 cycles and larger, notched ($K_t = 3.0$), unnotched, and for various temperatures. For values in the low-cyclic range, Reference 3 was used. Figure 3-1 presents typical data from this reference. To account for temperature effects, Figure 3-1 is normalized to a percentage of maximum cyclic stress by the room temperature allowable stress. Then, to obtain the elevated temperature S-N (stress-number of cycles) curve, the normalized S-N curve is multiplied by the material allowable stress at the given elevated temperature.

3.1 LOAD SPECTRA

Orbiter and booster load spectra were generated for four structural points on each vehicle; the wing, horizontal tail, vertical tail roots, and a point on the fuselage slightly forward of the wing leading edge. The mission flight profile was divided into nine ascent segments, entry, cruise, approach/landing, and taxi. These spectra are presented in Figures 3-2 through 3-9.

The ascent spectra were generated by flying a rigid vehicle through ten "real" wind profiles. For each structural point load (bending moment), exceedences were monitored. The frequency content of the winds used was not high enough to excite elastic modes. Therefore, a power spectral approach was used to develop that portion of the load spectra which can be attributed to elastic motion and the higher frequency components of the wind.

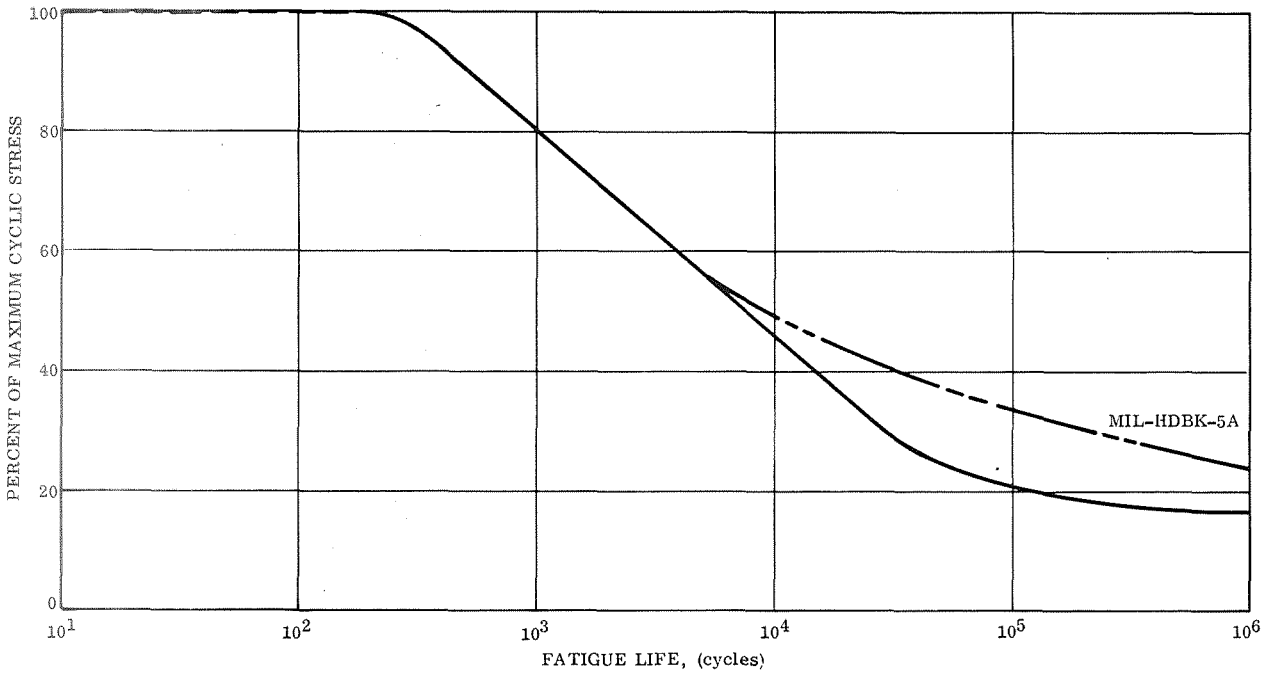

Figure 3-1. Fatigue Diagram for Inconel 718 at Room Temperature as a Percentage of Maximum Cyclic Stress

For these estimates, a computer program was used which develops transfer functions relating control point load to gust input and then computes the control point output spectra by

$$\Phi_{OUT}(\omega) = T^2(\omega)\,\Phi_{IN}(\omega)$$

where:

$\Phi_{OUT}(\omega)$ = control point output spectral

$\Phi_{IN}(\omega)$ = gust input spectral

$T^2(\omega)$ = transfer function relating control point load to gust input.

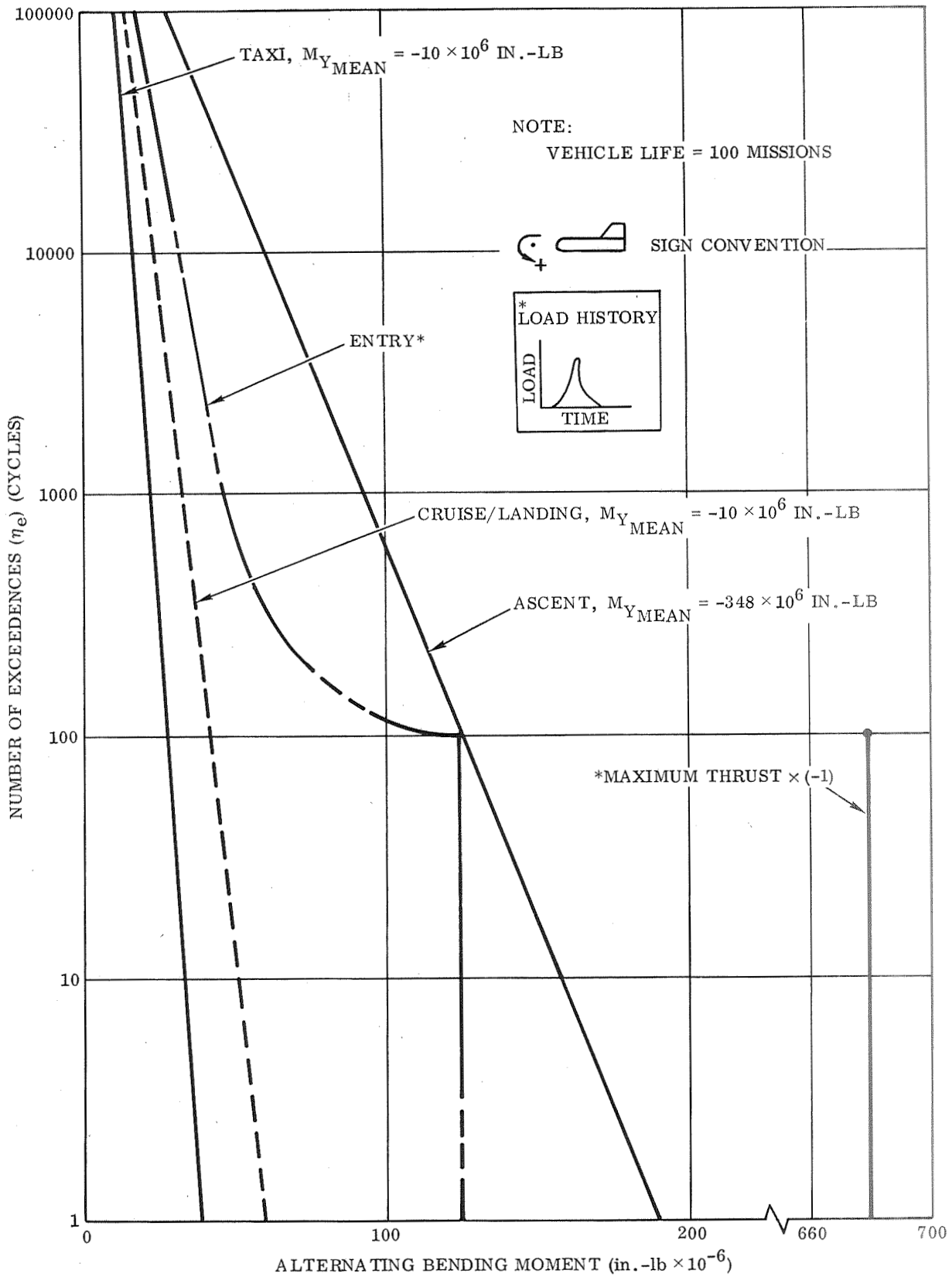

Figure 3-2. Booster Fuselage Station 2600 Load Spectra — Bending Moment, M_y

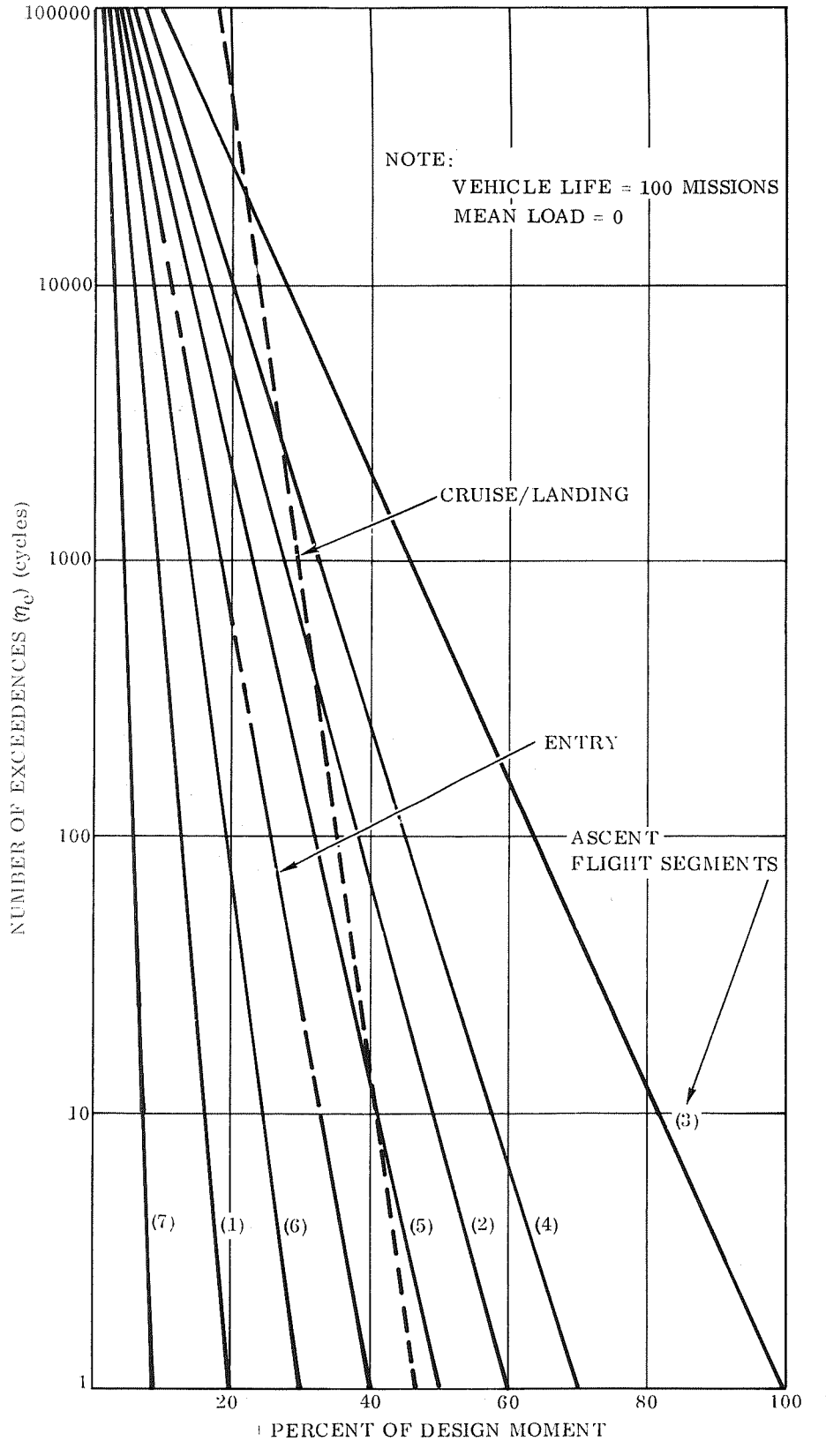

Figure 3-3. Booster Vertical Tail Load Spectra, Percent Design Root Bending Moment

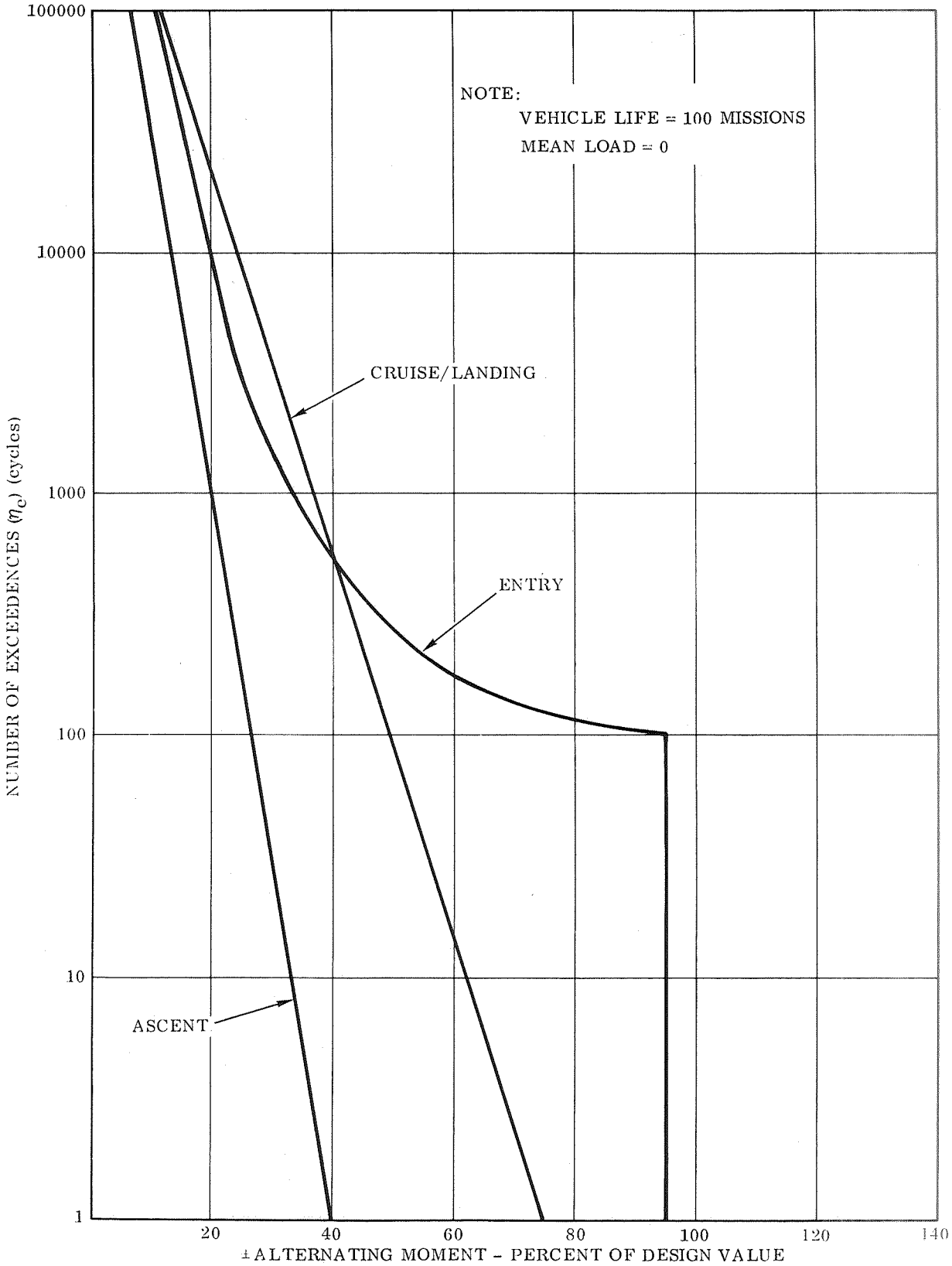

Figure 3-4. Booster Horizontal Tail Load Spectra, Percent Design Root Bending Moment

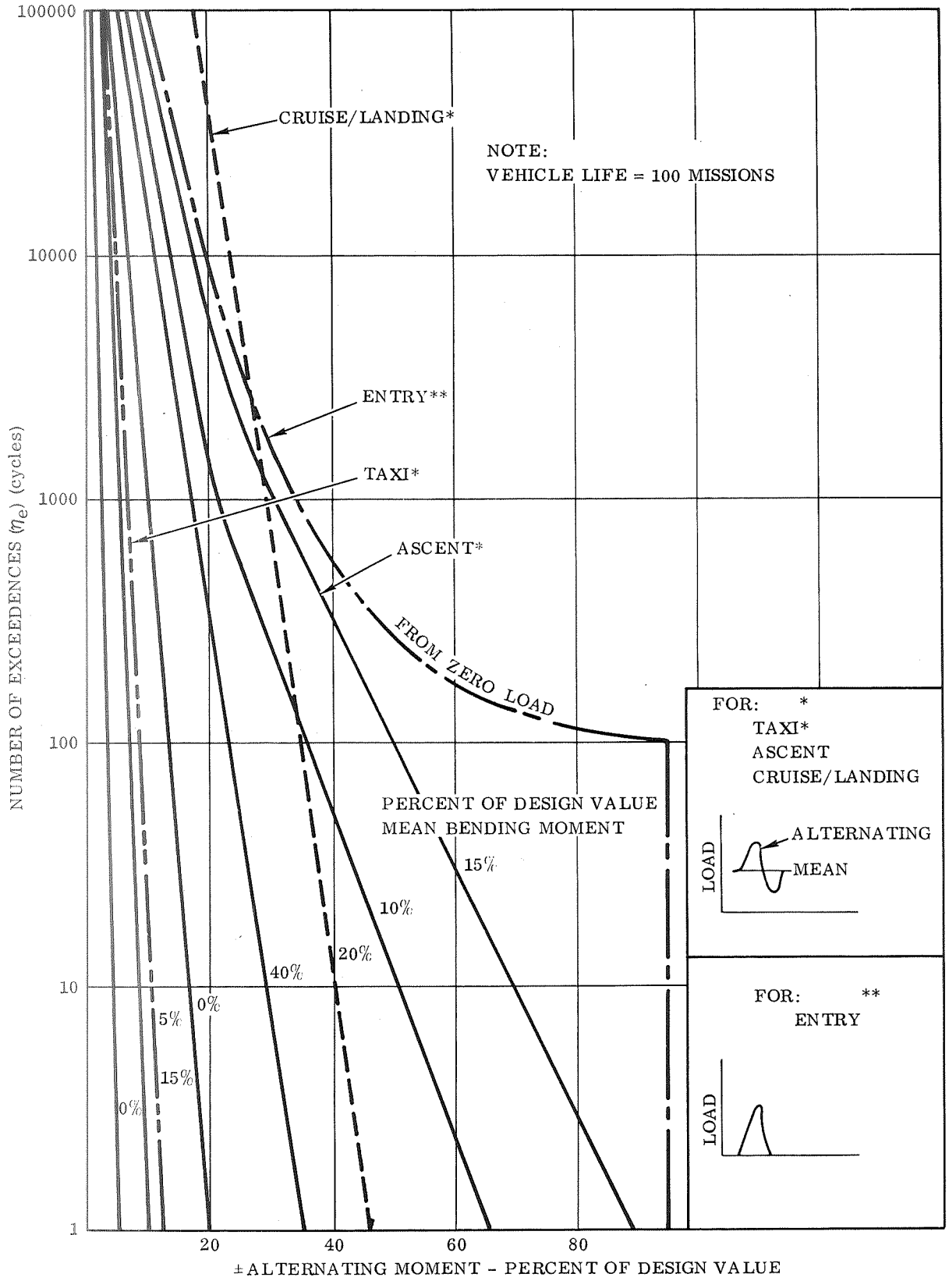

Figure 3-5. Booster Wing Load Spectra, Percent Design Root Bending Moment

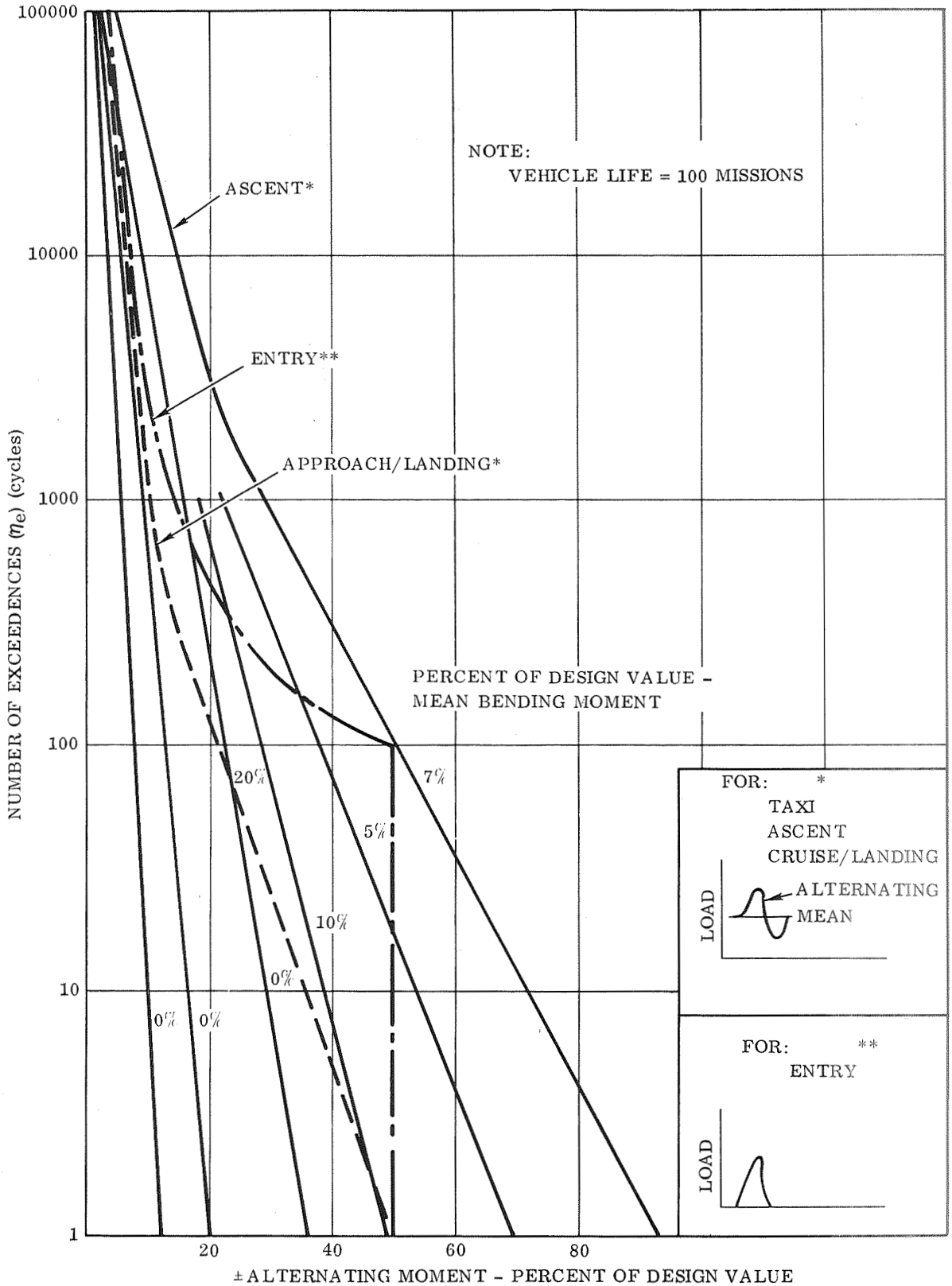

Figure 3-6. Orbiter Wing Load Spectra Percent Design Root Bending Moment

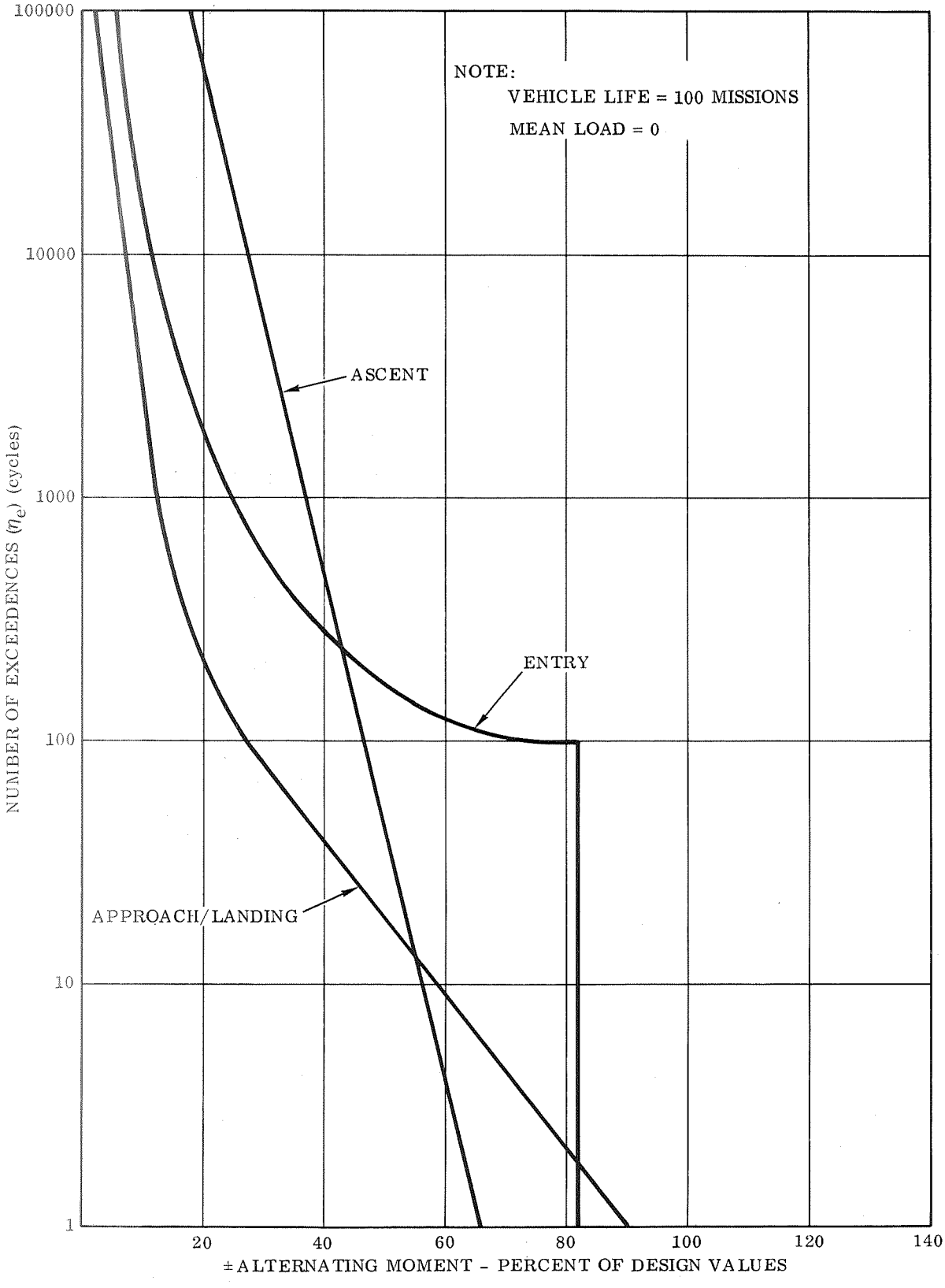

Figure 3-7. Orbiter Horizontal Tail Load Spectra, Percent Design Root Bending Moment

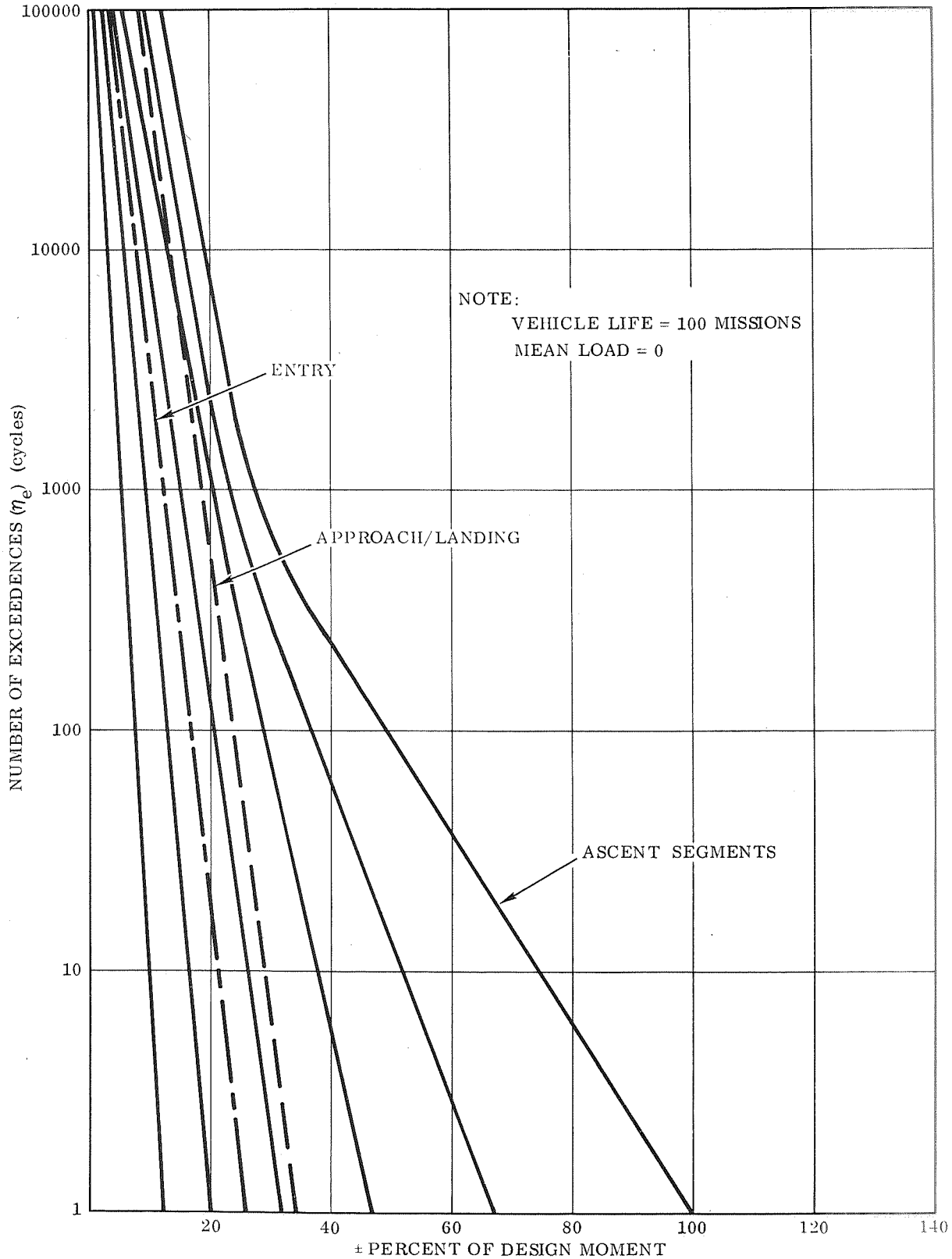

Figure 3-8. Orbiter Vertical Tail Load Spectra, Percent Design Root Bending Moment

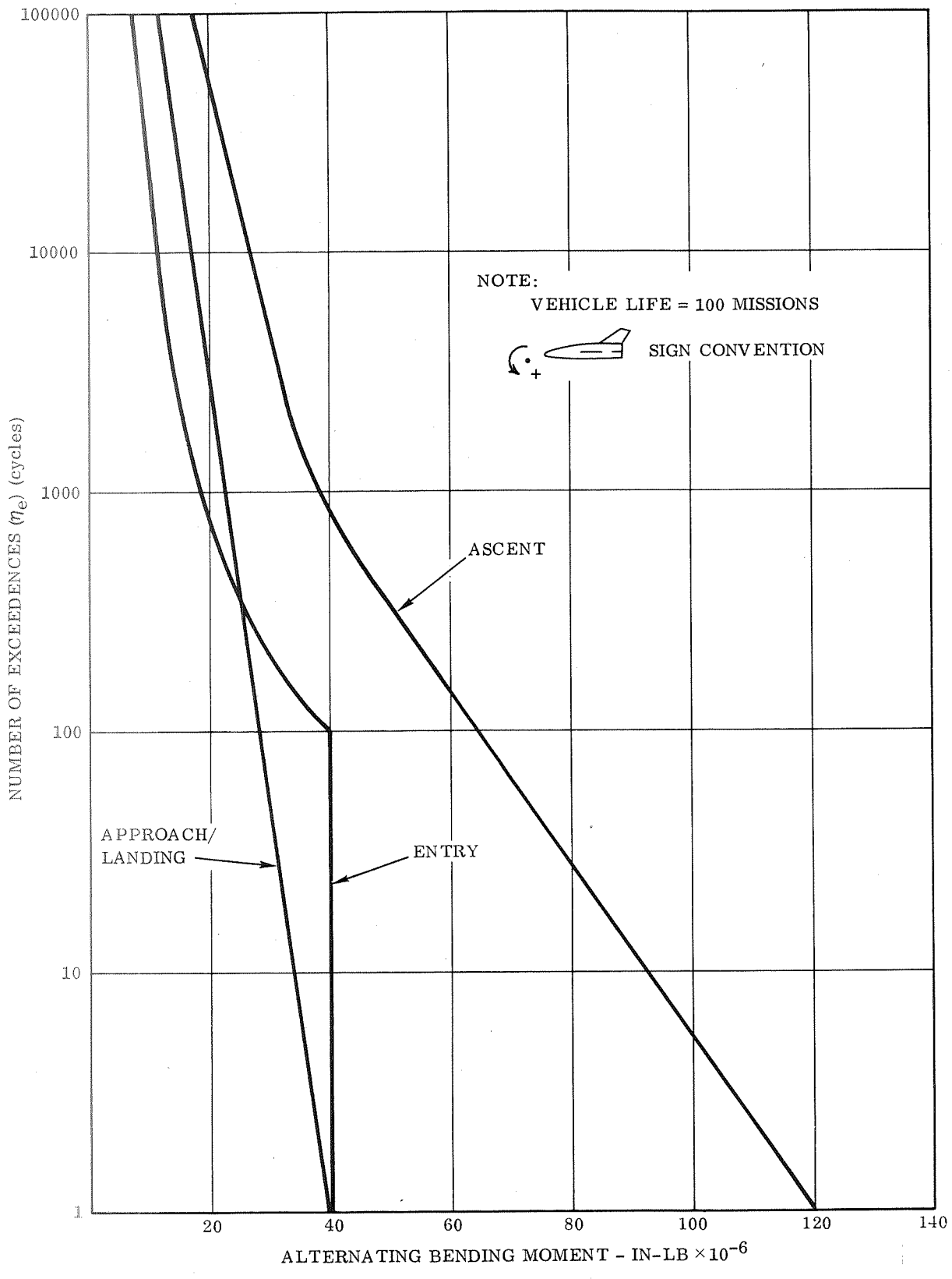

Figure 3-9. Orbiter Fuselage Station 1300 Load Spectra — Bending Moment, M_y

The control point output spectra was used to compute the number of occurrence of various levels of load by

$$N(LL) = N_O \left[P_1 e^{-LL/b_1 \bar{A}} + P_2 e^{-LL/b_2 \bar{A}}\right]$$

Where:

$$N_O = \frac{1}{2\pi}\left[\frac{\left[\int_o^\infty \omega^2 \Phi_{OUT}(\omega)\, d\omega\right]}{\left[\int_o^\infty \Phi_{OUT}(\omega)\, d\omega\right]}\right]^{1/2}$$

$$\bar{A} = \left[\int_o^\infty \Phi_{OUT}(\omega)\, d\omega\right]^{1/2}$$

P_1, P_2 = turbulence scale factor

b_1, b_2 = turbulences magnitude parameters

LL = load level

N(LL) = number of exceedences of load level

The transfer function used in these computations includes the first four elastic modes of each major structural component. For the aerodynamic lifting surfaces (wing, horizontal and vertical tail), aerodynamic forces due to modal motion were included. These aerodynamic forces were computed using Woodward theory and are quasi-steady values.

Results indicate that elastic modes with frequencies greater than 10 Hz contribute less than 1% to the exceedence count. This is due to the fact that the energy content of the gusts is primarily in the lower frequency region (less then 1 Hz).

To obtain the composite load spectra for the ascent portion of flight, the number of exceedences due to gusts was added to the exceedences computed from simulated flights through real winds. The load spectras are based on 100 missions. Since the baseline space shuttle vehicle does not ascend on a zero angle of attack trajectory each ascent flight segment has a mean load about which wind/gust load varies. The gust component of the ascent load spectra only represents approximately 10 percent of the total ascent load spectra. This result is due to the large inertia and low vehicle response at the time of maximum external disturbance.

The entry load spectra were obtained by (1) simulating the vehicle entry flight and measuring the load exceedences and (2) applying gust spectral density methods. The former of these methods provides flight path oscillation loads and rigid body wind loads. The latter provides the elastic body response to the high-frequency gust inputs. This method is identical to the ascent load spectra generation. The load spectra attributable to the gust represents only five percent of the load spectra. This is due to the relatively low magnitude of the input spectra at the high altitudes. The entry portion of flight was defined to be from 400,000 feet to 80,000 feet in altitude.

To determine the load spectra for the booster cruise and the orbiter/booster approach portions of flight, power spectral density methods were used. Throughout this study the Dryden gust spectral density was used.

$$\Phi_{Gust}(\Omega) = \frac{\sigma_w^2 \, L}{\pi} \frac{(1 + 3 L^2 \Omega^2)}{(1 + \Omega^2 L^2)^2}$$

where

$\Phi_{Gust}(\Omega)$ = gust spectral density

σ_w^2 = gust variance squared

L = length scale factor

Ω = reduced frequency $\left(\frac{\omega}{V}\right)$ rad/ft

V = velocity ft/sec

ω = frequency cps

Included in the presented composite load spectra are maneuver load factors. Table 3-1 presents the estimated maneuver-load-factor spectra for the space shuttle orbiter and booster. They are based on Table VII of Reference 4 and have been factored for a 100-mission life.

3.2 FATIGUE DAMAGE

Fatigue damage was computed from the presented load spectra for the four orbiter and four booster control points. Table 3-2 present the accumulative damage factor $\Sigma \eta / N$ for each of the control points. No point is fatigue critical (accumulative damage factor $\Sigma \eta / N < 1.0$). For the booster, the cruise portion of flight contributes the most to the damage. This is due to the relatively long time spent in the cruise mode,

Table 3-1. Maneuver Load Factor Spectra for Space Shuttle Approach and Landing (100 Mission)

N_Z (g)	Occurrence
2.4	1.0
2.2	4.0
2.0	10.0
1.8	35.0
1.6	170.0
1.4	1390.0
1.2	16500.0
0.9	4300.0
0.8	1200.0
0.7	290.0
0.6	50.0
0.4	2.0

Table 3-2. Fatigue Damage at Control Point

$\Sigma\frac{\eta}{N}$	Booster				Orbiter			
	Wing	Horizontal Tail	Vertical Tail	Fuselage	Wing	Horizontal Tail	Vertical Tail	Fuselage
Ascent	0.07	0.05	0.08	0.15	0.12	0.05	0.10	0.12
Entry	0.02	0.05	0.01	0.04	0.05	0.06	0.01	0.04
Cruise/ Landing/ Approach	0.10	0.12	0.10	0.01	0.01	0.01	0.04	0.02
Accumulative	0.19	0.22	0.19	0.20	0.18	0.12	0.15	0.18
Accumulative × 4.0*	0.76	0.88	0.76	0.80	0.72	0.48	0.60	0.72

* Scatter factor = 4.0

one and one-half hours compared to three minutes in ascent and six minutes in entry. For the orbiter, entry and ascent provide about equal amounts of fatigue damage. The short duration orbiter approach does not produce very much fatigue damage.

These results are based on limited fatigue properties data. Especially in the high-stress, low-number-of-cycles region. Design or near-design load will be applied to the booster on every flight. This is analogous to a fighter airplane being subjected to 7 g on every flight. Small variation in the fatigue data in the low-cycle, high-stress region can produce fatigue critical areas.

A classical scatter factor of 4.0 has been used throughout the study. This scatter factor is used to account for variations in fatigue material properties test results. Since fatigue behavior is dependent on minute imperfections in metals, scatter and variations in test results are not surprising. As the data needed for describing materials in detail become available, it may be possible to reduce the scatter factor to 3.0 or even 2.0. Economic consideration may make it impractical to run a large number of fatigue tests on the space shuttle structure. Reference 5 specifies that a scatter factor of 4.0 be used.

SECTION 4

MODAL SUPPRESSION

The dynamic response of flexible airframes continues to be a fundamental problem to aircraft designers and operators. It has become a more important design criterion as mission requirements have subjected airframes to more severe environments, as airframe structural-weight-to-total-weight ratios have decreased, and as knowledge has improved about dynamic response effects on equipment and system effectiveness. It has become more apparent that the dynamic response of aircraft influences riding and flying qualities, safety, equipment and structural failures, and basic airframe operational life.

For years, designers of ballistic missile boosters have stabilized structural modes. The space shuttle vehicle is a more complicated machine, but the structural weight ratios are comparable to those used for missiles. Stability augmentation systems (SAS) for the space shuttle are mandatory to control the vehicle through the many automatic portions of flight and to provide the pilot with good handling qualities during manual modes of operation. These requirements have dictated a highly reliable stability augmentation system. Structural dynamic stabilizers are essentially SAS systems with an extended bandwidth capability. Several studies have been performed on systems that extend the control of the rigid body dynamics into the lower frequency structural dynamic modes. These have shown that it is possible to selectively gain-stabilize by shifting the mode frequencies, to phase-stabilize by increasing the damping, and to avoid or filter out control signals from the several modes. While all these investigations have been analytic, none, not even the most comprehensive, have indicated a fundamental limitation precluding significant success.

While feasibility is no longer seriously contended, and the general benefits of improved structural dynamic response control are universally acceptable, there is no data available which indicates specific performance potential for a given situation and vehicle. This study specifically analyzed the straight wing, low crossrange space shuttle vehicle to assess the potential increase in structural modal damping by active control. Increased structural damping provides the obvious benefits of improved airframe response, reduced structural dynamic loads, and increased structural life. Even though the discussions in Section 3 indicate that fatigue damage is not critical to structural design, there are numerous assumptions in the preliminary fatigue analysis which, with small changes, can lead to fatigue critical areas.

Modal suppression implies, essentially, the control of structural modes only and is akin to the problem of flutter suppression. Associated problems can be classified within a few categories as follows:

a. The determination of the contribution of the different structural modes to a given arbitrary deformation of the aircraft.

b. The determination of a control law which will actuate the control surfaces in a certain fashion, proportional to the participation of the structural mode in the given deformation, and give rise to a stable control system. An unstable control system can arise, for example, when a signal sensed from one structural mode gives rise to a control force which actuates a second structural mode and which in turn gives rise to a force which drives the first structural mode. This condition is known as control system induced instability and is caused by the sensor-force couplings.

c. The determination that the control forces arising from the determined control law are of the type used to stabilize the motion sensed.

d. The determination that the stabilized system is insensitive to changes in flight configuration, altitude, Mach number, and mode shapes.

Different approaches and methods have been studied for the solution of the problems mentioned in a., b., and c. above. These methods include multisensor systems for modal observation, force-sensor modal decoupling networks, or mode discriminating sensors to avoid control system induced instability, and aerodynamic damping forces for mode stabilization. Linear optimal control theory has recently been used (Reference 6) to provide a systematic way of treating the problem of control system instability and to increase the control-force stabilization effectiveness. However, the control law which is derived by this method, and which depends on the location of the sensors, cannot often be attained by real systems. Furthermore, it may require as many control surfaces as modes considered. Recently, Wykes (Reference 7) suggested the identically located accelerometer and force (ILAF) scheme to ensure control system stability and made use of control "aerodynamic damping" forces (that is, control deflection proportional to linear velocity) for modal stabilization.

Considerable literature dealing with multiple sensors, rate gyro blending, and tracking notch filters has offered possible solutions to the problem of sensing individual modal acceleration or velocities (References 8 through 11).

For this study it was decided that the control system should be designed to produce damping in the structural modes. To implement this, two control system concepts were considered: One approach involved simultaneous elimination of sensor and force coupling; the other approach involved making positive use of both sensor and force coupling. The first approach can be implemented by introducing proper force magnitudes at the proper locations by multiple control surfaces to cancel the undesirable coupling effects. Such a "mode isolation damper" is complicated because of the number of multiple loops. In many instances, the multiple feedback gains required for cancellation are so large that fail-safety aspects of the design may be endangered. In addition, variations with flight conditions require complicated control system features for

tracking the structural mode frequencies, shapes, damping ratios, and for tracking the unsteady aerodynamic effects of the control surfaces. The space shuttle vehicle does not have many control surfaces along the trailing edge of the wing.

A promising solution has been found in a relatively simple conventional control system, making use of modal coupling that can increase the structural mode damping ratios despite the variation of the mode shapes with flight condition. Such a conventional control system is based upon the concept of introducing a generalized dissipative force at approximately the same location where the sensors measure structural mode velocity.

While it was mandatory to consider the combined excitation of the rigid body as well as structural modes, the control of the structural modes was considered to be by far the more difficult problem. It was felt that rigid body mode control could be exercised using conventional techniques, whereas the structural mode control would require new approaches. Most effort, therefore, was expended on the latter problem area. Specifically, the study effort was directed toward active control of the first five wing asymmetric modes and the first six fuselage modes. The wing modes, orbiter or booster, are basically constant throughout the mission because they contain no internal fuel. The fuselage modes of the booster are the lowest during launch and pose the most severe problem. During entry, cruise, and landing, the fuselage modes are 5.0 Hz or higher, compared to 1.75 Hz or lower for the ascent portion of flight.

Modes higher than the fifth or sixth are not directly controlled. However, they are gain-stabilized by proper electronic networks.

4.1 FUSELAGE MODAL SUPPRESSION

An important consideration in analyzing the overall stability of a launch vehicle is the elastic modes of vibration. For the space shuttle vehicle, the automatic control and stabilization sensors are located on the fuselage of the booster during ascent flight. Therefore, fuselage elastic modes and rigid body response are coupled by sensors and control force. Figure 4-1 presents a block diagram of the pitch plane elastic/rigid body control system coupling. Table 4-1 presents the symmetrical modal frequencies associated with the launch configuration. Figure 4-2 presents the mode shapes for an early portion of ascent flight (0 to 50 seconds). These modes were computed using the structural dynamic computer program NASTRAN. A detailed structural and mass model was established for each of the major structural elements. Table 4-2 presents the equations for the system shown in Figure 4-1. These equations represent small perturbations about the vehicle forward velocity, plunging velocity, pitch attitude, thrust vector motion (tail-wags-dog), thrust vector system lag, six elastic degrees-of-freedom, and the various gains and filters for maximum dynamic pressure portion of flight.

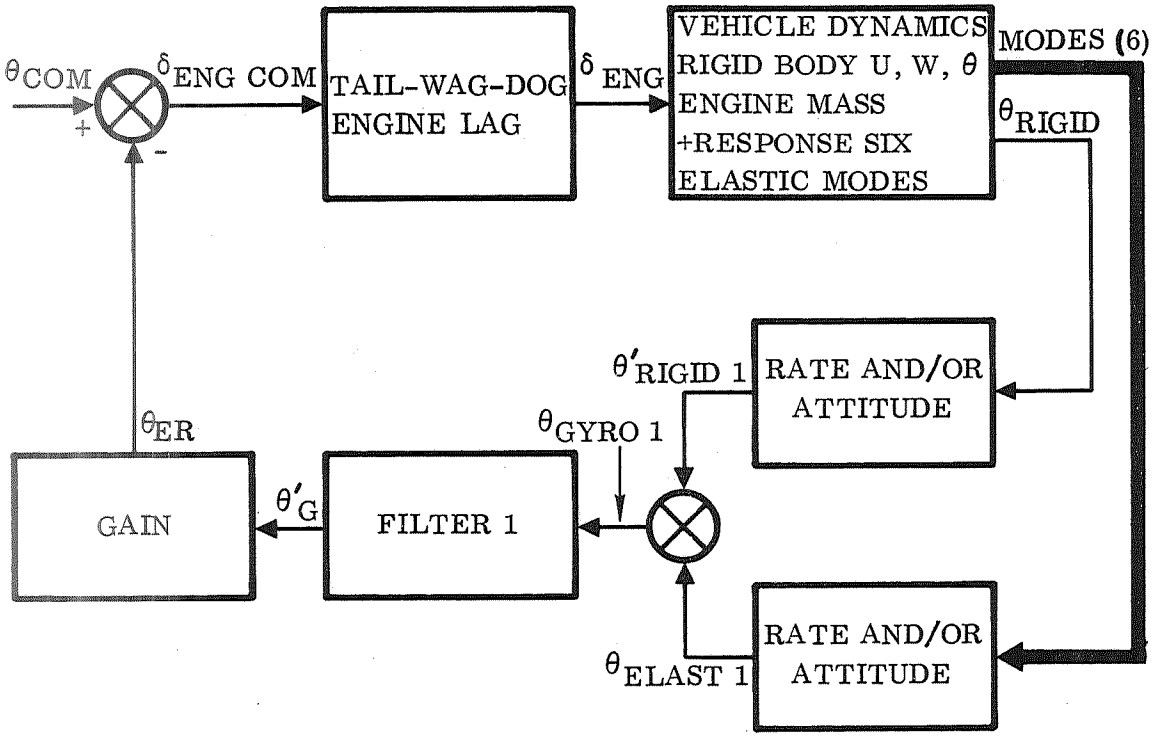

Figure 4-1. Block Diagram of Ascent Pitch Plane Single — Sensor System

Table 4-1. Fuselage Ascent Pitch Plane Mode Frequencies

Mode	Frequency	
	Hz	Rad/sec
1	1.83	11.49
2	1.98	12.44
3	2.20	13.85
4	4.11	25.83
5	4.97	31.21
6	10.40	65.33

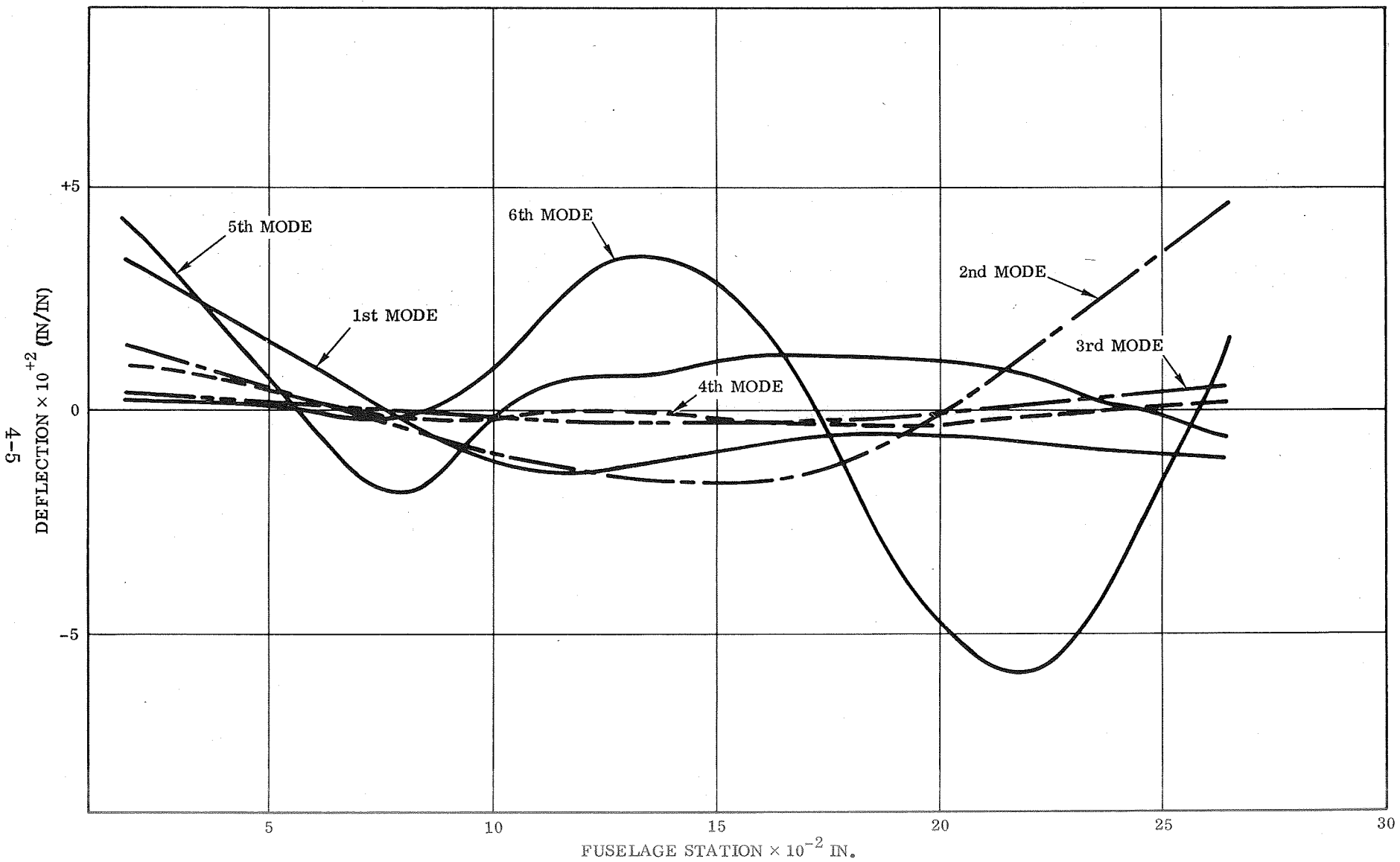

Figure 4-2. Fuselage Modes Shapes

Table 4-2. Ascent Maximum Dynamic Pressure Rigid/Elastic Body Equation

Equation Number And Title	Equation
Forward Velocity (1)	$(0.0265 + S)\ U + (-0.013)\ w + (14.55 - 60\ S)\ \theta + 4.94\ \delta_{eng} = 0$
Normal Velocity (2)	$(0.0287)\ U + (0.16 + S)\ w + (28.69 - 1052\ S)\ \theta + 62.01\ \delta_{eng} = 0$
Pitch (3)	$(0.0001)\ U + (0.0024)\ w + (0.104\ S + S^2)\ \theta + 2.73\ \delta_{eng} = 0$
Tail-Wags-Dog (4) + Engine	$(1 + 0.0012\ S^2)\ \delta_{eng\ com} + (-1 - 0.067\ S)\ \delta_{eng} = 0$
1st Bend (5)	$(132.09 + 0.23\ S + S^2)\ \zeta_1 + (0.011)\ \delta_{eng} = 0$
2nd Bend (6)	$(154.76 + 0.25\ S + S^2)\ \zeta_2 + (-0.046)\ \delta_{eng} = 0$
3rd Bend (7)	$(191.90 + 0.28\ S + S^2)\ \zeta_3 + (-0.005)\ \delta_{eng} = 0$
4th Bend (8)	$(667.05 + 0.52\ S + S^2)\ \zeta_4 + (-0.0018)\ \delta_{eng} = 0$
5th Bend (9)	$(974.10 + 0.62\ S + S^2)\ \zeta_5 + (0.0047)\ \delta_{eng} = 0$
6th Bend (10)	$(4267.7 + 1.30\ S + S^2)\ \zeta_6 + (-0.016)\ \delta_{eng} = 0$
Rigid Body Filter 1 (11)	$\theta'_{Rigid\ 1} + (-K_1 - K_2\ S)\ \theta_{Rigid} = 0$
Rigid Body Filter 2 (12)	$\theta'_{Rigid\ 2} + (-K_3 - K_4\ S)\ \theta_{Rigid} = 0$
Elastic θ 1 Location 480 FS (13)	$\theta_{Elast\ 1} + (-K_1 - K_2\ S)\ 5.1 \times 10^{-5}\ \zeta_1 + (-K_1 - K_2\ S)\ 2.9 \times 10^{-5}\ \zeta_2 + (-K_1 - K_2\ S)\ 0.62 \times 10^{-5}\ \zeta_3 + (-K_1 - K_2\ S)\ 1.15 \times 10^{-5}\ \zeta_4 + (-K_1 - K_2\ S)\ 7.5 \times 10^{-5}\ \zeta_5 + (-K_1 - K_2\ S)\ 0.3 \times 10^{-5}\ \zeta_6 = 0$
Elastic θ 2 Location 1320 FS (14)	$\theta_{Elast\ 2} + (-K_3 - K_4\ S)(-0.34 \times 10^{-5}\ \zeta_1 + (-K_3 - K_4\ S)\ 0.36 \times 10^{-5}\ \zeta_2 + (-K_3 - K_4\ S)\ 0.06 \times 10^{-5}\ \zeta_3 + (-K_3 - K_4\ S)\ 0.1 \times 10^{-5}\ \zeta_4 + (-K_3 - K_4\ S)(-0.1) \times 10^{-5}\ \zeta_5 + (-K_3 - K_4\ S)\ 0.01 \times 10^{-5}\ \zeta_6 = 0$
Gyro 1 Filter (15)	$(K_5\ S^2 + K_6\ S + K_7)\ \theta'_{G\ 1} + (-K_8\ S^2 - K_9\ S - K_{10})\ \theta_{Gyro\ 1} = 0$
Gyro 1 Output (16)	$\theta_{Gyro\ 1} - \theta'_{Rigid\ 1} - \theta_{Elast\ 1} = 0$
Gyro 2 Filter (17)	$(K_{11}\ S^2 + K_{12}\ S + K_{13})\ \theta'_{G\ 2} + (-K_{14}\ S^2 - K_{15}\ S - K_{16})\ \theta_{Gyro\ 2} = 0$
Gyro 2 Output (18)	$\theta_{Gyro\ 2} - \theta'_{Rigid\ 2} - \theta_{Elast\ 2} = 0$
Gyro 1 + Gyro 2 (19)	$\theta'_G - \theta'_{G\ 1} - \theta'_{G\ 2} = 0$
Augmentation (20)	$S\ \theta_{ER} + (-K_{Rate}\ S^2 - K_{ATT}\ S - K_1)\ \theta'_G = 0$
Engine Comm (21)	$\delta_{Eng\ Com} + \theta_{ER} = \theta_{Com}$

Equation Variables

1. U — Forward Velocity
2. w — Normal Velocity
3. θ — Pitch Attitude
4. δ_{Eng} — Engine Deflection
5. $\delta_{Eng\ Com}$ — Engine Command
6. ζ_1 — 1st Mode Coordinate
7. ζ_2 — 2nd Mode Coordinate
8. ζ_3 — 3rd Mode Coordinate
9. ζ_4 — 4th Mode Coordinate
10. ζ_5 — 5th Mode Coordinate
11. ζ_6 — 6th Mode Coordinate
12. $\theta'_{Rigid\ 1}$ — Rigid Pitch Attitude No. 1
13. $\theta'_{Rigid\ 2}$ — Rigid Pitch Attitude No. 2
14. $\theta_{Elast\ 1}$ — Elastic Pitch Attitude No. 1
15. $\theta_{Elast\ 2}$ — Elastic Pitch Attitude No. 2
16. $\theta'_{G\ 1}$ — Gyro Filter No. 1 Output
17. $\theta_{Gyro\ 1}$ — Gyro No. 1 Output
18. $\theta'_{G\ 2}$ — Gyro Filter No. 2 Output
19. $\theta_{Gyro\ 2}$ — Gyro No. 2 Output
20. θ'_G — Gyro 1 + 2 Output
21. θ_{ER} — Pitch Attitude Error
22. θ_{Com} — Pitch Command

A basic rigid body analysis had shown the pitch augmentation for ascent to be:

$$\left(\frac{0.1}{s} + 1.2 + 2.0\,s\right)\theta$$

this provides rigid body characteristics at high dynamic pressure of

$$\omega_{Ph} = 0.07 \text{ rad/sec}$$

$$\omega_{SP} = 7.94 \text{ rad/sec}$$

$$\zeta_{Ph} = 0.6$$

$$\zeta_{SP} = 0.7$$

Table 4-3 presents the rigid body characteristics for various points along the ascent trajectory. Combining these rigid and elastic body characteristics without filtering and with the sensors located near the nose of the vehicle (F.S. 1460) produces an unstable condition. Closed loop characteristics at maximum dynamic pressure are

Frequency (rad/sec)	Damping	
0.07	0.59	Rigid Mode
10.87	-0.04	Elastic Mode
12.26	0.21	
13.86	0.01	
25.82	0.01	
31.09	0.01	
65.56	0.01	

Figure 4-3 presents a locus of roots for various combinations of pitch integration, rate, and attitude gains. The system is relatively insensitive to pitch integration gain. The obvious conclusion is that no combination of gains will produce a stable system. Second order filters of the form

$$\frac{O_{UT}(s)}{I_N(s)} = \frac{K_1(K_2 S^2 + K_3 S + K_4)}{(S^2 + K_5 S + K_6)}$$

were applied to both the rate and attitude gyro signal. The K parameters were varied

Table 4-3. Ascent Pitch Plane Rigid Body Characteristics

Mach No.	Altitude (ft)	Open Loop Characteristics		Closed Loop Characteristics	
		Frequency (rad/sec)	Damping Ratio	Frequency (rad/sec)	Damping Ratio
0.2	2,650	0.311	0.325	7.713	0.848
0.6	11,000	0.73	0.173	7.890	0.827
1.6	50,000	1.404	0.044	8.061	0.787
2.5	86,000	0.596	0.035	8.540	0.757
3.5	110,000	0.40	0.023	8.556	0.757
4.8	143,000	0.217	0.017	8.932	0.721
6.5	180,000	0.107	0.013	8.934	0.721
10.0	230,000	0.04	0.007	9.713	0.652

to produce filters of pure first order lag, lead-lag, second order, and notch types. None of these produced satisfactory mode stabilization let alone increased modal damping.

Past studies have indicated that the location of sensors pitch rate and attitude in both the nose and tail can improve modal stability. With sensors located on the thrust structure, a stable system as shown in Figure 4-4 was developed. Root locus for this system is shown in Figure 4-5. With the two-sensor feedback system, a first order lag at 30 radians was necessary to stabilize the sixth mode. Modal damping increased by a factor of two over the basic structural damping.

Improvement in modal damping beyond the improvement and stabilization discussed in preceding paragraphs would involve the addition of other controllers. These additional controllers would have to provide generalized forces in the same range of magnitude as that supplied by the thrust vector control. Examining the mode shapes indicates that forces produced at the nose and tail provide large generalized forces in all modes. Therefore, aerodynamic forces produced by a canard located on the nose may provide good modal suppression. A root locus at maximum dynamic pressure of a system with canard, thrust vector control (TVC), and sensors located in the nose and tail is presented in Figure 4-6. With this system, the structural modal damping is increased by a factor of 10. However, for the baseline configuration, no such control surface exists

Filter: Out/In = 1

KA	KR	Short Period Mode		Phugoid Mode*		Elastic Modes											
						1		2		3*		4*		5*		6*	
		ω	ζ	ω	ζ	ω	ζ	ω	ζ	ω	ζ	ω	ζ	ω	ζ	ω	ζ
1.2	0	2.40	-0.01	0.07	0.63	11.57	0.005	12.28	0.02	13.85	0.01	25.83	0.01	31.21	0.01	65.33	0.01
	0.1	2.40	0.05	0.07	0.63	12.00	0.001	11.76	0.02	13.85	0.01	25.83	0.01	31.21	0.01	65.33	0.01
	0.5	2.52	0.29	0.07	0.62	12.09	-0.07	11.38	0.05	13.84	0.01	25.83	0.01	31.18	0.01	65.39	0.01
	1.0	2.63	0.61	0.07	0.61	12.11	-0.12	11.10	0.05	13.83	0.01	25.82	0.01	31.15	0.01	65.44	0.01
0.75	0	2.13	0.01	0.08	0.54	11.54	0.01	12.34	0.02	13.85	0.01	25.83	0.01	31.21	0.01	65.33	0.01
	0.1	2.15	0.07	0.08	0.54	12.15	-0.001	11.64	0.02	13.85	0.01	25.83	0.01	31.20	0.01	65.34	0.01
	0.5	2.24	0.34	0.08	0.53	12.15	-0.07	11.37	0.05	13.84	0.01	25.82	0.01	31.18	0.01	65.39	0.01
	1.0	2.34	0.70	0.08	0.51	12.15	-0.12	11.10	0.05	13.83	0.01	25.82	0.01	31.15	0.01	65.44	0.01
	2.0	Real	-	0.08	0.49	12.30	-0.21	10.88	0.04	13.82	0.01	25.82	0.01	31.10	0.01	65.56	0.01
0.5	0	1.96	0.02	0.09	0.48	11.53	0.01	12.37	0.02	13.85	0.01	25.83	0.01	31.21	0.01	65.33	0.01
	0.1	1.98	0.09	0.09	0.48	12.21	-0.001	11.60	0.02	13.85	0.01	25.83	0.01	31.20	0.01	65.33	0.01
	0.5	2.06	0.38	0.09	0.46	12.17	-0.070	11.36	0.05	13.84	0.01	25.82	0.01	31.18	0.01	65.39	0.01
	1.0	2.16	0.77	0.09	0.45	12.18	-0.12	11.11	0.05	13.83	0.01	25.82	0.01	31.15	0.01	65.44	0.01
	2.0	Real	-	0.09	0.41	12.32	-0.21	10.88	0.04	13.82	0.01	25.82	0.01	31.10	0.01	65.56	0.01
0.1	0	1.67	0.05	0.10	0.37	11.51	0.01	12.43	0.01	13.85	0.01	25.83	0.01	31.21	0.01	65.33	0.01
	0.1	1.68	0.13	0.10	0.36	12.29	-0.01	11.55	0.02	13.85	0.01	25.83	0.01	31.20	0.01	65.34	0.01
	0.5	1.76	0.47	0.10	0.34	12.22	-0.07	11.35	0.05	13.84	0.01	25.82	0.01	31.18	0.01	65.39	0.01
	1.0	1.85	0.92	0.10	0.31	12.22	-0.12	11.11	0.05	13.83	0.01	25.82	0.01	31.15	0.01	65.44	0.01
	2.0	Real	-	0.10	0.27	12.35	-0.21	10.89	0.04	13.82	0.01	25.82	0.01	31.10	0.01	65.56	0.01

* Damping and frequency of these modes are unchanged regardless of filter.

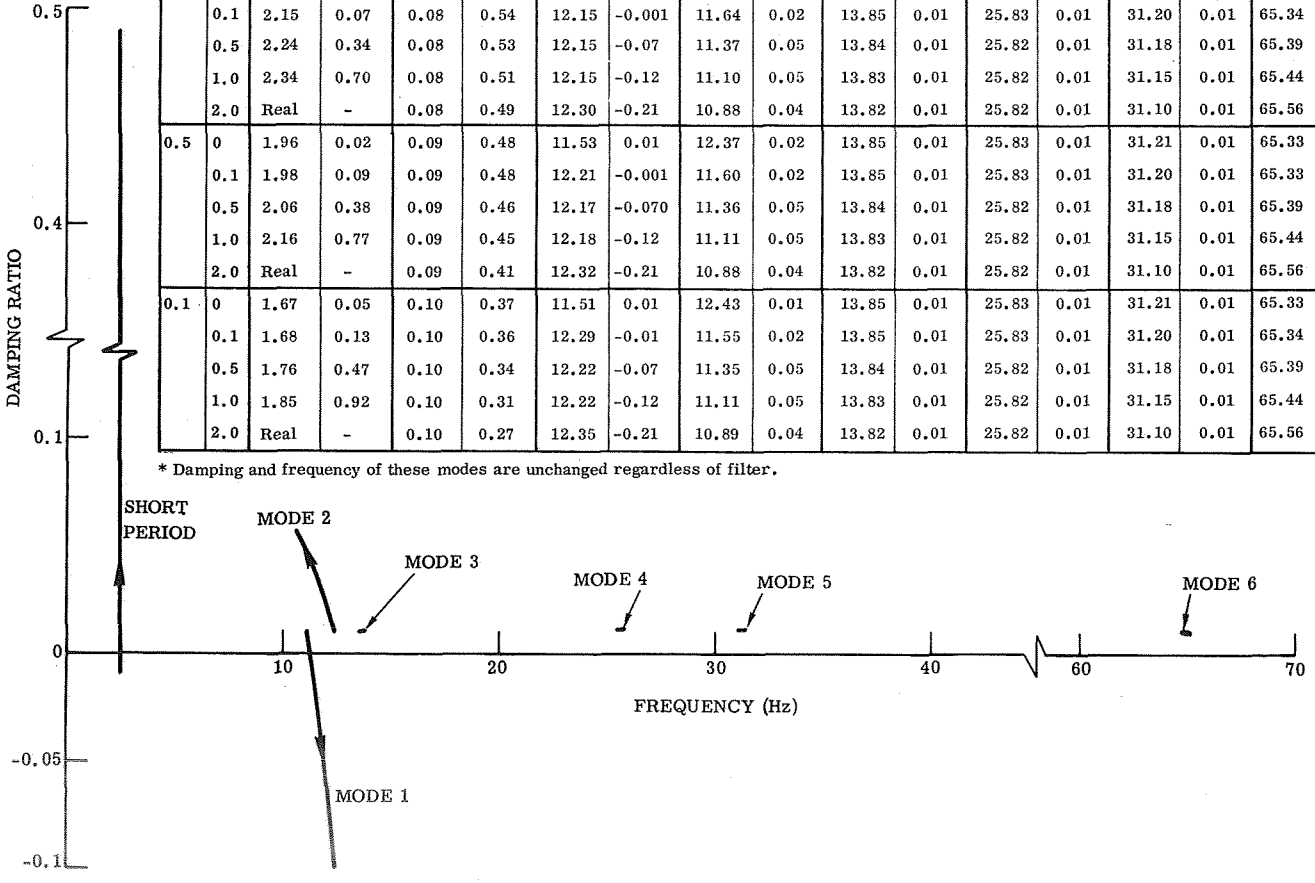

Figure 4-3. Single-Sensor Ascent Pitch Control System (Sheet 1 of 3)

VARIOUS FILTERS USED IN SINGLE-SENSOR ASCENT PITCH CONTROL SYSTEM

Filter: $\frac{300}{S^2 + 35S + 300}$

KA	KR	Short Period Mode ω	Short Period Mode ζ	Elastic Modes 1 ω	Elastic Modes 1 ζ	Elastic Modes 2 ω	Elastic Modes 2 ζ
1.2	0	2.33	-0.08	11.46	0.001	12.51	0.02
	0.1	2.38	-0.03	11.52	0.001	12.38	0.03
	0.5	2.68	0.18	11.57	-0.03	12.05	0.07
	1.0	3.69	0.52	11.39	-0.05	11.80	0.12
0.75	0	2.08	-0.04	11.48	0.01	12.48	0.02
	0.1	2.14	0.02	11.54	0.001	12.35	0.02
	0.5	2.43	0.28	11.59	-0.03	12.00	0.07
	1.0	3.93	0.70	11.41	-0.05	11.75	0.12
	2.0	Real	-	10.90	-0.07	10.94	0.34
0.5	0	1.93	-0.02	11.48	0.01	12.47	0.01
	0.1	1.98	0.05	11.55	0.001	12.33	0.02
	0.5	2.27	0.34	11.61	-0.03	11.98	0.07
	1.0	4.53	0.76	11.42	-0.05	11.73	0.11
	2.0	Real	-	10.90	-0.08	10.86	0.31
0.1	0	1.65	0.04	11.49	0.01	12.45	0.01
	0.1	1.70	0.12	11.57	0.01	12.30	0.01
	0.5	1.97	0.49	11.64	-0.03	11.93	0.07
	1.0	5.34	0.75	11.43	-0.05	11.69	0.11
	2.0	Real	-	10.91	-0.08	10.74	0.32

Filter: $\frac{300}{S^2 + 15S + 50}$

KA	KR	Short Period Mode ω	Short Period Mode ζ	Elastic Modes 1 ω	Elastic Modes 1 ζ	Elastic Modes 2 ω	Elastic Modes 2 ζ
1.2	0	3.49	-0.39	11.37	0.01	12.69	0.02
	0.1	3.76	-0.34	11.38	-0.001	12.67	0.03
	0.5	5.30	-0.25	11.18	-0.02	12.90	0.10
	1.0	6.86	-0.34	10.98	-0.02	13.57	0.15
0.75	0	3.03	-0.34	11.41	0.01	12.61	0.01
	0.1	3.35	-0.25	11.42	-0.001	12.58	0.03
	0.5	5.29	-0.18	11.19	-0.02	12.89	0.10
	1.0	6.90	-0.32	10.97	-0.02	13.54	0.16
	2.0	8.44	-0.47	10.86	-0.01	14.82	0.20
0.5	0	2.70	-0.29	11.44	0.01	12.56	0.01
	0.1	3.06	-0.17	11.44	-0.001	12.52	0.04
	0.5	5.33	-0.14	11.21	-0.02	12.86	0.11
	1.0	6.93	-0.30	10.97	-0.02	13.53	0.16
	2.0	8.45	-0.46	10.86	-0.02	14.75	0.20
0.1	0	1.85	-0.15	11.48	0.01	12.47	0.01
	0.1	2.43	0.17	11.49	-0.001	12.43	0.04
	0.5	5.48	-0.08	11.20	-0.03	12.81	0.11
	1.0	7.00	-0.28	10.97	-0.02	13.51	0.16
	2.0	8.47	-0.46	10.86	-0.01	14.75	0.20

Filter: $\frac{150\,(S + 2)}{S^2 + 35S + 300}$

KA	KR	Short Period Mode ω	Short Period Mode ζ	Elastic Modes 1 ω	Elastic Modes 1 ζ	Elastic Modes 2 ω	Elastic Modes 2 ζ
1.2	0	2.81	0.24	11.53	-0.03	12.01	0.08
	0.1	2.64	0.32	11.80	-0.07	11.43	0.07
	0.5	2.08	0.52	12.21	-0.20	10.90	0.04
	1.0	1.70	0.65	12.83	-0.31	10.86	0.02
0.75	0	2.35	0.18	11.62	-0.02	12.07	0.05
	0.1	2.22	0.26	11.98	-0.06	11.43	0.05
	0.5	1.81	0.48	12.33	-0.20	10.92	0.04
	1.0	1.50	0.64	12.89	-0.31	10.87	0.02
	2.0	1.18	0.85	14.06	-0.43	10.87	0.02
0.5	0	2.10	0.14	11.64	-0.01	12.13	0.04
	0.1	2.00	0.23	12.09	-0.06	11.42	0.05
	0.5	1.66	0.46	12.39	-0.19	10.93	0.04
	1.0	1.38	0.64	12.93	-0.30	10.87	0.02
	2.0	1.10	0.87	14.07	-0.43	10.87	0.02

Filter: $\frac{1.85\,(S^2 + 2S + 122)}{S^2 + 30S + 225}$

KA	KR	Short Period Mode ω	Short Period Mode ζ	Elastic Modes 1 ω	Elastic Modes 1 ζ	Elastic Modes 2 ω	Elastic Modes 2 ζ
1.2	0	2.30	-0.08	11.51	0.01	12.40	0.01
	0.1	2.35	-0.03	11.50	0.01	12.42	0.01
	0.5	2.62	0.17	11.49	0.01	12.51	-0.01
	1.0	3.47	0.42	11.47	0.02	12.63	-0.02
0.75	0	2.07	-0.04	11.50	0.01	12.42	0.01
	0.1	2.12	0.02	11.50	0.01	12.44	0.01
	0.5	2.39	0.26	11.49	0.02	12.54	-0.01
	1.0	3.62	0.54	11.46	0.02	12.65	-0.02
	2.0	5.96	0.32	11.42	0.02	12.90	-0.05
0.5	0	1.92	-0.01	11.50	0.01	12.42	0.01
	0.1	1.97	0.05	11.50	0.01	12.44	0.01
	0.5	2.25	0.32	11.48	0.01	12.53	-0.01
	1.0	3.85	0.49	11.46	0.02	12.66	-0.02
	2.0	6.02	0.32	11.41	0.02	12.91	-0.05

Figure 4-3. Single-Sensor Ascent Pitch Control System (Sheet 2 of 3)

VARIOUS FILTERS USED IN SINGLE-SENSOR ASCENT PITCH CONTROL SYSTEM

Filter: $\frac{S^2 + 3.7S + 225}{S^2 + 30S + 225}$

KA	KR	Short Period Mode		Elastic Modes 1		Elastic Modes 2	
		ω	ζ	ω	ζ	ω	ζ
1.2	0	2.31	-0.08	11.49	0.01	12.44	0.01
	0.1	2.36	-0.03	11.52	0.01	12.39	0.01
	0.5	2.64	0.18	11.71	0.004	12.11	0.02
	1.0	3.56	0.46	11.80	-0.03	11.92	0.05
0.75	0	2.08	-0.04	11.49	0.01	12.44	0.01
	0.1	2.12	0.02	11.52	0.01	12.39	0.01
	0.5	2.41	0.27	11.73	0.004	12.10	0.02
	1.0	3.75	0.59	11.82	-0.03	11.90	0.05
	2.0	6.69	0.32	11.70	-0.06	11.79	0.08
0.5	0	1.93	-0.01	11.49	0.01	12.44	0.01
	0.1	1.97	0.05	11.52	0.01	12.39	0.01
	0.5	2.26	0.33	11.74	0.01	12.09	0.01
	1.0	4.05	0.64	11.83	-0.03	11.89	0.05
	2.0	6.76	0.32	11.71	-0.06	11.78	0.08

Filter: $\frac{100\,(1 + S)}{S^2 + 20S + 100}$

KA	KR	Short Period Mode		Elastic Modes 1		Elastic Modes 2	
		ω	ζ	ω	ζ	ω	ζ
1.2	0	4.19	0.21	11.36	-0.03	12.42	0.09
	0.1	4.40	0.52	11.46	-0.06	11.56	0.10
	0.5	1.80	0.71	11.47	-0.24	10.72	0.03
	1.0	1.35	0.71	12.18	-0.37	10.80	0.02
0.75	0	3.03	0.28	11.47	-0.02	12.35	0.06
	0.1	2.56	0.48	11.67	-0.06	11.51	0.08
	0.5	1.55	0.60	11.63	-0.23	10.75	0.03
	1.0	1.19	0.65	12.25	-0.36	10.81	0.02
	2.0	0.89	0.75	13.52	-0.49	10.85	0.01
0.5	0	2.44	0.24	11.52	-0.01	12.33	0.05
	0.1	2.12	0.37	11.79	-0.06	11.47	0.06
	0.5	1.41	0.53	11.71	-0.23	10.77	0.03
	1.0	1.10	0.62	12.29	-0.36	10.81	0.02
	2.0	0.83	0.74	13.53	-0.48	10.85	0.01

Filter: $\frac{1.55\,(S^2 - 12S + 145)}{S^2 + 30S + 225}$

KA	KR	Short Period Mode		Elastic Modes 1		Elastic Modes 2	
		ω	ζ	ω	ζ	ω	ζ
1.2	0	2.30	-0.08	11.50	0.01	12.42	0.01
	0.1	2.35	-0.03	11.51	0.01	12.42	0.01
	0.5	2.63	0.17	11.55	0.01	12.40	0.004
	1.0	3.52	0.43	11.58	0.02	12.40	-0.01
0.75	0	2.07	-0.04	11.50	0.01	12.43	0.01
	0.1	2.12	0.02	11.51	0.01	12.42	0.01
	0.5	2.40	0.26	11.54	0.01	12.41	0.004
	1.0	3.68	0.55	11.58	0.02	12.41	-0.01
	2.0	6.16	0.31	11.62	0.03	12.45	-0.04
0.5	0	1.92	-0.01	11.50	0.01	12.43	0.01
	0.1	1.97	0.05	11.50	0.01	12.43	0.01
	0.5	2.26	0.32	11.54	0.01	12.42	0.004
	1.0	3.93	0.60	11.58	0.02	12.42	-0.01
	2.0	6.22	0.31	11.61	0.03	12.46	-0.04

Figure 4-3. Single-Sensor Ascent Pitch Control System (Sheet 3 of 3)

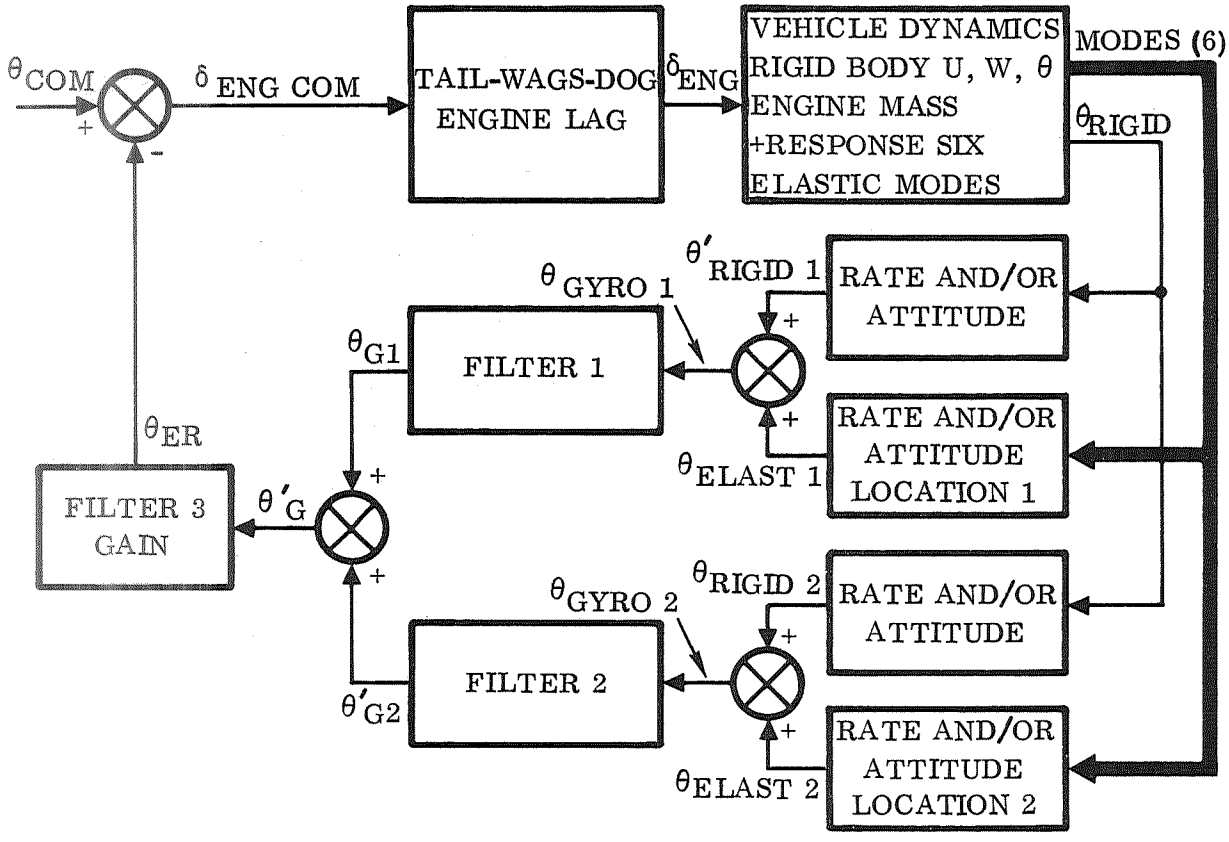

Figure 4-4. Block Diagram of Pitch Plane Two-Sensor Ascent Control System

and the weight penalty associated with the addition of a canard is 5000 pounds. Since fatigue damage is not critical in space shuttle design and a basic, stable pitch control system is possible with TVC, the conclusion can be drawn that no further considerations be given to additional pitch plane aerodynamic control elements. The ascent yaw plane vibration modes present the same problems as the pitch plane modes with the exception that a new mode called the "scissors mode" is added. The scissors mode has the properties that the orbiter and booster are yawing in opposite directions (as rigid bodies). This mode is produced by the interstage roll/yaw flexibility. Table 4-4 presents the yaw mode frequencies. Figure 4-7 presents a root locus using sensors, rate, and attitude gyros, located in both the nose and tail. As in the pitch plane, a stable system was realized and the modal damping was increased by a factor of two.

Increased modal damping can be obtained by using the orbiter rudder to provide large generalized forces when the dynamic pressure is relatively high. Figure 4-8 presents a root locus for maximum dynamic pressure with (1) sensors located on the tail of the orbiter, (2) orbiter rudder controller, and (3) the booster two-sensor TVC system. Structural modal damping can be improved by a factor of 10. The penalty associated with this system is to provide hydraulic power to the rudder during a portion of flight when the orbiter hydraulic power would normally not be used. It has been estimated that 100 pounds of orbiter weight would be necessary. The 100-pound penalty is

Filter: Filter 1 = 1; $\frac{30}{S+30}$ = Filter 2; Gyro 2 gain = 2; Gyro 1 gain = 1

KA	KR	Short Period Mode		Phugoid Mode		Elastic Modes											
						1		2		3		4		5		6	
		ω	ζ	ω	ζ	ω	ζ	ω	ζ	ω	ζ	ω	ζ	ω	ζ	ω	ζ
1.2	0	2.24	0.02	0.07	0.65	11.57	0.01	12.79	-0.05	13.87	0.01	25.83	0.01	31.21	0.01	65.41	0.01
	0.1	2.25	0.05	0.07	0.65	11.57	0.01	13.52	-0.02	13.86	0.01	25.83	0.01	31.20	0.01	65.06	0.02
	0.5	2.35	0.19	0.07	0.64	11.59	0.01	16.28	0.01	13.83	0.01	25.83	0.01	31.20	0.01	63.56	0.04
	1.0	2.73	0.30	0.07	0.64	11.60	0.01	18.52	0.01	13.83	0.01	25.83	0.01	31.12	0.01	61.74	0.06
0.75	0	2.06	0.03	0.07	0.59	11.55	0.01	12.64	-0.03	13.85	0.01	25.83	0.01	31.12	0.01	65.38	0.01
	0.1	2.07	0.07	0.07	0.59	11.56	0.01	13.41	-0.002	13.87	0.01	25.83	0.01	31.20	0.01	65.03	0.02
	0.5	2.22	0.25	0.07	0.58	11.59	0.01	16.29	0.02	13.83	0.01	25.83	0.01	31.17	0.01	63.54	0.04
	1.0	2.78	0.36	0.07	0.57	11.60	0.01	18.54	0.02	13.84	0.01	25.83	0.01	31.17	0.01	61.73	0.06
	2.0	3.37	0.25	0.07	0.54	11.60	0.01	21.01	0.004	13.84	0.01	25.83	0.01	31.05	0.01	58.89	0.07

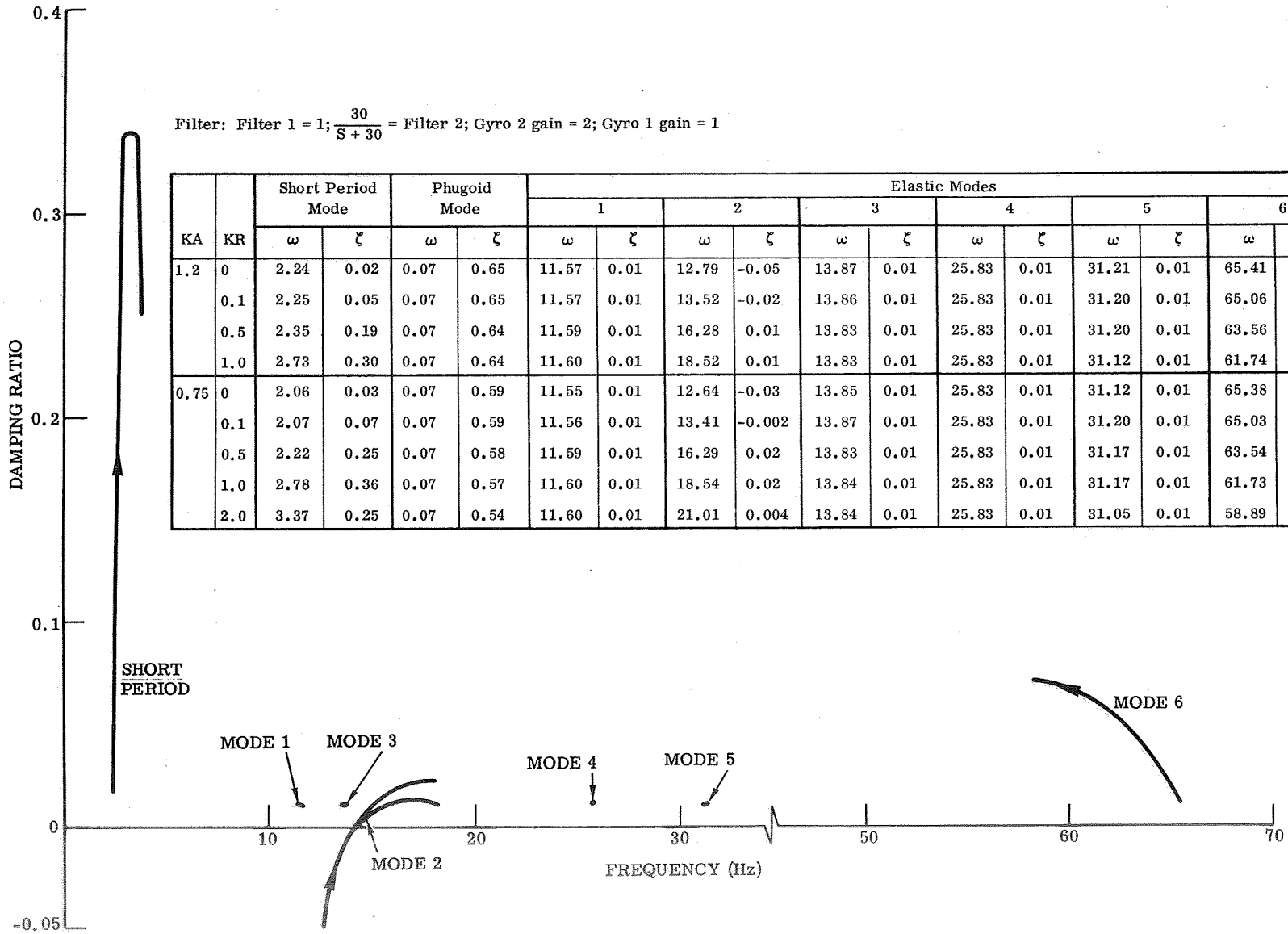

Figure 4-5. Two-Sensor Ascent Pitch Control System

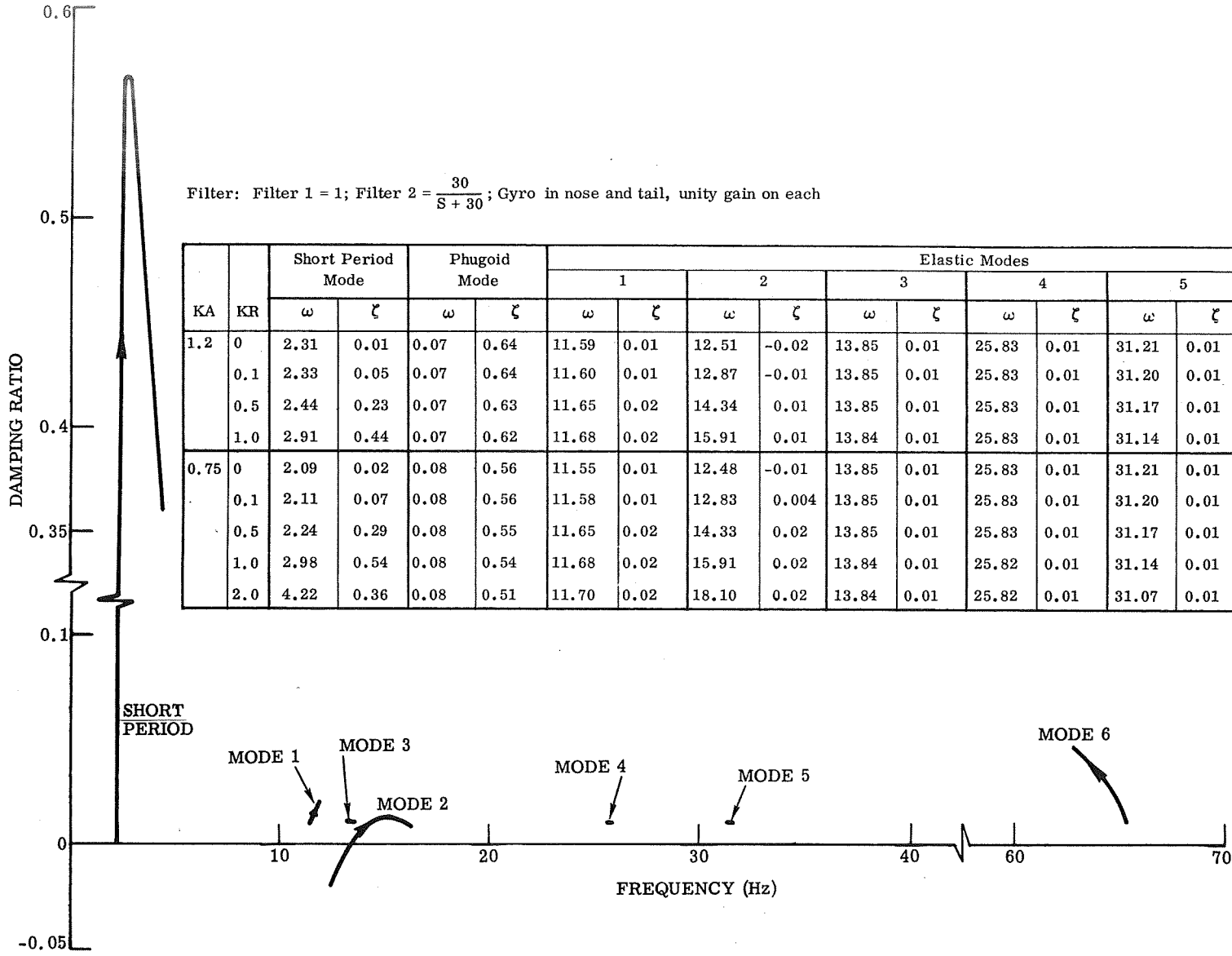

Filter: Filter 1 = 1; Filter 2 = $\frac{30}{S + 30}$; Gyro in nose and tail, unity gain on each

		Short Period Mode		Phugoid Mode		Elastic Modes											
						1		2		3		4		5		6	
KA	KR	ω	ζ	ω	ζ	ω	ζ	ω	ζ	ω	ζ	ω	ζ	ω	ζ	ω	ζ
1.2	0	2.31	0.01	0.07	0.64	11.59	0.01	12.51	-0.02	13.85	0.01	25.83	0.01	31.21	0.01	65.37	0.01
	0.1	2.33	0.05	0.07	0.64	11.60	0.01	12.87	-0.01	13.85	0.01	25.83	0.01	31.20	0.01	65.20	0.01
	0.5	2.44	0.23	0.07	0.63	11.65	0.02	14.34	0.01	13.85	0.01	25.83	0.01	31.17	0.01	64.50	0.03
	1.0	2.91	0.44	0.07	0.62	11.68	0.02	15.91	0.01	13.84	0.01	25.83	0.01	31.14	0.01	63.59	0.04
0.75	0	2.09	0.02	0.08	0.56	11.55	0.01	12.48	-0.01	13.85	0.01	25.83	0.01	31.21	0.01	65.35	0.01
	0.1	2.11	0.07	0.08	0.56	11.58	0.01	12.83	0.004	13.85	0.01	25.83	0.01	31.20	0.01	65.19	0.01
	0.5	2.24	0.29	0.08	0.55	11.65	0.02	14.33	0.02	13.85	0.01	25.83	0.01	31.17	0.01	64.48	0.03
	1.0	2.98	0.54	0.08	0.54	11.68	0.02	15.91	0.02	13.84	0.01	25.82	0.01	31.14	0.01	63.58	0.04
	2.0	4.22	0.36	0.08	0.51	11.70	0.02	18.10	0.02	13.84	0.01	25.82	0.01	31.07	0.01	61.82	0.06

Figure 4-5. Two-Sensor Ascent Pitch Control System, Contd

Filter: None; Gyro in nose and tail, unity gain on each

KA	KR	Short Period Mode		Phugoid Mode		Elastic Modes											
						1		2		3		4		5		6	
		ω	ζ	ω	ζ	ω	ζ	ω	ζ	ω	ζ	ω	ζ	ω	ζ	ω	ζ
1.2	0	2.31	0.001	0.07	0.64	11.57	0.01	12.70	-0.01	13.85	0.01	25.83	0.01	31.21	0.01	65.30	0.01
	0.1	2.33	0.05	0.07	0.64	11.60	0.01	12.95	0.01	13.86	0.01	25.83	0.01	31.20	0.01	65.67	0.01
	0.5	2.45	0.23	0.07	0.63	11.68	0.01	14.27	0.10	13.84	0.01	25.83	0.01	31.17	0.01	62.64	0.004
	1.0	2.98	0.44	0.07	0.62	11.70	0.01	16.21	0.14	13.84	0.01	25.83	0.01	31.13	0.01	60.83	-0.001
0.75	0	2.09	0.02	0.08	0.56	11.55	0.01	12.60	-0.002	13.85	0.01	25.83	0.01	31.21	0.01	65.31	0.01
	0.1	2.11	0.07	0.08	0.56	11.58	0.01	12.85	0.02	13.86	0.01	25.83	0.01	31.20	0.01	64.68	0.01
	0.5	2.25	0.30	0.08	0.55	11.68	0.01	14.21	0.11	13.85	0.01	25.83	0.01	31.17	0.01	62.65	0.002
	1.0	3.07	0.56	0.08	0.54	11.71	0.01	16.21	0.15	13.84	0.01	25.83	0.01	31.13	0.01	60.83	-0.002
	2.0	4.40	0.32	0.08	0.51	11.72	0.01	19.03	0.14	13.85	0.01	25.83	0.01	31.06	0.01	58.50	-0.01
0.5	0	1.94	0.03	0.08	0.52	11.53	0.01	12.54	0.004	13.85	0.01	25.83	0.01	31.21	0.01	65.32	0.01
	0.1	1.96	0.09	0.08	0.51	11.58	0.01	12.79	0.03	13.85	0.01	25.83	0.01	31.20	0.01	64.69	0.01
	0.5	2.12	0.35	0.08	0.50	11.68	0.01	14.18	0.11	13.85	0.01	25.83	0.01	31.17	0.01	62.65	0.004
	1.0	3.29	0.62	0.08	0.48	11.71	0.01	16.21	0.15	13.84	0.01	25.83	0.01	31.13	0.01	60.84	-0.004
	2.0	4.44	0.32	0.08	0.45	11.72	0.01	19.04	0.14	13.85	0.01	25.82	0.01	31.06	0.01	58.50	-0.01

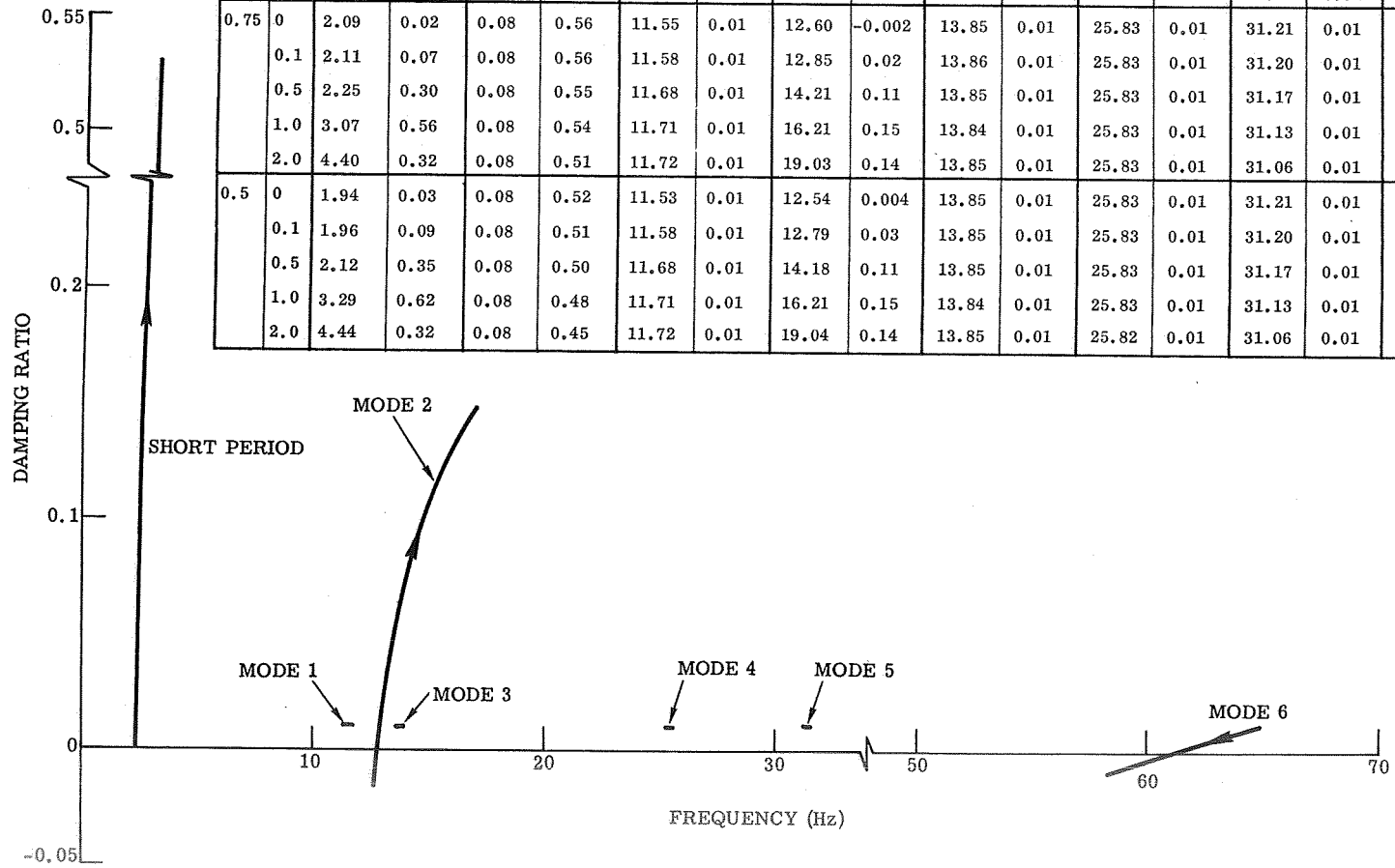

Figure 4-5. Two-Sensor Ascent Pitch Control System, Contd

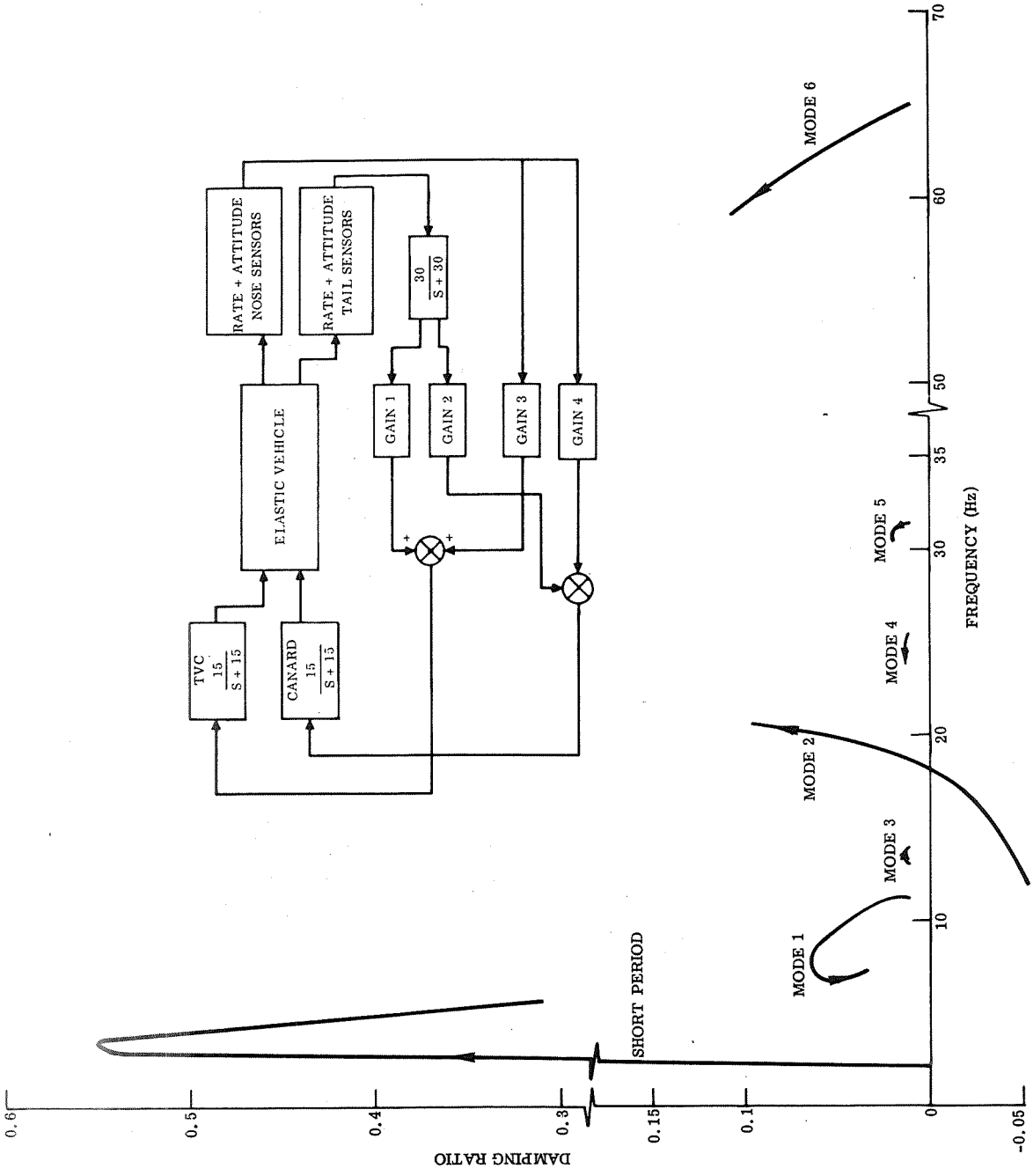

Figure 4-6. Two-Sensor, Two-Controller Ascent Pitch Control System

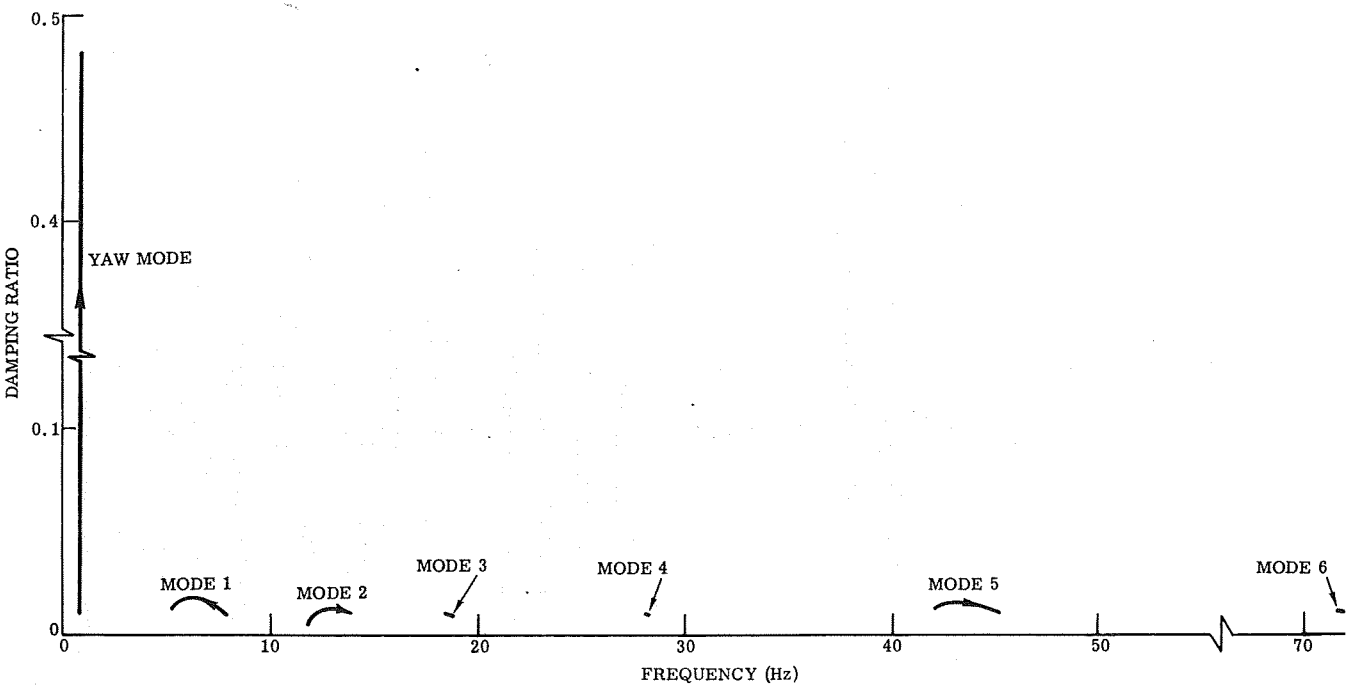

Figure 4-7. Two-Sensor Ascent Yaw Control System

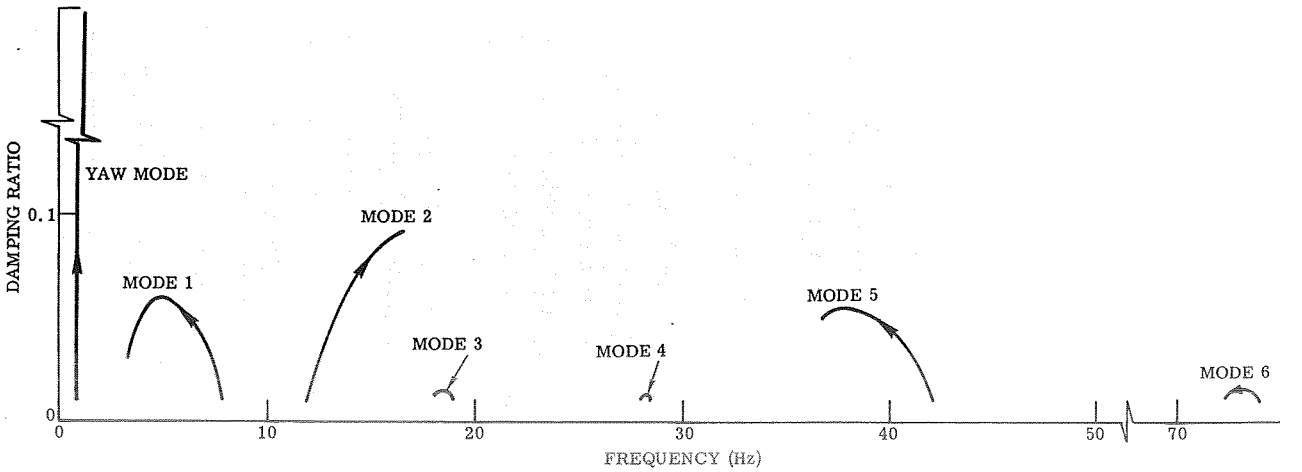

Figure 4-8. Two-Sensor Orbiter Rudder/Booster TVC Ascent Yaw Control System

Table 4-4. Fuselage Ascent Yaw Plane Mode Frequencies

Mode	Frequency	
	H_z	Rad/sec
1	1.25	7.85
2	1.90	11.9
3	3.00	18.8
4	4.50	28.2
5	6.70	42.0
6	11.50	72.0

based on normal operations of starting the hydraulic system at liftoff or just prior to liftoff. The modal suppression peak hydraulic power requirements are less than design requirements and therefore, will not change hydraulic power supply design. This system would not provide modal damping during early portions of flight when the scissor mode is at the lowest frequency.

4.2 WING MODAL STABILIZATION

These wing structural modes are stable without mode stabilization. The basic uncontrolled stability was verified by flutter analysis. Classical wing instability can only occur in the presence of air forces and is known as flutter. The methods described herein were developed to provide improved damping and can be used for future space shuttle configurations if improved damping is required.

The characteristics of the straight-wing space shuttle are such that the wing structural modes can be separated from the fuselage. Table 4-5 presents the first five booster wing structural modes. The baseline booster and orbiter wing has a high response aileron located on the last 30 percent of the trailing edge. An aerodynamic surface appears to be the only practical method of generating generalized forces of sufficient magnitude to damp the structural modes. At maximum dynamic pressure, the booster aileron generates 4000 pounds per degree. The space shuttle program is developing a new large attitude control propulsion system (ACPS) with 1500 pounds of thrust capability. Therefore, three ACPS motors in each wing tip would be equivalent to the force requirements. The ACPS fuel expenditures have been estimated to be 1000 pounds for an I_{SP} of 400 seconds. This study analyzed only aerodynamic controllers.

The analysis considered only the first five wing structural modes since the ailerons or wing flaps produced very little pitching moment and the plunging mode couples through weak aerodynamic forces. Rate gyros located at 25 percent, 50 percent, and the wing tip were used to sense slopes of modal deflections. Signals from identical sensors mounted on opposite wings are differenced to remove the rigid body roll component.

Table 4-5. Wing Structural Mode Frequencies

Mode	Frequency H_z	Rad/sec
1	3.38	22.25
2	4.11	25.90
3	4.97	31.20
4	8.70	54.65
5	11.34	71.20

If considerations are given only to the first mode, a system as presented in Figure 4-9 can increase the structural mode damping from 0.01 to 0.3. Various lead-lag and second-order filters were applied to the gyro signal. Best results were obtained from a first-order lead at 10 radians/second and a first-order lag at 50 radians/second.

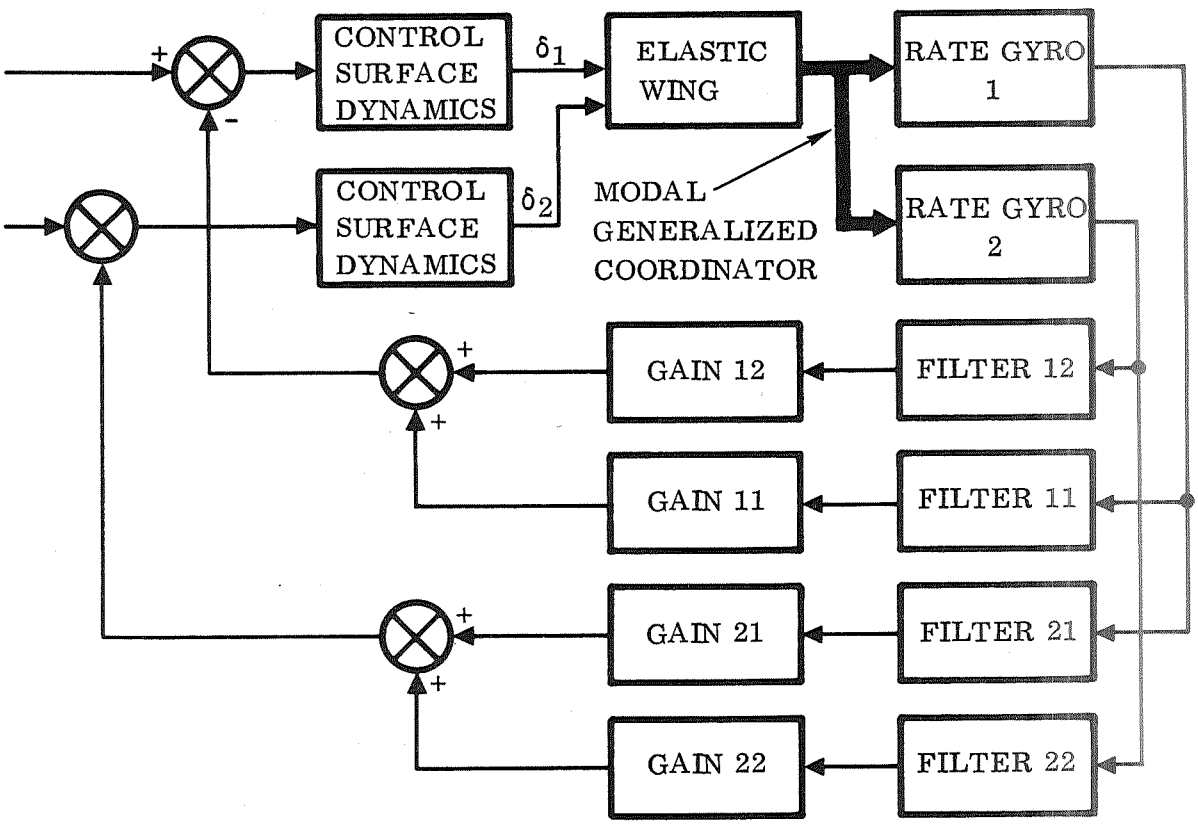

Figure 4-9. Block Diagram of Wing Modal Suppression Control System

A five-mode analysis showed that with only one control surface no filter or combinations of filters could be found that produced a stable system. While the first and second structural modes were well damped, the third and fifth modes were driven unstable. Due to the shapes of the modes, the generalized forces produced by the ailerons were very destabilizing for the third and fifth mode.

An aerodynamic control surface was introduced at approximately the wing semi-span. The generalized forces produced by this controller were stabilizing for all modes. These wing modal control surfaces were of sufficiently high frequency to avoid adverse interference with the rigid body control and not to require high-pass filters. It was found that the best system consisted of driving the control surface located at the semi-span with a signal derived from a sensor located at 50 percent of the span and to drive the tip control surface with a sensor located near the wing tip. This system closely approximates the general mode suppression controller/sensor location described in Reference 7. With the above system the wing modal damping for all five modes was increased from 0.01 to 0.1. A significant increase in damping was obtained with the addition of a high-response control surface. The addition of such a control surface would increase the vehicle weight by 4000 pounds. This weight includes hydraulic equipment necessary to provide peak rates of 50 deg/sec. Figure 5-10 presents a root locus of the two-sensor, two-controller system.

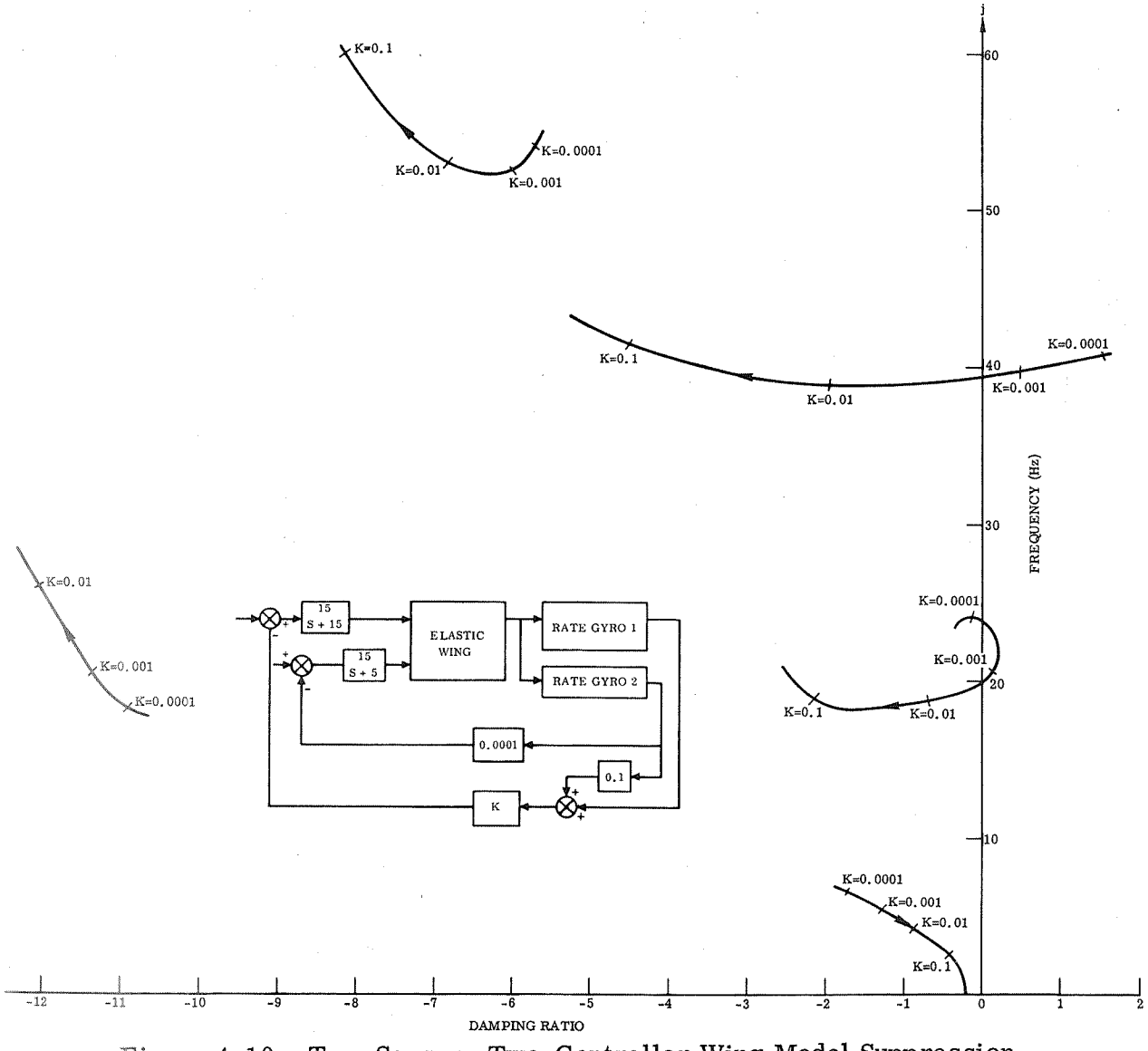

Figure 4-10. Two-Sensor, Two-Controller Wing Modal Suppression

SECTION 5

AERODYNAMIC EFFECTS

Significant effort was expended to define the unsteady aerodynamics which affect control, stability, and loads. These aerodynamic forces are due to elastic modal defection, vortex shedding, shock interference, flow reparation, and buffeting. Vortex shedding, shock interference effects and buffeting can not be predicted analytically and, therefore, to include their effects in load alleviation design, wind tunnel data on similar configurations was used.

5.1 MODAL AERODYNAMICS

Many unsteady aerodynamic theories can be used to estimate the aerodynamic coupling between elastic modes. For the subsonic case, either the Kernel function (Reference 12) or doublet lattice (Reference 13) are applicable. Mach box theory (Reference 14) is suited for the supersonic flight phases. However, after careful analysis the use of steady-state aerodynamics in the standard "quasi-steady" approach is most suitable for space shuttle.

Parallel-mounted vehicles, such as the proposed space shuttle vehicle, exhibit extremely complex aerodynamic flow characteristics. Studies (Reference 15) reveal that unsteady aerodynamic theories do not properly account for body-body, body-wing, and wing-wing interference at Mach numbers below hypersonic. Quasi-steady aerodynamics, such as the Woodward theory, were used to account for the interference effects.

Steady-state aerodynamics have been used successfully to derive generalized forces for dynamic response and flutter problems in the low to moderate reduced frequency range. The approach used was to compute the pressure at a point j due to a unit downwash at the point i. The resulting influence matrix then relates the arbitrary motion of each segment of the vehicle to an overall pressure distribution.

The use of steady-state aerodynamics to solve response problems, referred to as the "quasi-steady" approach, gained interest following the work of Pines (Reference 16) and Zimmerman (Reference 17). Results have been compared to experimental and prediction based on Theodorsen's unsteady theory. In all cases, the quasi-steady method gave better agreement with experiment than did unsteady theory. The steady-state aerodynamic center (a.c.) was found to be at a 32% chord, and this location was specified in the quasi-steady analysis. In the unsteady approval, however, the aerodynamic center is inherently at the quarter-chord.

Woodward's steady-state method (Reference 18) was used by Brignac and Shelton (Reference 19) in flutter and dynamic analysis of the F-111 horizontal stabilizer. Analytical and experimental results were compared for Mach numbers of 1.09 and 1.37. At Mach 1.09, where no applicable unsteady aerodynamic theory was available, the predicted flutter velocity using Woodward aerodynamics was eight percent low and the flutter frequency was two percent high. This is a remarkable correlative, considering the transonic Mach number and the relatively high reduced frequency at flutter (about 0.8 based on the mean semi-chord). At Mach 1.37, the predicted flutter speed using the Woodward method agreed exactly with test results. Unsteady Mach box theory applied to this condition yielded a three percent higher flutter speed.

It becomes evident that in some cases the use of steady-state aerodynamics yields more accurate dynamic response and flutter calculation than does unsteady aerodynamic theory. Unsteady lag effects are in some cases less important than the proper definitions of steady-state effects due to interference. The Woodward theory has also been compared to steady-state aerodynamic characteristics of the B-58 airplane. Excellant correlation between the theory and wind tunnel data has been obtained for typical pressure distribution.

The space shuttle launch configuration was subdivided into a large number of quadrilateral panels for the application of the Woodward theory. Figure 5-1 presents the Woodward model. These panels define the boundaries of planar singularities used to simulate the effects of wing lift, thickness, and wing-body interference. Additional line singularities located along the body axis are used to simulate the lift and volume effects of the body. A unit downwash was applied at the center of each panel to obtain the pressure distribution over the entire configuration. The pressure is computed at the center of each panel and is assumed constant over the entire panel. The aerodynamic influence matrix was obtained so that the aerodynamics effects of elastic modal velocities and displacements could be derived.

For this study the Woodward theory was used only to develop the modal aerodynamic coefficients. The rigid-body load distribution and total forces and moments were derived from wind tunnel data. This data was obtained for the complete range of Mach numbers needed for this study. The wind tunnel data includes the effects of flow interference, shock impingement, and separated flow. The rigid-body loads obtained from the Woodward theory were compared to the wind tunnel data. Good correlation was obtained. In the pitch plane, the correlation was within 10 percent and in the yaw plane good correlation was obtained for all values except rolling moment due to sideslip. Shock impingement or interference produce large discrepancies in this parameter.

Figures 5-2 through 5-6 present the modal aerodynamic data for the launch configuration. These coefficients are used in the following way:

$$C_{1\alpha}\alpha + M_1\ddot{\zeta}_1 + \bar{C}_{11}\dot{\zeta}_1 + C_{11}\zeta_1 + K_1\zeta_1 + \bar{C}_{12}\dot{\zeta}_2 + C_{12}\zeta_2 + \ldots + \bar{C}_{15}\dot{\zeta}_5 + C_{15}\zeta = C_{1G}$$

$$\vdots$$

$$C_{5\alpha}\alpha + \bar{C}_{51}\dot{\zeta}_1 + C_{51}\zeta_1 + \ldots M_5\ddot{\zeta}_5 + \bar{C}_{55}\dot{\zeta}_5 + C_{55}\zeta_5 + K_5\zeta_5 = C_{5G}$$

where

C_{ij} = modal generalized aerodynamic force coefficient

$\bar{C}_{ij}$ = modal generalized aerodynamic damping force coefficient

M_i = modal generalized masses

K_i = modal generalized spring forces

α = rigid body angle of attack

C_{iG} = modal generalized just force coefficient

$C_{i\alpha}$ = modal generalized angle-of-attack force coefficient

These coefficients and equations were used in the modal stabilization analysis.

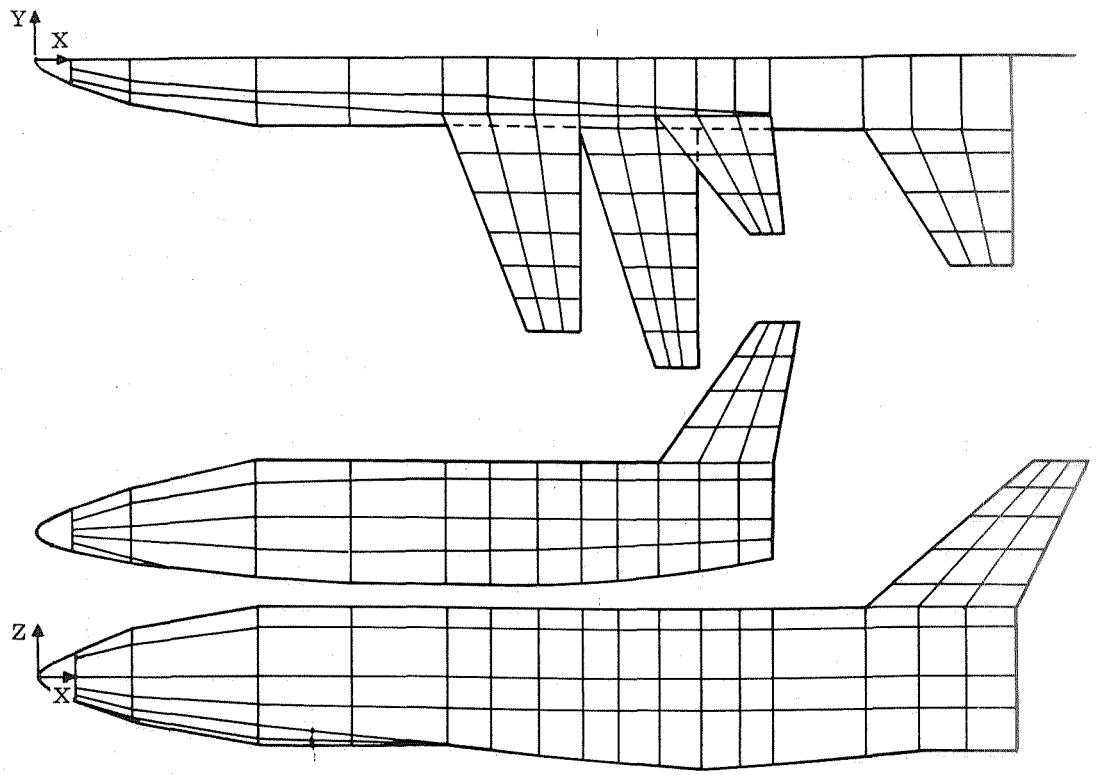

Figure 5-1. Aerodynamic Representation - Woodward Method

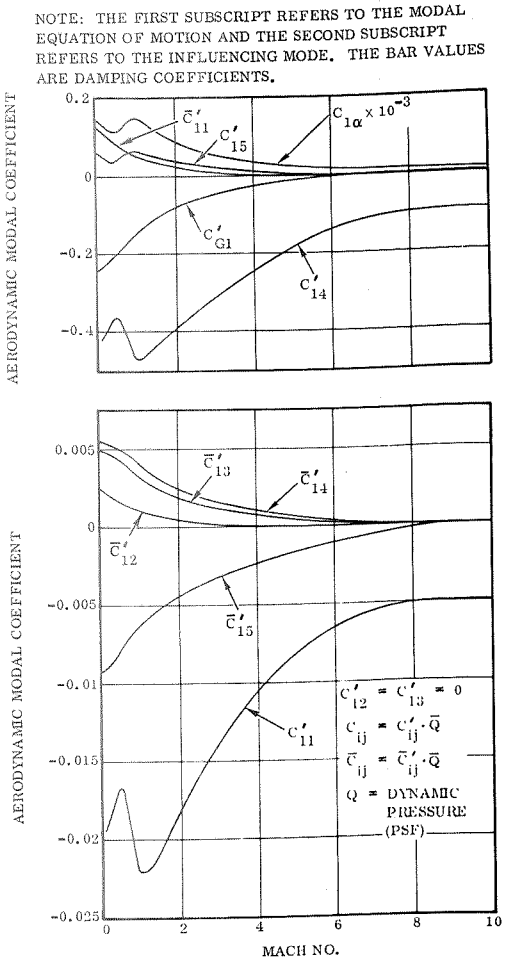

Figure 5-2. Launch Configuration Modal Aerodynamic Coefficients - Wing First Mode

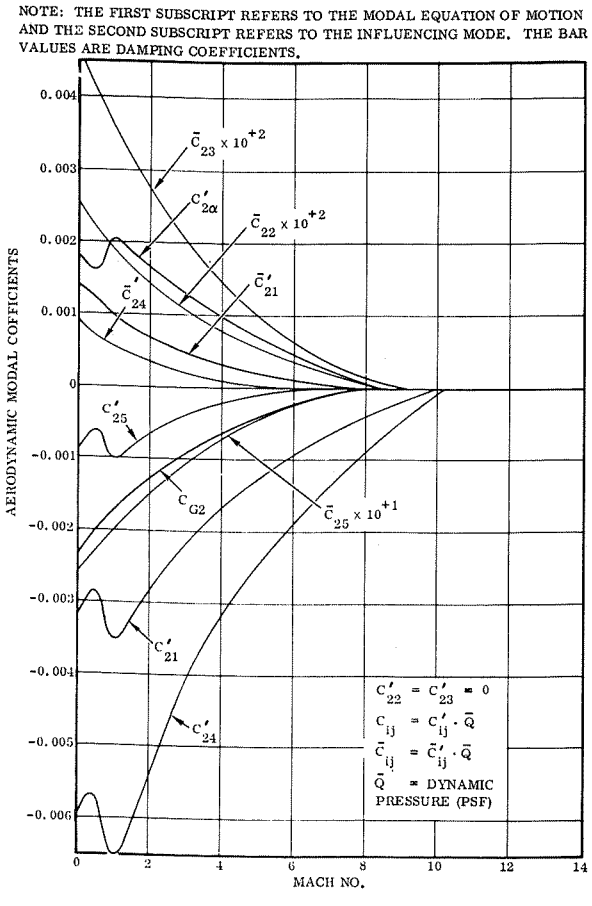

Figure 5-3. Launch Configuration Modal Aerodynamic Coefficients - Wing Second Mode

5.2 BUFFET EFFECTS

Since the proposed shuttle reenters at very high angles of attack (60°) and remains at these high angles of attack until deceleration to moderate subsonic Mach numbers, considerable concern has been given to buffet loads. The vehicle must also penetrate the transonic region at high dynamic pressure during the launch phase of flight.

Exploratory experimental studies of buffeting characteristics for semispan wall-mounted models of a clipped 50-degree delta and an unswept wing of aspect ratio = 7 have been conducted at Mach numbers from 0.2 to 2.0 at angles of attack from 0 to 90°. For Mach 0.3 and at about 9 degrees angle of attack the tests indicate the onset of buffeting. The buffeting response is characterized by random amplitude oscillation at the frequency of the wing fundamental bending mode. The buffeting persists throughout the angle-of-attack range. At Mach 0.8 buffeting occurs at all angles of

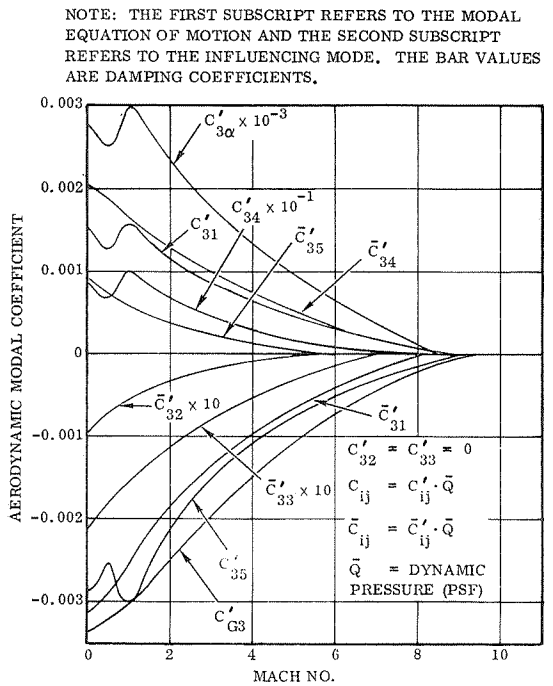

Figure 5-4. Launch Configuration Modal Aerodynamic Coefficients - Wing Third Mode

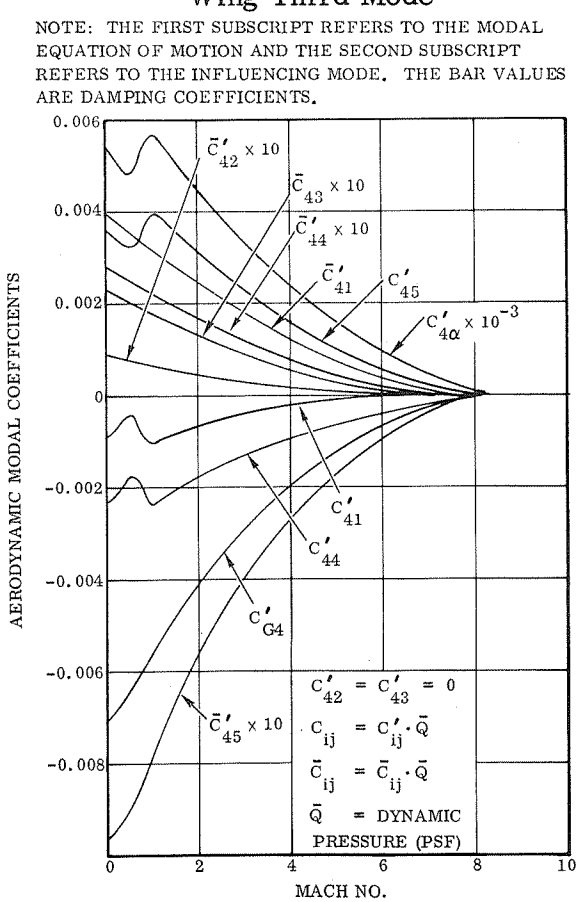

Figure 5-5. Launch Configuration Modal Aerodynamic Coefficients - Wing Fourth Mode

attack. For the supersonic Mach numbers the character of the buffeting is similar to the low subsonic Mach number, except buffet onset occurs at higher angles of attack. Figure 5-7 presents the buffet boundaries for wing similar to the configuration studied. Figure 5-8 presents the relative maximum buffet intensity for the straight wing over the subsonic-transonic portion of flight. The relative intensity is the ratio of the peak root-bending moment to the static nonbuffeting root-bending moment. The largest factor, 0.15, occurs at about Mach 0.8. This factor was applied to the loads which were used in the fatigue analysis. For the number of occurrences of the load, the buffeting was assumed to occur at the wing first-bending frequency.

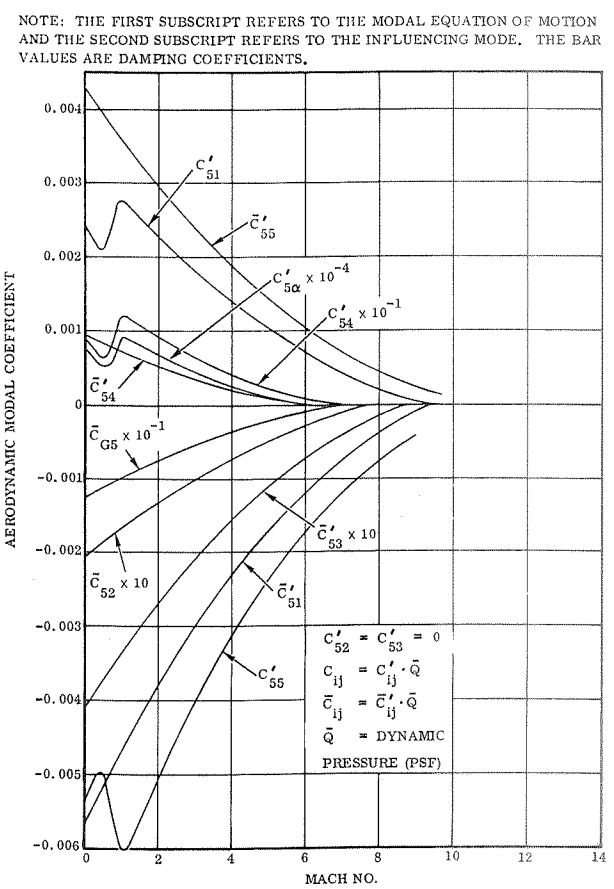

Figure 5-6. Launch Configuration Modal Aerodynamic Coefficients - Wing Fifth Mode

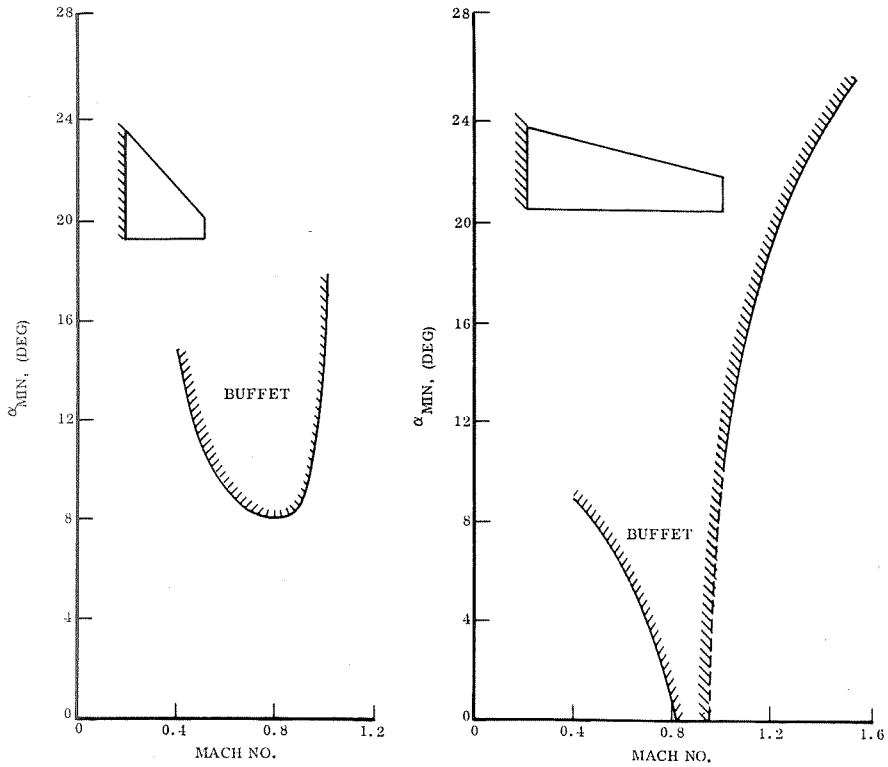

Figure 5-7. Buffet Boundaries

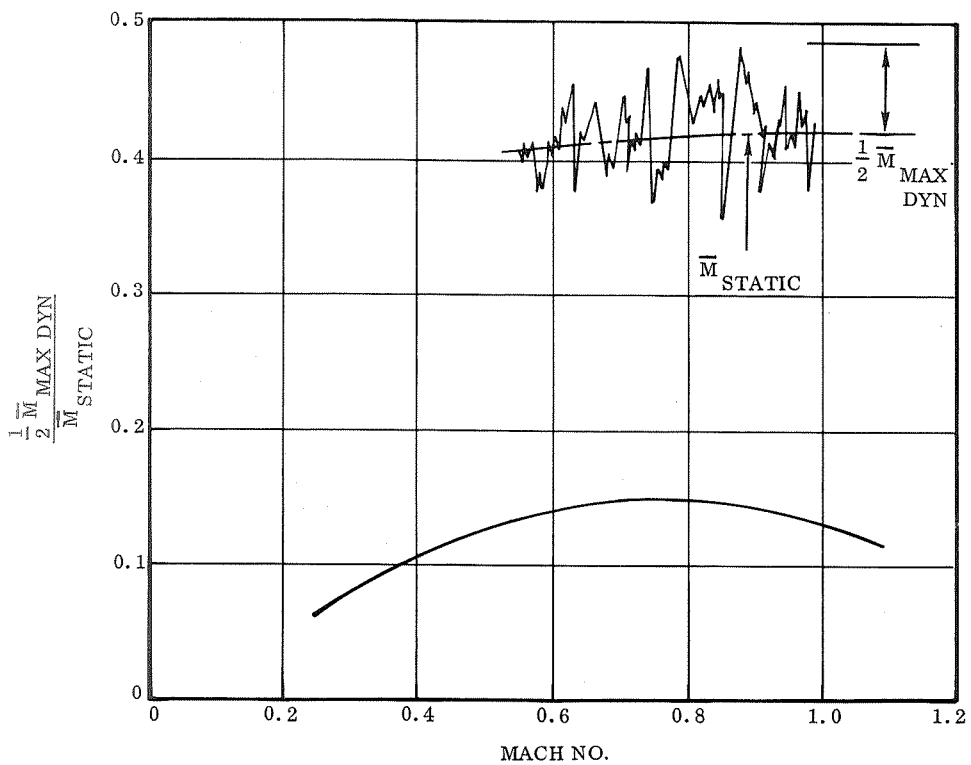

Figure 5-8. Relative Buffet Intensity for a Straight-Wing Configuration

SECTION 6

REFERENCES

1. Miner, M. A., "Linear Cumulative Damage Method of Analysis," Journal of Applied Mechanics, Volume 12, Secret 1945.

2. MIL-HDBK-5A, Metalic Material and Elements for Aerospace Vehicle Structures.

3. Nachtigall, A. S., Klima, S. J., Freche, J. C., "Fatigue Properties at Low Cycles," Journal of Materials, Volume 3, No. 2, American Society for Testing and Materials.

4. MIL-A-008866A, 31 March 1971, Military Specification Airplane Strength and Rigidity Reliability Requirements, Repeated Loads and Fatigue.

5. NASA SP-8057, Structural Design Criteria Applicable to a Space Shuttle, January 1971.

6. Smith, R. E. and Lum, E.L.S., "Linear Optimal Theory Applied to Active Structural Bending Control," AIAA Paper No. 66-970, November-December 1966.

7. Wykes, J. H. and Movi, A. S., "Techniques and Results of an Analytical Investigation into Controlling the Structural Modes of Flexible Aircraft," AIAA Symposium of Structural Dynamics and Aeroelasticity, August - September 1965, pp 419 to 433.

8. Hosenthien, H. H., and Borelli, M. R., "Self-Adaptive Tracking Filters," SAE Paper Aerospace Vehicle Flight Controls System Committee, July 8 to 10, 1964.

9. Hendrick, R. C., "The Sensor Blender Approach to Control of Flexible Vehicles," SAE Committee A-18 Paper, Aerospace Vehicle Flight Control Systems, New York, New York, July 8 to 10, 1964.

10. Gillooly R. R., "Control Through Digital Filtering with Application to Highly Elastic Boosters," McDonnell Aircraft Corporation, July 12, 1963.

11. Westerwick, R. A., "Use of Multiple Gyro Feedback to Control Flexible Missiles," SAE Committee A-18 Paper, Aerospace Vehicle Flight Control Systems, Miami Beach, Florida, December 1962.

12. Watkins, C.E., et al, On the Kernal Function of the Integral Equation Relating the Lift and Downwash Distribution of Oscillating Finite Wings in Subsonic Flow, NACA Report 1234, 1955.

13. Albano, E., and Rodden, W.P., "A Doublet Lattice Method for Calculating Lift Distributions on Oscillating Surfaces in Subsonic Flows," AIAA Paper No. 68-73, AIAA 6th Aerospace Sciences Meeting, New York. January 1968.

14. Donato, V.W., Huhn C.R. Jr., Supersonic Unsteady Aerodynamics for Wings with Trailing Edge Control Surfaces and Folded Tips, AFFDL-TR-68-30, August 1968.

15. Huntington, R.G., Aeroelastic Effects on Shuttle Vehicle Dynamics, Convair Aerospace Report 71-378, 1971.

16. Pines, S., "An Elementary Explanation of the Flutter Mechanism," Preceedings of the National Specialists Meeting on Dynamics and Aeroelasticity, Fort Worth, Texas, 6-7 November 1958.

17. Zimmerman, H.H., "Elementary Static Aerodynamics Adds Significance and Scope in Flutter Analyses," Structural Dynamics of High Speed Flight, ACR-62, Office of Naval Research, Vol. 1, pp. 28-84, April 1961.

18. Woodward, F.A., and Hague, D.S., A Computer Program for the Aerodynamic Analysis and Design of Wing-Body-Tail Combinations at Subsonic and Supersonic Speeds, Volume I: Theory and Program Utilization, Convair Aerospace Report ERR-FW-867, February 1969.

19. Brignac, W.J., and Shelton, D.A., "Quasi-Steady Supersonic Flutter Analysis of a Low Aspect Ratio Surface," paper presented at Aerospace Flutter and Dynamics Council Meeting, Dallas, Texas, 3 December 1970.

APPENDIX I

ASCENT PHASE EQUATIONS

To evaluate rigid body load alleviation and to determine load spectra for fatigue analysis a six degree-of-freedom digital computer simulation was used. This appendix lists the equations in the simulation. Figure I-1 presents the sign convention.

The translational equations are

$$\dot{u} = \frac{\Sigma F_x}{m} - q\,w + r\,v \tag{1}$$

$$\dot{v} = \frac{\Sigma F_y}{m} - ru + pw \tag{2}$$

$$\dot{w} = \frac{\Sigma F_z}{m} - pv + qu \tag{3}$$

The rotational equations about the body axes are

$$\dot{p} = \frac{\Sigma L}{I_{xx}} + \frac{I_{xz}}{I_{xx}} \cdot \dot{r} - \frac{(I_{zz} - I_{yy})}{I_{xx}} \cdot q \cdot r + \frac{I_{xz}}{I_{xx}} \cdot p \cdot q \tag{4}$$

$$\dot{q} = \frac{\Sigma M}{I_{yy}} + \frac{I_{xz}}{I_{yy}} \cdot (r^2 - p^2) - \frac{(I_{xx} - I_{zz})}{I_{yy}} \cdot p \cdot r \tag{5}$$

$$\dot{r} = \frac{\Sigma N}{I_{zz}} + \frac{I_{xz}}{I_{zz}} \cdot \dot{p} - \frac{(I_{yy} - I_{xx})}{I_{zz}} \cdot p \cdot q - \frac{I_{xz}}{I_{zz}} \cdot q \cdot r \tag{6}$$

For the forces

$$\Sigma F_x = -C_D(M) \cdot Q \cdot S + \text{Thrust (Altitude, Flow Rate)} - C_{D_\delta}(M) \cdot Q \cdot S \cdot \delta - (g_{\bar{x}} \cdot \ell_1 + g_{\bar{y}} \cdot \ell_2 + g_{\bar{z}} \cdot \ell_3) \tag{7}$$

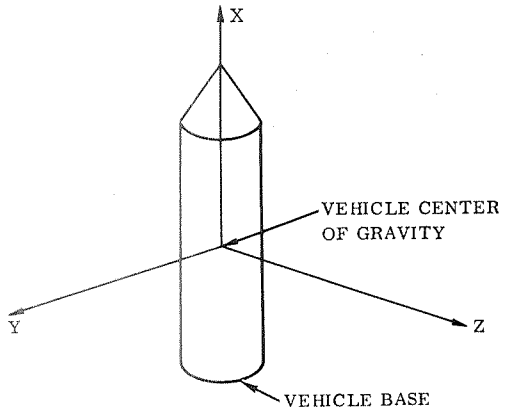

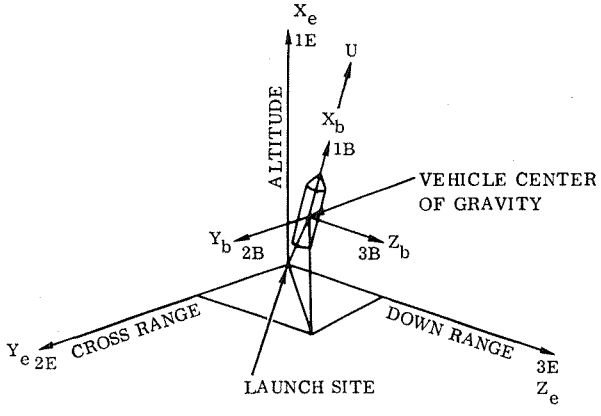

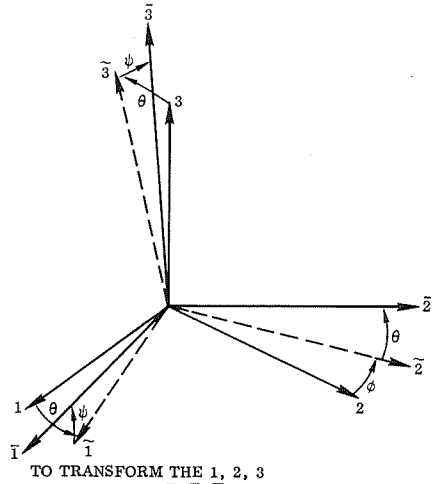

TO TRANSFORM THE 1, 2, 3
AXES INTO THE $\bar{1}$, $\bar{2}$, $\bar{3}$ AXES:

1. ROTATE THROUGH AN ANGLE ϕ ABOUT THE 3 AXIS
2. ROTATE THROUGH AN ANGLE θ ABOUT THE $\tilde{2}$ AXIS
3. ROTATE THROUGH AN ANGLE ψ ABOUT THE $\bar{2}$ AXIS

Figure I-1. Sign Convention

$$\Sigma F_y = C_{y_\beta}(M) \cdot Q \cdot S \cdot \beta - \text{Thrust} \cdot \delta_y + C_{y_{\delta_{Rud}}}(M) \cdot Q \cdot S \cdot \delta_{Rud} \tag{8}$$

$$- (g_{\bar{x}} \cdot m_1 + g_{\bar{y}} \cdot m_2 + g_{\bar{z}} \cdot m_3)$$

$$\Sigma F_z = -(C_{N_o}(M) + C_{N_\alpha}(M)\,\alpha) \cdot Q \cdot S + \text{Thrust} \cdot \delta_P + C_{z_{\delta_z}}(M) \cdot Q \cdot S \cdot \delta_z \tag{9}$$

$$- (g_{\bar{x}} \cdot n_1 + g_{\bar{y}} \cdot n_2 + g_{\bar{z}} \cdot n_3)$$

and the moments are

$$\Sigma L = \left(C_{l_\beta}(M) \cdot b + C_{y_\beta}(M) \cdot b_{ARM}\right) \cdot Q \cdot S \cdot \beta + C_{l_{\delta_l}} \cdot b \cdot Q \cdot S \cdot \delta_l \tag{10}$$

$$+ \text{Thrust} \cdot \delta_R$$

$$\Sigma M = \left(C_{m_o}(M)\,\bar{c} + C_{N_\alpha}(M) \cdot (CG(t) - CP_\alpha(M))\alpha + C_D(M) \cdot \text{Dragarm}\right) \cdot Q \cdot S$$

$$+ \text{Thrust} \cdot \delta_p \cdot \text{ARMX} + \text{Thrust} \cdot (CG(t) - TL_B) + C_{m_{\delta_z}}(M) \cdot Q \tag{11}$$

$$\cdot S \cdot \delta_z + \text{Thrust} \cdot \left(Z_{CG} - Z_{\text{Thrust}}\right)$$

$$\Sigma N = \left(C_{n_\beta}(M) \cdot b + C_{y_\beta}(M) \cdot (CP_\beta(M) - CG(t))\right) \beta \cdot Q \cdot S \tag{12}$$

$$+ \text{Thrust} \cdot \delta_y \cdot \text{ARMX} + C_{n_{\delta_{Rud}}}(M) \cdot Q \cdot S \cdot \delta_{Rud}$$

The direction cosine matrix is used throughout. These equations are

$$\left.\begin{aligned} \dot{\ell}_i &= m_i r - n_i q \\ \dot{m}_i &= n_i p - \ell_i r \\ \dot{n}_i &= \ell_i q - m_i p \end{aligned}\right\} \qquad i = 1, 2, 3 \tag{13}$$

Also used are the Euler angles θ, ϕ, ψ defined in the standard aircraft convention

$$\dot{\psi} = (r \cos\phi + q \sin\phi)/\cos\theta \tag{14}$$

$$\dot{\theta} = q \cos \phi - r \sin \phi \tag{15}$$

$$\dot{\phi} = p + \dot{\psi} \sin \theta \tag{16}$$

The model simulated is a round, non-rotating earth so that

$$H = \left((R_o + x)^2 + Z^2 + Y^2\right)^{1/2} - R_o \tag{17}$$

$$\dot{X} = \ell_1 \cdot u + m_1 \cdot v + n_1 \cdot w \tag{18}$$

$$\dot{Y} = \ell_2 \cdot u + m_2 \cdot v + n_2 \cdot w \tag{19}$$

$$\dot{Z} = \ell_3 \cdot u + m_3 \cdot v + n_3 \cdot w \tag{20}$$

$$\text{Cross Range} = R_o \bar{\psi} \tag{21}$$

$$\text{Down Range} = R_o \phi \tag{22}$$

$$\bar{\phi} = \tan^{-1}\left(Z/(R_o + x)\right) \tag{23}$$

$$\bar{\psi} = \tan^{-1}\left(Y/((R_o + x)^2 + Z^2)^{1/2}\right) \quad R_o = (3440)\ (6080)\ \text{FT.} \tag{24}$$

Winds are measured in the local earth surface coordinate system and are functions of altitude. Dynamic pressure, angle of attack, and angle of side slip are computed by

$$\alpha = \tan^{-1}\left((w + w_{wind})/(u + u_{wind})\right) \tag{25}$$

$$\beta = \sin^{-1}\left((v + v_{wind})/V_T\right) \tag{26}$$

$$V_T = \left((u + u_{wind})^2 + (v + v_{wind})^2 + (w + w_{wind})^2\right)^{1/2} \tag{27}$$

$$Q = 1/2\ \rho\ V_T^2 \tag{28}$$

$$u_{wind} = (\ell_2 \cdot \sin \Gamma + \ell_3 \cos \Gamma)\ \text{wind (H)} \tag{29}$$

$$v_{wind} = (m_2 \sin \Gamma + m_3 \cos \Gamma)\ \text{wind (H)} \tag{30}$$

$$w_{wind} = (n_2 \sin \Gamma + n_3 \cos \Gamma) \text{ wind } (H) \tag{31}$$

$$\Gamma = \Gamma_{\text{Wind Dir}} - \Gamma_{\text{Launch Dir}} \tag{32}$$

For the control system, a simple first-order lag is used. Then,

$$\dot{\delta}_P = K_{AP}\left(\delta_{P_{COM}} - \delta_P\right) \tag{33}$$

$$\dot{\delta}_Y = K_{AY}\left(\delta_{R_{COM}} - \delta_R\right) \tag{35}$$

$$\delta_{P_{COM}} = -K_\theta \cdot \left((\theta - \theta_c) + K_{\dot{\theta}} \cdot q + K_{I_P} \int (\theta - \theta_c)\, dt\right) \tag{36}$$

$$\delta_{Y_{COM}} = K_\psi \cdot \left(K_{I_Y} \int \psi \, dt + K_{\dot{\psi}} \cdot r + K'_{\psi}(t) \cdot \psi\right) + K_\beta (t)\, \beta \tag{37}$$

$$\delta_{R_{COM}} = K_\phi \cdot (K_{I_\phi} \int \phi \, dt + K_{\dot{\phi}} \cdot p + \phi) \tag{38}$$

Thrust is computed by

$$\text{Thrust} = I_{SP}(H) \cdot \dot{\overline{WF}} \tag{39}$$

Inertia and vehicle weight are functions of time and are inputs to the simulation. Aerodynamic data as a function of Mach number is linear tables input.

APPENDIX II

SMALL PERTURBATION EQUATIONS

This appendix describes the equations used in the small perturbation analysis into program TRIM-STAB, including those written for control point fatigue spectra generations.

From Newton's second law of motion,

$$\bar{F} = \frac{d}{dt}\,\bar{P} \quad \text{and} \quad \bar{M} = \frac{d}{dt}\,\bar{L} \tag{1}$$

where

$$\bar{P} = m\bar{V}_T$$

$$\bar{L} = I\bar{\omega}$$

$\bar{P}$ and $\bar{L}$ are the linear and angular momentums respectively.

For velocities with respect to a rotating axis system, these equations can be written as

$$\bar{F} = m\left(\frac{d}{dt}\,\bar{V} + \bar{\omega} \times \bar{V}_T\right) + \dot{m}\,\Delta\bar{V}_T$$

$$\bar{M} = \frac{d}{dt}\,\bar{L} + \bar{\omega} \times \bar{L} \tag{2}$$

The $\dot{m}\,\Delta\bar{V}$ term in the force equation is the thrust.

The angular and rotational velocities are divided into steady state and small perturbation quantities;

$$\bar{V}_T = (U_o + u)\,\bar{i} + (V_o + v)\,\bar{j} + (W_o + w)\,\bar{k} \tag{3}$$

$$\bar{\omega} = (P_o + p)\,\bar{i} + (Q_o + q)\,\bar{j} + (R_o + r)\,\bar{k} \tag{4}$$

Numerous assumptions are made. The first of these is that the vehicle has no lateral velocity nor roll or yaw rates, then

$$V_o = P_o = R_o = 0$$

$$\bar{V}_T = (U_o + u)\,\bar{i} + (v)\,\bar{j} + (W_o + w)\,\bar{k} \tag{5}$$

$$\bar{\omega} = p\,\bar{i} + (Q_o + q)\,\bar{j} + r\,\bar{k}$$

The $\bar{\omega} \times \bar{V}$ term in the force equation is therefore

$$\bar{\omega} \times \bar{V}_T = \begin{vmatrix} \bar{i} & \bar{j} & \bar{k} \\ (p) & (Q_o + q) & (r) \\ (U_o + u) & (v) & (W_o + w) \end{vmatrix}$$

$$= \bar{i}\left[Q_o W_o + Q_o w + q W_o + qw - rv\right] \tag{6}$$

$$- \bar{j}\left[pW_o + pw - rU_o - ru\right]$$

$$+ \bar{k}\left[pv - Q_o U_o - uQ_o - qU_o - qu\right]$$

The second assumption is that the products of small perturbations are negligible. Eliminating products of small perturbations and steady state terms yields

$$\Delta(\bar{\omega} \times \bar{V}_T) \simeq \bar{i}\,(wQ_o + qW_o)$$

$$+ \bar{j}\,(-pW_o + rU_o) \tag{7}$$

$$+ \bar{k}\,(-uQ_o - qU_o)$$

The perturbed force equation, from equations 2 and 7, are then

$$\Delta F_x = m\left\{\dot{u} + qW_o + wQ_o\right\}$$

$$\Delta F_y = m\left\{\dot{v} - pW_o + rU_o\right\} \tag{8}$$

$$\Delta F_z = m\left\{\dot{w} - uQ_o - qU_o\right\}$$

The angular momentum can be expressed as

$$\bar{L} = I\bar{\omega}$$

Where I is the second order inertial tensor

$$I = \begin{vmatrix} I_{xx} & -I_{xy} & -I_{xz} \\ -I_{yx} & I_{yy} & -I_{yz} \\ -I_{zx} & -I_{zy} & I_{zz} \end{vmatrix}$$

The third assumption is that the xz plane is a plane of symmetry, then

$$I_{yz} = I_{zy} = I_{xy} = I_{yx} = 0$$

$$I = \begin{vmatrix} I_{xx} & 0 & -I_{xz} \\ 0 & I_{yy} & 0 \\ -I_{zx} & 0 & I_{zz} \end{vmatrix} \tag{9}$$

with this assumption

$$\bar{L} = I\bar{\omega} = \begin{vmatrix} I_{xx} & 0 & -I_{xz} \\ 0 & I_{yy} & 0 \\ -I_{xz} & 0 & I_{zz} \end{vmatrix} \begin{vmatrix} p \\ Q_o + q \\ r \end{vmatrix} \tag{10}$$

$$L_x = pI_{xx} - rI_{xz}$$

$$L_y = Q_o I_{yy} + qI_{yy}$$

$$L_z = -pI_{xz} + rI_{zz}$$

The $\bar{\omega} \times \bar{L}$ term in the moment equation is

$$\bar{\omega} \times \bar{L} = \begin{vmatrix} \bar{i} & \bar{j} & \bar{k} \\ p & Q_o + q & r \\ (pI_{xx} - rI_{xz}) & (Q_o I_{yy} + qI_{yy}) & (rI_{zz} - pI_{xz}) \end{vmatrix} \tag{11}$$

$$= \bar{i}\,(r Q_o I_{zz} - p Q_o I_{xz} + qr I_{zz} - qp I_{xz} - r Q_o I_{yy} - rq I_{yy})$$

$$- \bar{j}\,(pr I_{zz} - p^2 I_{xz} - rp I_{xx} + r^2 I_{xz}) \qquad (11)$$

$$+ \bar{k}\,(p Q_o I_{yy} + pq I_{yy} - p Q_o I_{xx} + qr I_{xz} + r Q_o I_{xz} + pq I_{xx}) \qquad \text{(Contd)}$$

or, eliminating products of perturbations,

$$\bar{\omega} \times \bar{L} = \bar{i}\left[r Q_o (I_{zz} - I_{yy}) - p Q_o I_{xz}\right]$$

$$+\bar{k}\left[p Q_o (I_{yy} - I_{xx}) + r Q_o I_{xz}\right] \qquad (12)$$

The fourth assumption is that the time rate of change of the inertias is negligible.

$$\frac{d\bar{L}}{dt} = \frac{d}{dt}(I\bar{\omega}) = \frac{I d\bar{\omega}}{dt}$$

Using the fourth assumption the $\frac{d}{dt}\bar{L}$ term in the moment equation above, is

$$\frac{d}{dt}\bar{L} = \frac{d}{dt} I\bar{\omega} = I\frac{d}{dt}\bar{\omega} = \begin{vmatrix} I_{xx} & 0 & -I_{xz} \\ 0 & I_{yy} & 0 \\ -I_{xz} & 0 & I_{zz} \end{vmatrix} \begin{vmatrix} \dot{p} \\ \dot{q} \\ \dot{r} \end{vmatrix} \qquad (13)$$

$$= \bar{i}\,(\dot{p} I_{xx} - \dot{r} I_{xz})$$

$$+ \bar{j}\,(\dot{q} I_{yy})$$

$$+ \bar{k}\,(-\dot{p} I_{xz} + \dot{r} I_{zz})$$

The moment equation, (2) using equations 12 and 13 is

$$M_x = \dot{p} I_{xx} - \dot{r} I_{xz} + r Q_o (I_{zz} - I_{yy}) - p I_{xz} Q_o$$

$$M_y = \dot{q} I_{yy} \qquad (14)$$

$$M_z = \dot{r} I_{zz} - \dot{p} I_{xz} + p Q_o (I_{yy} - I_{xx}) + r Q_o I_{xz}$$

The gravity force term must be treated by rotating through Euler angles. In this work, the order of rotation is psi (ψ), theta (θ), and phi (ϕ).

Assume a normal, orthogonal, axis system with the X axis pointing forward, the Y axis out the right wing, and the Z axis down. Assume vector elements of $(X_o, Y_o, Z_o) = \bar{V}_T$ along the original axis. The transfer matrix describing this vector in a new frame caused by rotating about the Z axis is

$$\bar{V}_1 = A\bar{V}_T \text{ where } A = \begin{vmatrix} \cos\psi & \sin\psi & 0 \\ -\sin\psi & \cos\psi & 0 \\ 0 & 0 & 1 \end{vmatrix} \tag{15}$$

or, using small angle approximations,

$$A \simeq \begin{vmatrix} 1 & \psi & 0 \\ -\psi & 1 & 0 \\ 0 & 0 & 1 \end{vmatrix}$$

A second rotation about the new Y axis will have a transfer matrix of

$$\bar{V}_2 = B\bar{V}_1 \text{ where } B = \begin{vmatrix} \cos\theta & 0 & -\sin\theta \\ 0 & 1 & 0 \\ \sin\theta & 0 & \cos\theta \end{vmatrix} \tag{16}$$

or approximately

$$B \simeq \begin{vmatrix} 1 & 0 & -\theta \\ 0 & 1 & 0 \\ \theta & 0 & 1 \end{vmatrix}$$

The transfer matrix from V_T to V_2 (assuming the products of perturbations are zero) is

$$\bar{V}_2 = BA\bar{V}_T \text{ where } BA \simeq \begin{vmatrix} 1 & \psi & -\theta \\ -\psi & 1 & 0 \\ \theta & 0 & 1 \end{vmatrix}$$

The third rotation about the new X axis will have a transfer matrix of

$$\bar{V}_3 = C\bar{V}_2 \quad \text{where } C = \begin{vmatrix} 1 & 0 & 0 \\ 0 & \cos\phi & \sin\phi \\ 0 & -\sin\phi & \cos\phi \end{vmatrix} \tag{17}$$

or approximately

$$C \simeq \begin{vmatrix} 1 & 0 & 0 \\ 0 & 1 & \phi \\ 0 & -\phi & 1 \end{vmatrix}$$

The total small perturbation transfer matrix from $\bar{V}_T$ to $\bar{V}_3$ is

$$\bar{V}_3 = CBA\ \bar{V}_o$$

$$CBA = \begin{vmatrix} 1 & \psi & -\theta \\ -\psi & 1 & \phi \\ \theta & -\phi & 1 \end{vmatrix} \tag{18}$$

The fifth assumption is that the wings are level. Then the gravity vector in the unperturbed axis system is

$$\phi_o = 0$$

$$\bar{g} = g \begin{vmatrix} -\sin\theta_o \\ 0 \\ \cos\theta_o \end{vmatrix} \tag{19}$$

The perturbed gravity term, $(\bar{g}_p)$, as a function of the Euler angles ψ, θ, and ϕ is

$$\bar{g}_p = \begin{vmatrix} 1 & \psi & -\theta \\ -\psi & 1 & \phi \\ \theta & -\phi & 1 \end{vmatrix} \begin{vmatrix} -\sin\theta_o \\ 0 \\ \cos\theta_o \end{vmatrix} g \tag{20}$$

$$= \begin{vmatrix} -\sin\theta + \theta\cos\theta_o \\ \psi\sin\theta_o + \phi\cos\theta_o \\ -\theta\sin\theta_o + \cos\theta_o \end{vmatrix} g$$

The ΔF expressions in equation (8) can now be separated into aerodynamic and gravitational forces

$$\Delta F_x = \Delta F_{x_A} + \Delta F_{x_g} = m\,(\dot{u} + q\,W_o + w Q_o)$$

$$\Delta F_y = \Delta F_{y_A} + \Delta F_{y_g} = m\,(\dot{v} - p\,W_o + r\,U_o) \qquad (21)$$

$$\Delta F_z = \Delta F_{z_A} + \Delta F_{z_g} = m\,(\dot{w} - u\,Q_o - q\,U_o)$$

or, the aerodynamic forces are equal to

$$\Delta F_{x_A} = m\,(\dot{u} + q\,w_o + w\,Q_o) + mg\,\theta\cos\theta_o$$

$$\Delta F_{y_A} = m\,(\dot{v} - p\,w_o + r\,U_o) - mg\,(\psi\sin\theta_o + \phi\cos\theta_o) \qquad (22)$$

$$\Delta F_{z_A} = m\,(\dot{w} - u\,Q_o - q\,U_o) + mg\,\theta\sin\theta_o$$

The F_X and F_Z force equations are written as the respective body acclerations, (e.g., $\dot{u}$ and $\dot{w}$) with all terms having dimensions of ft/sec^2. The dimensionalizing procedure from an aerodynamic coefficient is

$$\left[X_u\ \left(\frac{1}{\text{sec}}\right)\right]\ u\ \left(\frac{\text{ft}}{\text{sec}}\right) = \left[\frac{qs}{m}\ \left(\frac{\text{ft}}{\text{sec}^2}\right)\ C_{x_u}\ \left(\frac{\text{sec}}{\text{ft}}\right)\right]\ u\ \left(\frac{\text{ft}}{\text{sec}}\right)$$

The lateral force equation, F_y, is expressed as $\dot{\beta}$ through the relationship

$$\beta = \tan^{-1}\frac{v}{V_T} \simeq \frac{v}{V_T}$$

$$\dot{\beta} = \frac{\dot{v}}{U_o} = \frac{\Delta F_y}{m U_o} \qquad V_o \approx V_T$$

All terms have dimensions of 1/sec. An aerodynamic coefficient* is dimensioned by

$$Y_\beta\ \left(\frac{1}{\text{sec}}\right)\ \beta = \left(\frac{qs}{mV_T}\right)\left(\frac{1}{\text{sec}}\right)\ C_{y_\beta}\ \beta$$

* The dimensionalization of lateral aerodynamic accelerations are divided by U_o.

All three moment equations are written in terms of the angular accelerations and have dimensions of $1/sec^2$. The dimensionalizing qualities are

$$\frac{qs\bar{c}}{I} \text{ for pitch}$$

and

$$\frac{qsb}{I} \text{ for roll and yaw}$$

where I is the corresponding inertia.

The equations are expressed as Euler Angles. This is valid for small perturbations when products of perturbations are neglected and small angle approximations of trigonometry functions are used.

The longitudinal equations, are

Longitudinal acceleration $(\dot{u})$

$$(S - X_u)\, u + (Q_o - X_w)\, w + (S\, W_o + g \cos \theta_o)\, \theta = X_{\delta_e}$$

Vertical acceleration $(\dot{w})$

$$(-Q_o - Z_u)\, u + \left[S\,(1 - Z_{\dot{w}}) - Z_w\right] w + \left[S(-u_o - Z_q) + g \sin \theta_o\right] \theta = Z_{\delta_e}$$

Pitch angular acceleration $(\ddot{\theta})$

$$(-M_u)\, u + (-SM_{\dot{w}} - M_w)\, w + (S^2 - SM_q)\, \theta = M_{\delta_e}$$

where X_{δ_e}, Z_{δ_e} and M_{δ_e} are the control forces and moment

The lateral equations are

Lateral acceleration $(\dot{\beta})$ (23)

$$\left[S\left(1 - Y_{\dot{\beta}}\right) - Y_\beta\right] \beta + \left[S\left(-\frac{w_o}{U_o} - Y_p\right) - \frac{g}{U_o} \cos \theta_o\right] \phi +$$

$$+ \left[S\,(1 - Y_r) - \frac{g}{U_o} \sin \theta_o\right] \psi = Y_{\delta_a} + Y_{\delta_r}$$

Roll acceleration ($\ddot{\phi}$)

$$\left[-SL_{\dot{\beta}} - L_{\beta}\right]\beta + \left[S^2 - S\left(Q_o I_{xz}/I_{xx} + L_p\right)\right]\phi$$

$$+ \left[-S^2 I_{xz}/I_{xx} + S\left(Q_o\left(\frac{I_{zz} - I_{yy}}{I_{xx}}\right) - L_r\right)\right]\psi = L_{\delta_a} + L_{\delta_r}$$

Yaw acceleration (ψ)

$$\left[-SN_{\dot{\beta}} - N_{\beta}\right]\beta + \left[-S^2\frac{I_{xz}}{I_{zz}} + S\left(Q_o\left(\frac{I_{yy} - I_{xx}}{I_{zz}}\right) - N_p\right)\right]\phi +$$

$$+ \left[S^2 + S\left(Q_o\frac{I_{xz}}{I_{zz}} - N_r\right)\right]\psi = N_{\delta_r} + N_{\delta_a}$$

where Y_{δ_a}, L_{δ_a}, and N_{δ_a} are the roll axis control force and moments and Y_{δ_r}, L_{δ_r} and N_{δ_r} are the yaw axis control force and moments

CENTER OF GRAVITY EQUATIONS

The small perturbation center of gravity acceleration, the inertial plus gravitational acceleration, can be taken directly from equation 22.

$$\Delta A_y = \dot{v} - p W_o + r U_o - \psi g \sin\theta_o - \phi g \cos\theta_o$$

$$\Delta A_z = \dot{w} - u Q_o - q U_o + \theta g \sin\theta_o \qquad (24)$$

ACTUATOR LAG AND TAIL-WAGS-DOG EQUATION

The tail-wags-dog zeros are a complex pair occurring at the frequency at which the inertial forces resulting from the gimballing of the rocket engine cancel the component of thrust normal to the missile axis due to deflection of the motor chamber.

The frequency can be computed from the following sketch

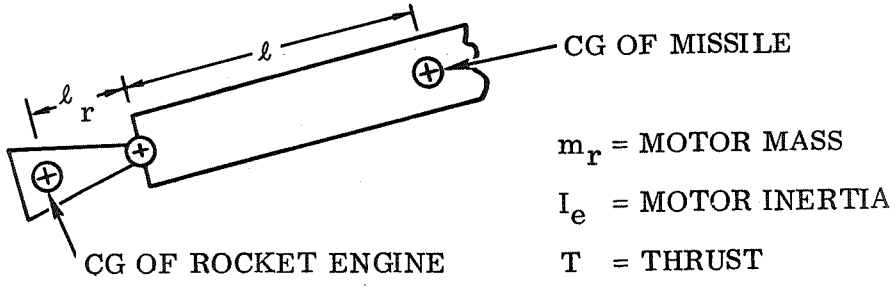

m_r = MOTOR MASS

I_e = MOTOR INERTIA

T = THRUST

Moments about the cg due to motor deflection are

$$M = I_e \ddot{\delta} + T \ell \delta + m_r \ell_r \ell \ddot{\delta}$$

or

$$M = \delta \left\{ S^2 \left(\frac{I_{e/\ell} + m_r \ell_r}{T} \right) + 1 \right\} T \ell \tag{25}$$

and

$$\omega_{n_{TWD}} = \left(\frac{T}{I_{e/\ell} + m_r \ell_r} \right)^{1/2}$$

Assuming a first order lag for actuator dynamics

$$\frac{\delta}{\delta_c} = \frac{1}{\tau_e S+1}$$

Then the dynamics between the actuator command and the resulting thrust is

$$\frac{M/T}{\delta_c} = \left(\frac{1/\omega^2_{n_{TWD}} S^2 + 1}{\tau_e S + 1} \right)$$

AUTOPILOT

The autopilot block diagram is

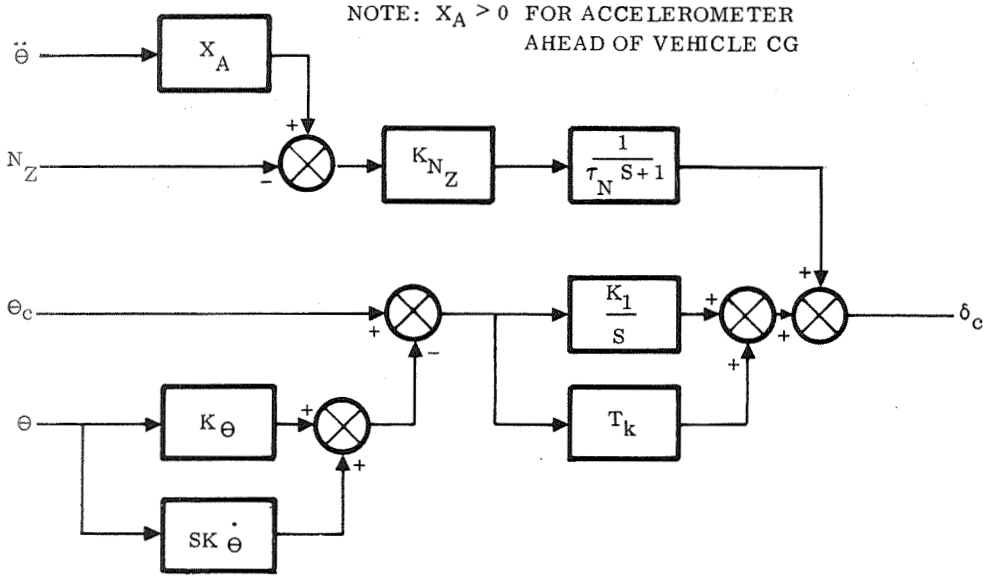

This can be reduced by block diagram algebra into an equation relating the gimbal command, (δ_c) as a function of pitch (θ), pitch command (θ_c), and normal acceleration (N_Z). This equation is

$$S(\tau_N S + 1)\,\delta_c = -\left\{\left[\tau_N T_k K_\theta - K_{N_Z} X_A\right] S^3 + \left[K_{\dot\theta}(T_k + \tau_N K_1) + \tau_N T_k K_\theta\right] S^2 + \left[K_1 K_{\dot\theta} + K_\theta (T_k + \tau_N K_1)\right] S + K_\theta K_1\right\}\theta + \left\{T_k \tau_N S^2 + (T_k + \tau_N K_1) S + K_1\right\}\theta_c - \left\{SK_{N_Z}\right\} N_Z \quad (26)$$

BENDING MODE EQUATIONS

The normalized bending mode equations are as follows:

$$\ddot\eta_i + B_{ii}\dot\eta_i + (\omega_{m_i} + K_{ii})\eta_i = \sum_{\substack{j=1 \\ j\neq i}}^{5} B_{ij}\dot\eta_j + \sum_{\substack{j=1 \\ j\neq i}}^{5} K_{ij}\eta_j \quad (27)$$

where i = 1, 5

K_{ij} and B_{ij} are the aerodynamic coupling terms between the modes as a function of the modal deflection and rate of deflection respectively. They are normalized from coefficients by the following expressions:

$$K_{ij} = \frac{qs}{gm} k_{ij} \qquad B_{ij} = \frac{qs}{gm} b_{ij}$$

where q = dynamic pressure
s = reference area
gm = generalized mass

k_{ij} and b_{ij} are functions of Mach number and altitude.

The preceeding leads to the matrix euqation presented in equation 28 and 29. The problem is divided into independent longitudinal and lateral sets.

The characteristic equation is determined by finding the eigenvalues (poles) of the determinate on the left hand side. The numerators of the transfer function are derived by the application of Cramer's Rule, in which the column on the right hand side replaces the column of interest in the determinate on the left hand side.

	U	W	θ	$N_{z_{C.G.}}$	ζ_1	$\zeta_2 \cdots \zeta_6$	δ_e	δ_s	δ_T	W_g
Axial Force	$(-X_u+s)$	(Q_o-X_w)	$g\cos\theta_o+W_o s$	0	0	0 ⋯ 0	X_{δ_e}	X_{δ_s}	0	X_g
Normal Force	$(-Q_o-Z_u)$	$-Z_w+(1-Z_{\dot{w}})s$	$+g\sin\theta_o-(U_o+Z_q)s$	0	A_{w1}	$A_{w2} \cdots A_{w6}$	Z_{δ_e}	Z_{δ_s}	Z_{δ_T}	W_g
Pitch Moment	$-M_u$	$(-M_w-M_{\dot{w}}s)$	$-M_q s+s^2$	0	$A_{\theta 1}$	$A_{\theta 2} \cdots A_{\theta 6}$	M_{δ_e}	M_{δ_s}	M_{δ_T}	θ_g
Normal Acceleration at C.G.	Q_o	$-s$	$-g\sin\theta_o+U_o s$	1	$N_1 s^2$	$N_2 s^2 \cdots N_6 s^2$	0	0	0	0
1st Symmetrical Modal Equation	0	A_{1w}	$A_{1\dot{\theta}}s$	0	$(A_{11}+\omega_1^2)+D_1 s+s^2$	$A_{12} \cdots A_{16}$	$A_{1\delta_e}$	$A_{1\delta_s}$	$A_{1\delta_T}$	A_{1g}
2nd Symmetrical Modal Equation	0	A_{2w}	$A_{2\dot{\theta}}s$	0	A_{21}	$(A_{22}+\omega_2^2)+D_2 s+s^2 \cdots A_{26}$	$A_{2\delta_e}$	$A_{2\delta_s}$	$A_{2\delta_T}$	A_{2g}
⋮	⋮	⋮	⋮	⋮	⋮	⋮	⋮	⋮	⋮	⋮
6th Symmetrical Modal Equation	0	A_{6w}	$A_{6\dot{\theta}}s$	0	A_{61}	$A_{62} \cdots (A_{66}+\omega_6^2)+D_6 s+s^2$	$A_{6\delta_e}$	$A_{6\delta_s}$	$A_{6\delta_T}$	A_{6g}
Elevator Control	0	$K_{E1}+K_{E2}s+K_{E3}s^2$	$K_{E4}+K_{E5}s+K_{E6}s^2+K_{E7}s^3$	0	To Be Determined		$\sum_{n=0}^{4} B_n^1 s^n$	$\sum_{n=0}^{4} B_n^2 s^n$	$\sum_{n=0}^{4} B_n^3 s^n$	0
Spoiler Control	0	$K_{s1}+K_{s2}+K_{s3}s^2$	$K_{s4}+K_{s5}s+K_{s6}s^2+K_{s7}s^3$	0			$\sum_{n=0}^{4} C_n^1 s^n$	$\sum_{n=0}^{4} C_n^2 s^n$	$\sum_{n=0}^{4} C_n^3 s^n$	0
Thrust Vector Control	0	$K_{T1}+K_{T2}s+K_{T3}s^2$	$K_{T4}+K_{T5}s+K_{T6}s^2+K_{T7}s^3$	0			$\sum_{n=0}^{4} D_n^1 s^n$	$\sum_{n=0}^{4} D_n^2 s^n$	$\sum_{n=0}^{4} D_n^3 s^n$	0

Q_o	Steady Pitch Velocity	Z	Normal Acceleration Due to External Force
U	Forward Velocity	X	Axial Acceleration Due to External Force
W	Normal Velocity	M	Pitch Acceleration Due to External Force
θ	Pitch Attitude	g	Gravity Acceleration Due to External Force
s	Laplace Operator	A	Acceleration Due to Modal Deflection
$N_{z_{C.G.}}$	Normal Acceleration at C.G.	D	Modal Damping Acceleration
C.G.	Center of Gravity	K	Constant
$\zeta_{1,2,\ldots,6}$	Modal Generalized Coordinate	B	Constant
δ_e	Elevator Deflection	C	Constant
δ_s	Spoiler Deflection	D	Constant
δ_T	Thrust Vector Deflection	N	Modal Deflection at C.G.
W_g	Gust Velocity	ω	Modal Frequency

Subscripts:

u	Per Unit U Velocity
w	Per Unit W Velocity
q	Per Unit Pitch Velocity
w1,w2,⋯,w6	Normal Acceleration Per Unit Modal Deflection 1,2,⋯,6
θ1,θ2, ..., θ6	Pitch Acceleration Per Unit Modal Deflection 1,2,⋯,6
δ_e	Per Unit δ_e
δ_s	Per Unit δ_s
δ_T	Per Unit δ_T
1,2,⋯,6	Mode 1,2,⋯,6
E1, E2,⋯	Elevator Constants
s1, s2,⋯	Spoiler Constants
T1, T2,⋯	Thrust Vector Constants
(x,y)	Influence on X Mode by Y Mode X = 1,2,⋯,6; Y = 1,2,⋯,6
g	Gust Acceleration
o	Steady State Value

Equation 28. Longtidunal Equations

	β	ϕ	ψ	N_y	ξ_1	$\xi_2 \cdots\cdots \xi_6$	δ_r	δ_a	δ_s	δ_T		Gust
Lateral Force	$-Y_\beta + U_o s$	$-g\cos\theta_o - (W_o + Y_p)s$	$-g\sin\theta_o + (U_o - Y_R)s$	0	A_{Y1}	$A_{Y2} \cdots\cdots A_{Y6}$	Y_{δ_r}	Y_{δ_a}	Y_{δ_s}	Y_{δ_T}		Y_g
Roll Moment	$-L_\beta$	$+(-L_p s + s^2)$	$-(L_v s + I_{xz}/I_{xx} s^2)$	0	A_{L1}	$A_{L2} \cdots\cdots A_{L6}$	L_{δ_r}	L_{δ_a}	L_{δ_s}	L_{δ_T}		L_g
Yaw Moment	$-N_\beta$	$-(N_p s + I_{xz}/I_{zz})s^2$	$-N_r s + s^2$	0	A_{N1}	$A_{N2} \cdots\cdots A_{N6}$	N_{δ_r}	N_{δ_a}	N_{δ_s}	N_{δ_T}		N_g
Lateral Acceleration	$-U_o s$	$g\cos\theta_o + W_o s$	$g\sin\theta_o - U_o$	1	$NM_1 s^2$	$NM_2 s^2 \cdots\cdots NM_6 s^2$	0	0	0	0		0
1st Asymmetrical Modal Equation	$A_{1\beta}$	A_{1p}	A_{1r}	0	$(A_{11} + \omega_1^2) + D_1 s + s^2$	$A_{12} \cdots\cdots A_{16}$	$A_{1\delta_r}$	$A_{1\delta_a}$	$A_{1\delta_s}$	$A_{1\delta_T}$		A_{1g}
2nd Asymmetrical Modal Equation	$A_{2\beta}$	A_{2p}	A_{2r}	0	A_{21}	$(A_{22} + \omega_2^2) + D_2 s + s^2 \cdots A_{26}$	$A_{2\delta_r}$	$A_{2\delta_a}$	$A_{2\delta_s}$	$A_{2\delta_T}$		A_{2g}
⋮	⋮	⋮	⋮	⋮	⋮	⋮ ⋮	⋮	⋮	⋮	⋮		⋮
6th Asymmetrical Modal Equation	$A_{6\beta}$	A_{6p}	A_{6r}	0	A_{61}	$A_{62} \cdots\cdots (A_{66} + \omega_6^2) + D_6 s + s^2$	$A_{6\delta_r}$	$A_{6\delta_a}$	$A_{6\delta_s}$	$A_{6\delta_T}$		A_{6g}
Rudder Control	$C_1^1 + C_2^1 s + C_3^1 s^2$	$\sum_{n=0}^{4} C_n^5 s^n$	$\sum_{n=0}^{4} C_n^6 s^n$	$\sum_{n=0}^{4} C_n^7 s^n$	To Be Determined		$\sum_{n=0}^{4} O_n^1 s^n$	$\sum_{n=0}^{4} O_n^2 s^n$	$\sum_{n=0}^{4} O_n^3 s^n$	$\sum_{n=0}^{4} O_n^4 s^n$	=	0
Aileron Control	$C_1^2 + C_2^2 s + C_3^2 s^2$	$\sum_{n=0}^{4} C_n^8 s^n$	$\sum_{n=0}^{4} D_n^9 s^n$	$\sum_{n=0}^{4} C_n^{10} s^n$			$\sum_{n=0}^{4} O_n^5 s^n$	$\sum_{n=0}^{4} O_n^6 s^n$	$\sum_{n=0}^{4} O_n^7 s^n$	$\sum_{n=0}^{4} O_n^8 s^n$		0
Spoiler Control	$C_1^3 + C_2^3 s + C_3^3 s^2$	$\sum_{n=0}^{4} C_n^{11} s^n$	$\sum_{n=0}^{4} C_n^{12} s^n$	$\sum_{n=0}^{4} C_n^{13} s^n$			$\sum_{n=0}^{4} O_n^9 s^n$	$\sum_{n=0}^{4} O_n^{10} s^n$	$\sum_{n=0}^{4} O_n^{11} s^n$	$\sum_{n=0}^{4} O_n^{12} s^n$		0
Thrust Vector Control	$C_1^4 + C_2^4 s + C_3^4 s^2$	$\sum_{n=0}^{4} C_n^{14} s^n$	$\sum_{n=0}^{4} C_n^{15} s^n$	$\sum_{n=0}^{4} C_n^{16} s^n$			$\sum_{n=0}^{4} O_n^{13} s^n$	$\sum_{n=0}^{4} O_n^{14} s^n$	$\sum_{n=0}^{4} O_n^{15} s^n$	$\sum_{n=0}^{4} O_n^{16} s^n$		0

β	Sideslip
ϕ	Bank Angle
ψ	Yaw Angle
N_y	Lateral Acceleration
$\xi_{1,2,\ldots,6}$	Asymmetric Mode Generalized Coordinate
δ_r	Rudder Deflection
δ_a	Aileron Deflection
δ_s	Spoiler Deflection
δ_T	Thrust Vector Deflection
g	Gravity
Y	Lateral Acceleration
D	Modal Damping
L	Roll Acceleration
N	Yaw Acceleration
U_o	Total Steady Velocity
I_{xz}	Cross Product of Inertia
I_{xx}	Roll Inertia
I_{zz}	Yaw Inertia
A	Modal Acceleration
NM	Modal Deflection at Accelerometer
s	Laplace Operator
C	Constants
O	Constants
ω	Modal Frequencies
W_o	Steady Normal Velocity

Subscripts:

β	Sideslip Unit Acceleration
p	Rolling Velocity Unit Acceleration
r	Yawing Velocity Unit Acceleration
$1, 2, \cdots, 6$	Modal Reference
g	Gust
δ_r	Rudder Unit Acceleration
δ_a	Aileron Unit Acceleration
δ_s	Spoiler Unit Acceleration
δ_T	Thrust Vector Unit Acceleration
(x, y)	Unit Acceleration in X Mode Produced by Y Mode X = 1, 2, ···, 6; Y = 1, 2, ···, 6, δ_r, δ_a, etc.
o	Steady State Velocity

Equation 29. Lateral Equations

APPENDIX III

MULTIPLE LOOP ANALYSIS

Throughout this study multiple, feedback loops were used. Within each loop only constant coefficient linear systems of equations were developed. The technique used in analyzing these systems was to write all the equations necessary to discribe the complete, overall system. In matrix notation this leads to

$$\underset{n \times n}{\begin{bmatrix} \sum_{i=0}^{m_{11}} K_{11i} S^i & \cdots & \\ \vdots & \ddots & \\ \sum_{i=0}^{m_{1n}} K_{1ni} S^i & & \sum_{i=0}^{m_{nn}} K_{nni} S^i \end{bmatrix}} \begin{bmatrix} x_1 \\ x_2 \\ \vdots \\ x_m \end{bmatrix} = \begin{bmatrix} 1 \\ 0 \\ 0 \\ \vdots \\ 0 \end{bmatrix} \tag{1}$$

The stability characteristics of equation 1 are evaluated by evaluating the determinant of the square matrix. Loop stability is evaluated by varying the gain or parameter of interest and reevaluating the determinant of the resultant matrix. On the surface, this may appear to be a costly process. However, a rapid computational method has been developed. In the method used, the left side of equation (1) is written as

$$\left[A_k\right] S^k + \left[A_{k-1}\right] S^{k-1} + \cdots + \left[A_o\right] \tag{2}$$

If $\left[A_k\right]$ is nonsingular, an inverse of A_k is found. Then,

$$S^k + \left[B_{k-1}\right] S^{k-1} + \cdots + \left[B_o\right] \tag{3}$$

where

$$\begin{aligned} \left[B_{k-1}\right] &= \left[A_k\right]^{-1} \left[A_{k-1}\right] \\ &\vdots \\ \left[B_o\right] &= \left[A_k\right]^{-1} \left[A_o\right] \end{aligned} \tag{4}$$

A new equivalent linear matrix equation is formulated as

$$\begin{bmatrix} -B_{k-1} & -B_{k-2} & \cdots & -B_o \\ I & 0 & \cdots & 0 \\ 0 & I & \cdots & 0 \\ \cdot & \cdot & \cdots & \cdot \\ \cdot & \cdot & \cdots & \cdot \\ 0 & 0 & \cdots & I\ 0 \end{bmatrix} \begin{bmatrix} S^{k-1} \\ S^{k-2} \\ S^{k-3} \\ \cdot \\ \cdot \\ 1 \end{bmatrix} = S \begin{bmatrix} S^{k-1} \\ S^{k-2} \\ S^{k-3} \\ \cdot \\ \cdot \\ 1 \end{bmatrix} \tag{5}$$

The stability of equation 1 can now be evaluated by determining the eigenvalues of equation 5. The computation of the eigenvalues of equation 5 is approximately an order of magnitude faster than the expansion of the miners of the matrix in equation (1).

To determine the polynominal which represents the matrix expansion and to evaluate the gain, the following procedure is used. From the eigenvalues form

$$\prod_{i=1}^{j} (S - \lambda_i) = \sum_{ii=0}^{j} \epsilon_{ii} S^{ii} \tag{6}$$

where λ_i 's are the eigenvalues.

Choose a number, A, such that

$$A \neq \lambda_i$$

Then numerically evaluate (6) with

$$S = A$$

then

$$\sum_{ii=o}^{j} \epsilon_{ii} A^{ii} = C_1 \tag{7}$$

The square matrix in equation (1) is also numerically evaluated with S = A. That numerical value is C_2. Then the gain is the ratio C_2/C_1.

If A_k is singular, then one of two procedures can be followed. The first procedure is to elevate the equation of (1) until A_k is nonsingular and proceed through the described method. Each equation elevation yields one nonvalid zero root. These nonvalid roots are discarded.

The other alternate procedure is if A_o in equation (2) is nonsingular, determine A_o^{-1}, then,

$$\left[C_k\right] S^k + \left[C_{k-1}\right] S^{k-1} + \cdots + 1 \tag{8}$$

where

$$\left[C_k\right] = \left[A_o\right]^{-1} \left[A_k\right]$$

$$\left[C_{k-1}\right] = \left[A_o\right]^{-1} \left[A_{k-1}\right]$$

A new equivalent linear matrix equation is

$$\begin{bmatrix} -[C_1] & -[C_2] & \cdots & -[C_k] \\ [I] & [0] & \cdots & 0 \\ 0 & [I] & \cdots & \\ \vdots & \vdots & \cdots & \\ 0 & 0 & \cdots & [I]\ [0] \end{bmatrix} \begin{bmatrix} 1 \\ S \\ \vdots \\ S^{k-1} \end{bmatrix} = \frac{1}{S} \begin{bmatrix} 1 \\ S \\ \vdots \\ S^{k-1} \end{bmatrix} \tag{9}$$

Then the eigenvalues of (9) are the inverse of the roots of (1). The steps outlined in equation (6) and (7) are also followed.

Unclassified

Security Classification

DOCUMENT CONTROL DATA - R & D

(Security classification of title, body of abstract and indexing annotation must be entered when the overall report is classified)

1. ORIGINATING ACTIVITY *(Corporate author)*

Convair Aerospace Division of General Dynamics
San Diego, California

2a. REPORT SECURITY CLASSIFICATION

Unclassified

2b. GROUP

3. REPORT TITLE

A Preliminary Investigation of Potential Value-Loads Alleviation Control for Space Shuttle Vehicles

4. DESCRIPTIVE NOTES *(Type of report and inclusive dates)*

Final

5. AUTHOR(S) *(First name, middle initial, last name)*

Bernard J. Kuchta

6. REPORT DATE	7a. TOTAL NO. OF PAGES	7b. NO. OF REFS
30 June 1971	109	11

8a. CONTRACT OR GRANT NO.	9a. ORIGINATOR'S REPORT NUMBER(S)
NAS9-11191	GDC-DDE71-001
b. PROJECT NO.	
c.	9b. OTHER REPORT NO(S) *(Any other numbers that may be assigned this report)*
d.	

10. DISTRIBUTION STATEMENT

Distribution of this document is unlimited

11. SUPPLEMENTARY NOTES	12. SPONSORING MILITARY ACTIVITY
	None

13. ABSTRACT

A study was conducted to investigate the potential value of load alleviation control for the space shuttle vehicle. The study considered rigid body load alleviation to reduce design loads. Trajectory biasing, gain scheduling, accelerometer feedback, and angle-of-attack command systems were investigated. A preliminary fatigue analysis of major structural components was performed. No significant fatigue damage was encountered. Modal stabilizations of structural modes was studied for body and wing modes. Multipule sensors and multipule controllers will be necessary for the space shuttle vehicle to increase structural mode damping.

DD FORM 1 NOV 65 1473

Unclassified

Security Classification

14. KEY WORDS	LINK A		LINK B		LINK C	
	ROLE	WT	ROLE	WT	ROLE	WT

GENERAL DYNAMICS

Convair Aerospace Division